STUDYING THE IMPACT OF XENON GAS IN URANIUM–MOLYBDENUM FUEL

A Dissertation

presented to

the Faculty of the Graduate School

at the University of Missouri

In Partial Fulfillment

of the Requirements for the Degree

Doctor of Philosophy

---

by

ABU RAFI MOHAMMAD IASIR

Dr. Karl D Hammond, Dissertation Supervisor

MAY, 12 2021

The undersigned, appointed by the dean of the Graduate School, have examined the dissertation entitled

STUDYING THE IMPACT OF XENON GAS IN
URANIUM–MOLYBDENUM FUEL

presented by Abu Rafi Mohammad Iasir,
a candidate for the degree of Doctor of Philosophy,
and hereby certify that, in their opinion, it is worthy of acceptance.

_____
Professor Karl D Hammond, chair

_____
Professor Scott Kovalaski, member

_____
Professor Robert Winholtz, member

_____
Professor Nickie Peters, member

To my parents Ismail and Halima

"Do you think that I know what I am doing?
That for one breath or half-breath I belong to myself?
As much as a pen knows what it's writing,
Or the ball can guess where it's going next."

—Rumi

ACKNOWLEDGMENTS

TABLE OF CONTENTS

Chapter

LIST OF TABLES

LIST OF FIGURES

LIST OF SYMBOLS

λ thermal conductitivity

λ_0 thermal conductivity of 100% dense material

λ_p thermal conductivity of dispersed phase

λ_s thermal conductivity of continuous phase (U–10Mo)

$\mathcal{H}$ many body hamiltonian

ν porosity

ν_p volume fraction of xenon in U–10Mo

K thermal conductivity tensor

K_{eff} effective thermal conductivity

q'' heat flux

T absolute temperature

CHAPTER 1

U–Mo FUEL: A BRIEF INTRODUCTION

Since the discovery of fission in 1938, the world has seen the impact of nuclear power on the modern world. The primary fuel for fission is ^{235}U. Naturally occurring uranium consists of a combination of different isotopes; about 99.3% ^{238}U, 0.7% ^{235}U and trace amounts of ^{234}U. Uranium can be 'enriched' in the ^{235}U isotope by using various complicated processes that mainly uses the defference in masses and/or other physical properties. Uranium that has a concentration of ^{235}U from natural level to 20% is called low enriched uranium (LEU). Typical power reactor fuel has ^{235}U assays below 5%.

After the Manhattan project, the enriched uranium (>90% ^{235}U) has been used for many peaceful usage in scientific research and radioisotope production. Nuclear fuels are characterized by a unique combination of physics, engineering, safety requirements, social and environmental factors, and international concerns. The purpose of nuclear safety is to prohivit the uncontrolled release of the radioactive isotopes to the environment and ensuring safe use of the fissile material. Highly enriched uranium (HEU) fuel is also a proliferation concern. All enrichments above 20% ^{235}U are considered HEU [1]

Proliferation concerns about HEU resulted a global effort, led by USA, to eradicate the civil uses of HEU in research and test reactors. One of the important programmes is known as RERTR. The Reduced Enrichment for Research and Test Reactors (RERTR) program was initiated in the USA in the late 1970s to develop new nuclear fission fuels to replace high-enriched uranium (HEU) [2, 3]. The RERTR program is now managed by the U.S. National Nuclear Security Administration (NNSA) office of Material Management

and Minimization (M^3). The development of low-enrichment uranium (LEU) fuels for high-performance reactors is an important nonproliferation initiative [4]. This initiative has completed a total of 69 reactors conversions to the use of LEU fuel, and 26 reactor facilities have been verified to have been shut down [5]. The conversion of six domestic high performance research reactors [1] that still use highly enriched uranium fuel is yet to be achieved. Due to their unique operating conditions, converting these six reactors is not easy and created a plethora of nuclear engineering challenges. These conversion process may take longer time periods, but developing a new LEU fuel is essential to ensure better performance and limiting nuclear proliferation. The current timeline to for the conversion is estimated to be 10–16 years [6, 7].

Research reactors operate at relatively low peak fuel temperatures, but are required to meet fuel performance requirements at high burnup. A typical peak fuel centerline temperature is around 250°C [8]. For a research reactor fission densities are usually in the range of 3×10^{21} to 6×10^{21} fissions/cm^3. In some cases, peak fuel fission density exceeds 7×10^{21} fissions/cm^3, requiring a higher number of initial ^{235}U atoms. One of the main requirements of LEU fuels is increased uranium density, such as that found in metallic uranium, to offset the decrease in ^{235}U enrichment. There are a fewer number of uranium alloys that have the combination of high uranium density and stable fuel behavior to the high burnup to replace the high power density reactors. Metallic uranium is thought to have sufficient density, but the orthorhombic crystal structure of α-U and the anisotropic fuel swelling that results make it unattractive as a fuel [9]. Uranium alloys that retain the high-temperature γ-phase, which is body-centered cubic, are more suitable for reactor fuel due to their more isotropic radiation-induced swelling behavior compared with α-uranium [10].

Various uranium alloys have been tested as alternative metallic fuels under reactor operating conditions, including U_6Fe and U_6Mn [11, 12]. Elements such as molybdenum (Mo),

---

[1] Advance Test Reactor at INT, Idaho; Advanced Test Reactor Assembly at INL, Idaho; High Flux Isotope Reactor at ORNL, Tennessee; Massachusetts Institute of Technology Reactor, Massachusetts; National Bureau of Standards Reactor in Gaithersburg, Maryland; University of Missouri Research Reactor in Columbia, Missouri.

niobium (Nb), titanium (Ti), and zirconium (Zr) have also been tried as alloying elements because of their solubility in γ-uranium [13–15]. Molybdenum stabilizes uranium's γ-phase at concentrations near the eutectoid point, lowering the phase transition temperature from 776 °C for pure uranium (corresponding to the β–γ allotropic point) to the eutectoid point of 555 °C for 11.1 percent molybdenum in γ-uranium [16, 17]. To take advantage of this, uranium alloyed with 10 wt% molybdenum (U-10Mo) is currently being developed as a potential high-density LEU fuel for high-performance research reactors.

Before the current interest in U–Mo metallic fuel, some of the earlier nuclear reactors used metallic fuel because of the combination of high uranium density and metallic properties. The Godiva IV pulsed reactors at Los Alamos (initially known as *Lady Godiva*) used U–Mo alloys, which date back to 1960. The Fast Burst Reactor (FBR) at White Sands, the Army Pulsed Radiation Facility (Aberdeen, MD), and the Sandia Pulsed Reactor II used U–Mo alloys. All of these reactors utilized the γ phase of uranium, but because of the short irradiation time, the impacts of fuel burnup were minimal [18]. The Dounreay Fast Reactor used a number of metal-fuel-based designs, which inclueds U–9.1Mo (9.1 wt% Mo) and U–7Mo clad in niobium. The highly alloyed fuel cracked more, even though the 9.1-wt%-Mo fuel swelled slightly less than 7 wt%-Mo alloy [19]. In U.S. the Enrico Fermi Fast Breeder Reactor (EFFBR) was the first commercial fast reactor that used U–10Mo fuel. The primary concern was to ensure that the fuel would remain in the γ-phase during the operating condition. A series of experiments have been performed to map the fission rate and temperature dependence of the γ-phase's stability [20]. Two types of U–Mo alloy fuel have been designed and tested. One is monolithic fuel, in which a thin layer of U–Mo foil is bonded to aluminum cladding. The other is a dispersion fuel in which of U–Mo fuel particles are dispersed in an Al matrix.

For five decades, dispersion fuels have powered many test and research reactors worldwide. The manufacturing process and operating conditions are well established for these types of fuels. The high-burnup testing of the dispersion fuel showed a pattern of breakaway

swelling [2] behavior at intermediate burnup. The post-irradiation examination of the U–Mo dispersion fuel revealed that this phenomenon is due to fission gas released from the interaction layer. Reaction between the U–Mo and aluminum occurs during irradiation and forms a ternary $[(U–Mo)Al_x]$ phase which releases the fission gas at the boundary between the interaction phase and the aluminum matrix [21–24]. These gas bubbles have a tendency to aggregate into the gas pockets, which weakens the fuel meat by exerting internal pressure. The result is mechanical failure and increase in fuel volume. To eliminate the fuel–matrix interaction, a 'monolithic' U–Mo fuel was suggested. In monolithic fuels, a zirconium foil is used as a diffusion barrier between the fuel and the cladding (aluminum) to prevent diffusion of molybdenum into the cladding [22].

This dissertation investigates how fission gas (xenon and krypton) impacts the transport properties of U–Mo fuel. In Chapter 2 we discuss the reduction of thermal conductivity due to the presence of fission gas. In Chapter 3 we introduce a new pseudopotential for metallic uranium to study the properties using density functional theory (DFT). A basic background of DFT is also discussed in this chapter. In Chapter 4 we look into the diffusion of xenon in γ-uranium and U–Mo alloy. In Chapter 5 we discuss the conclusions and future work.

References

1. *Management of High Enriched Uranium for Peaceful Purposes: Status and Trends.* Number 1452 in TECDOC Series. INTERNATIONAL ATOMIC ENERGY AGENCY, Vienna, 2005.

2. Armando Travelli. Current status of the RERTR program. Technical report, Argonne National Lab., IL (USA), 1980.

3. James L. Snelgrove, G. L. Hofman, M. K. Meyer, C. L. Trybus, and T. C. Wiencek. Development of very-high-density low-enriched-uranium fuels. *Nucl. Eng. Des.*, 178(1):119–126, 1997.

4. National Nuclear Security Administration. Material management minization. `https://www.energy.gov/nnsa/missions/nonproliferation`, 2021.

---

[2]The *breakaway* is defined as "the limiting exposure, beyond which there will be a marked increase in the rate of swelling as a function of burnup [25]"

5. EH Wilson, A Bergeron, JA Stillman, TA Heltemes, D Jaluvka, and L Jamison. Us high performance research reactor conversion program: an overview on element design. In *Proceedings of the 2017 European Research Reactor Conference*. RRFM Rotterdam, Netherlands, 2017.

6. National Academies of Sciences, Engineering, and Medicine. *Reducing the Use of Highly Enriched Uranium in Civilian Research Reactors*. National Academies Press, Washington, DC, 2016.

7. National Research Council. *Progress, Challenges, and Opportunities for Converting U.S. and Russian Research Reactors: A Workshop Report*. National Academies Press, Washington, DC, 2012.

8. M. K. Meyer, J. Gan, J. F. Jue, D. D. Keiser, E. Perez, A. Robinson, D. M. Wachs, N. Woolstenhulme, G. L. Hofman, and Y. S. Kim. Irradiation performance of U-Mo monolithic fuel. *Nucl. Eng. Technol.*, 46(2):169–182, 2014.

9. SF Pugh. Swelling in alpha uranium due to irradiation. *Journal of Nuclear Materials*, 4(2):177–199, 1961.

10. J. H. Kittel, B. R. T. Frost, J. P. Mustelier, K. Q. Bagley, G. C. Crittenden, and J. Van Dievoet. History of fast reactor fuel development. *J. Nucl. Mater.*, 204:1–13, 1993.

11. M. K. Meyer, T. C. Wiencek, S. L. Hayes, and G. L. Hofman. Irradiation behavior of U_6Mn–Al dispersion fuel elements. *J. Nucl. Mater.*, 278(2):358–363, 2000.

12. G. L. Hofman, R. F. Domagala, and G. L. Copeland. Irradiation behavior of low-enriched U_6Fe-Al dispersion fuel elements. *J. Nucl. Mater.*, 150(2):238–243, 1987.

13. G Donzé and G Cabane. Stabilisation de la phase γ dans les alliages ternaires a base d'uranium-molybdene. *J. Nucl. Mater.*, 1(4):364–373, 1959.

14. F Giraud-Heraud and J Guillaumin. Transition phase formation in U-7,5% Nb-2,5%Zr alloy. *Acta Metall.*, 21(9):1243–1252, 1973.

15. Denise Adorno Lopes, Thomaz Augusto Guisard Restivo, and Angelo Fernando Padilha. Mechanical and thermal behaviour of U–Mo and U–Nb–Zr alloys. *J. Nucl. Mater.*, 440(1):304–309, 2013.

16. Hiroaki Okamoto, Mark E. Schlesinger, and Erik M. Mueller, editors. *Mo (Molybdenum) Binary Alloy Phase Diagrams*, volume 3 of *ASM Handbook*, pages 489–498. ASM International, 2016.

17. A. Berche, N. Dupin, C. Guénau, C. Rado, B. Sundman, and J. C. Dumas. Calphad thermodynamic description of some binary systems involving U. *J. Nucl. Mater.*, 411:131–143, 2011.

18. J. A. Horak, J. A. Reuscher, and D. J. Sasmor. Operating experience with uranium–molybdenum fuel in pulsed reactors. Technical report, Sandia Labs., Albuquerque, N. Mex.(USA), 1973.

19. S. A. Cottrell, E. Edmonds, P. Higginson, and W. Oldfield. Development and performance of dounreay fast reactor metal fuel. Technical report, United Kingdom Atomic Energy Authority. Industrial Group. Dounreay, 1964.

20. International Atomic Energy Agency. Development status of metallic, dispersion and non-oxide advanced and alternative fuels for power and research reactors. *Nuclear Fuel Cycle and Material Section*, 2003.

21. Ann Leenaers, S. Van den Berghe, E. Koonen, C. Jarousse, F. Huet, M. Trotabas, M. Boyard, S. Guillot, L. Sannen, and M. Verwerft. Post-irradiation examination of uranium–7wt% molybdenum atomized dispersion fuel. *J. Nucl. Mater.*, 335(1):39–47, 2004.

22. Jan-Fong Jue, Dennis D. Keiser, Cynthia R. Breckenridge, Glenn A. Moore, and Mitchell K. Meyer. Microstructural characteristics of hip-bonded monolithic nuclear fuels with a diffusion barrier. *J. Nucl. Mater.*, 448(1):250–258, 2014.

23. Sven Van den Berghe, Wouter Van Renterghem, and Ann Leenaers. Transmission electron microscopy investigation of irradiated U–7wt% Mo dispersion fuel. *J. Nucl. Mater.*, 375(3):340–346, 2008.

24. D. Olander. Growth of the interaction layer around fuel particles in dispersion fuel. *J. Nucl. Mater.*, 383(3):201–208, 2009.

25. A E Guay. Uranium swelling in N-Reactor (PT-NR-4, Sup. A, Report No. 1). United States. `https://www.osti.gov/biblio/10163384`.

CHAPTER 2

EFFECT OF XENON ON THE OVERALL THERMAL CONDUCTIVITY OF U–10Mo

This chapter was largely published as an article in Journal of Nuclear Materials. The authors of that paper are A. Rafi M. Iasir and Karl D. Hammond of the University of Missouri and Nickie J. Peters of the University of Missouri Research Reactor.

2.1 Introduction

Thermal conductivity is an important property of any nuclear fuel, since most of the important physical properties are temperature-dependent. In the case of high-performance reactors, fuels must undergo high fission density at relatively low temperatures. For this reason, research reactor fuels are designed for efficient heat rejection. During test operations, Burkes and coworkers [1] observed that the thermal conductivity in monolithic fuels decrease significantly with increased burnup. For a fission density of 3.30×10^{21} cm^{-3} at 200 °C, thermal conductivity decreased by approximately 30%; at 4.53×10^{21} cm^{-3}, conductivity decreased by 45% [1].

Fission also creates a variety of fission products, which result in gas bubbles, metallic precipitates, and solutes in the fuel matrix [2]. These fission products, in addition to radiation damage in reactor environments, result in complex microstructural evolution that restructures the nuclear fuel over time. Fission gas bubbles are particularly problematic, as they cause changes in thermal conductivity and swelling of the fuel. In addition, ^{135}Xe is a potent neutron absorber.

For every four fission events, an average of one inert gas atom (xenon or krypton) is produced. The dominant gaseous species is xenon, accounting for almost 85% of fission gas [3, 4]. Xenon atoms in U–Mo alloy fuels have a strong tendency to precipitate into small bubbles due to their low solubility. The formation and growth of gas bubbles inside irradiated nuclear fuels has technical importance, as bubbles influence the microstructure of the material [5]. Recent TEM and SEM images show that fission bubbles in U-10Mo distribute themselves in both inter-granular and intra-granular formations [6–9]. High-fission-density fuels show randomly-distributed, micrometer-sized fission gas bubbles distributed throughout the grains [9]. Inter-granular bubble density increases with burnup.

Inside the micrometer-sized grains, fission gas forms superlattices [6, 7, 9], similar to those seen in ion-irradiated materials [10–19]. Typical bubble sizes are 2–6 nm in diameter, and the distance between the bubbles is typically in the 4–12 nm range. The superlattice usually has the same crystal structure as the host material, but an exception exists: the superlattice in U-10Mo shows a face-centered cubic structure in a body-centered cubic matrix. An ion-irradiated bubble superlattice has a lattice parameter of tens of nanometers [6]; that of fission gas bubbles is typically similar [20].

The thermal conductivity of a monolithic U–Mo fuel plate is at a maximum prior to irradiation [1]. Inclusions and porosity change the thermal and the electrical conductivity of many materials [21]. Solid fission products usually have minimal impact on overall thermal conductivity, as their conductivities are similar to the conductivity of the fuel. Gases, on the other hand, have much lower thermal conductivity than the matrix, and typically have much lower densities and heat capacities as well. Various models, both empirical and theoretical, have been proposed to describe the changes in conductivity due to gas bubbles. Maxwell [22] was among the first to derive an expression for the effective thermal conductivity of heterogenic media; his model assumed uniform distribution of spherical particles in a matrix. A few other empirical models also exist [23–25]; unfortunately, the large diversity of pore shape, pore size, and type of included material inside nuclear fuel make it

impossible to describe heat transfer with a single equation. Several theoretical models have been proposed to describe the influence of porosity and inclusions on the thermal conductivity [22, 26–29]. These theoretical models usually assume pores with regular geometric shapes, and that the pore arrangement is sufficiently dilute so as to neglect interaction between inclusions.

The microstructure of irradiated nuclear fuels is very complicated due to the lack of consistency between bubbles. The intra-granular gas bubbles are two or three order of magnitude smaller than the inter-granular gas bubbles [30]. The shapes of the bubbles are also highly variable: the intra-granular gas bubbles are approximately spherical, whereas inter-granular gas bubbles do not have consistent shapes. In this work, we assess contributions to the thermal conductivity of U-10Mo from both inter- and intra-granular gas bubbles. The impact of xenon bubble pressure on the overall thermal conductivity is also estimated. At the end, we present a study of the influence of different bubble arrangements on the overall thermal conductivity.

2.2   Methods

A finite element model was used to solve the steady-state heat conduction equation in the presence of various microstructures. Two types of microstructures containing xenon gas bubbles were used: a xenon bubble superlattice structure representing intra-granular bubbles, and a grain boundary structure representing inter-granular bubbles. Figure 2.1 shows an example of an intra-granular bubble distribution, while Figure 2.2 shows the inter-granular bubble distribution. In the intra-granular bubble case, xenon gas bubbles were placed in a variety of spatial configurations, including configurations consistent with a gas bubble superlattice. All simulations were performed in a two-dimensional domain. The gas bubble supperlattice structure was created based on data from Miller et al. [6]. According to Miller et al. [6], the bubble size inside the grain boundary superlattice structure is normally distributed. Based on their experimental values, we chose four bubble diame-
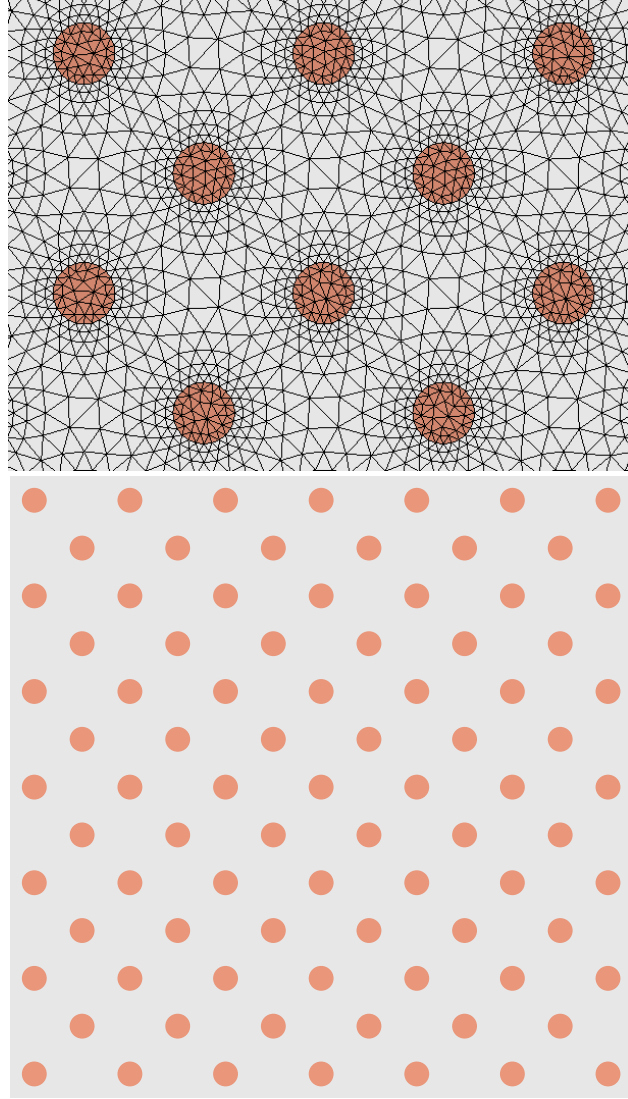
Figure 2.1. (a) Discretized domain of intra-granular xenon bubbles inside a U-10Mo matrix; (b) Example two-dimensional bubble distribution used for intra-granular xenon gas, consisting of bubbles with 3.1, 3.6, 3.75, and 4.0 nm diameters, consistent with the work of Miller and coworkers [6]. The lattice parameter for the gas bubble superlattice is 12.0 nm.

ters to create our simulation. Since the superlattice in U-10Mo is FCC, the two-dimensional structure of bubbles was created based on the FCC structure with a 12 nm lattice parameter, which was also taken from Miller et al. [6]. The bubble sizes were randomly sampled from this distribution using the discrete values of 3.1, 3.6, 3.75, and 4.0 nm in diameter. The square domain's dimensions were 80 nm $\times$ 80 nm, which results in 85 bubbles with a lattice constant of 12 nm. Triangular elements were used to create the mesh using the Trelis Pro software package [31].

In the inter-granular bubble case, the grain boundary structure of U-10Mo was created based on images from Miller et al. [7]. Their SEM (Scanning Electron Micrograph) of a Focused Ion Beam (FIB) cross-section showed fission gas bubbles populating the grain boundaries, as shown in Figure 2.2. This domain was also discretized with triangular elements. The top and bottom boundaries of the domain of the FEM domain were assumed to be adiabatic. The left and right boundary have fixed-temperature boundary conditions applied. This temperature difference drives the heat flow.

The thermal conductivity of U-10Mo was estimated from a linear fit of thermal conductivity as a function of temperature between 298 K and 1073 K from Kaufmann [33]. Burkes et al. [34] also provided a linear fit of the U-10Mo thermal conductivity as a function of temperature up to 873 K; their results were in good agreement with Kaufmann's [33]. The thermal conductivity of xenon depends on both temperature and pressure [32], as shown in Figure 2.3. The pressure inside a bubble depends on the radius of the bubble, the surface tension, the magnitude of the Burgers vector, and the shear modulus of the host material [35, 36]. According to Xiao et al. [37], the pressure inside a xenon bubble can be as high as 120 kbar. Such high pressures suggest the possibility of forming solid xenon bubbles inside the fuel [38–40]. Unfortunately, thermal conductivity data for xenon above 1000 bar are not available, so we chose two limiting sets of thermal conductivity data: 1 bar and 1000 bar. For each set of data, a polynomial fit (fifth order) was used to interpolate the conductivity over the temperature range.
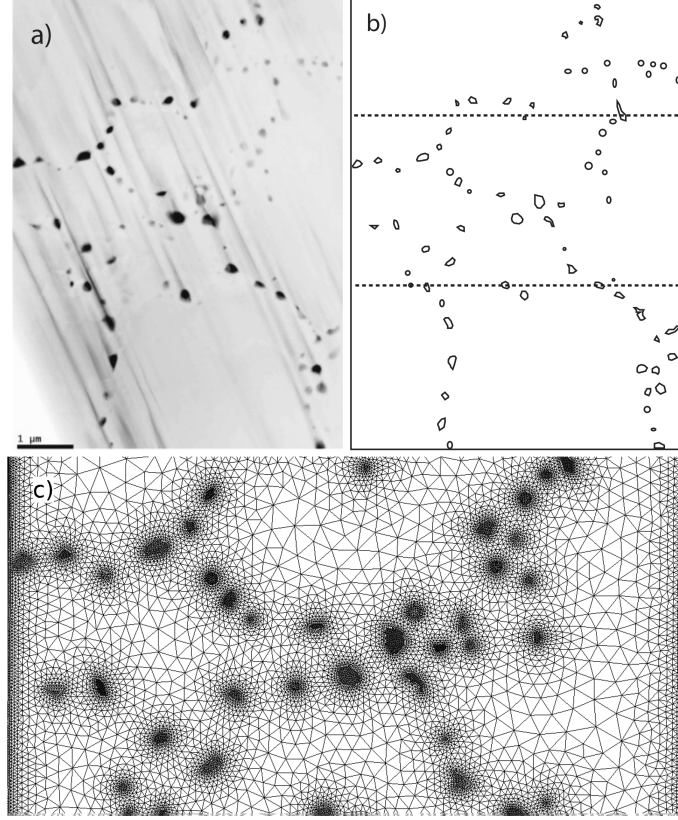
Figure 2.2. (a) SEM image of the fission gas bubbles along the grain boundaries from Miller et al. [7] used for FEM calculations [7] (b) Geometry created based on the grain boundary fission gas image in (a) (c) FEM mesh with grain boundary fission gas of the region between the dotted line in (b)

2.2.1 Effective Thermal Conductivity Calculation

The temperature in a composite material in the absence of heat source is described by the heat equation:

$$\nabla \cdot (K \nabla T) = 0 \tag{2.1}$$

where $K(x, y) = \chi_1(x, y)K_1 + \chi_2(x, y)K_2$ is the thermal conductivity tensor, T is the temperature, K_i ($i = 1$ for the matrix and 2 for the bubble) is the thermal conductivity tensor, and $\chi_i(x, y)$ is the indicator function of phase i. Local heat flux can be calculated using the equation

$$q''(x, y) = -K(x, y) \cdot \nabla T(x, y) \tag{2.2}$$
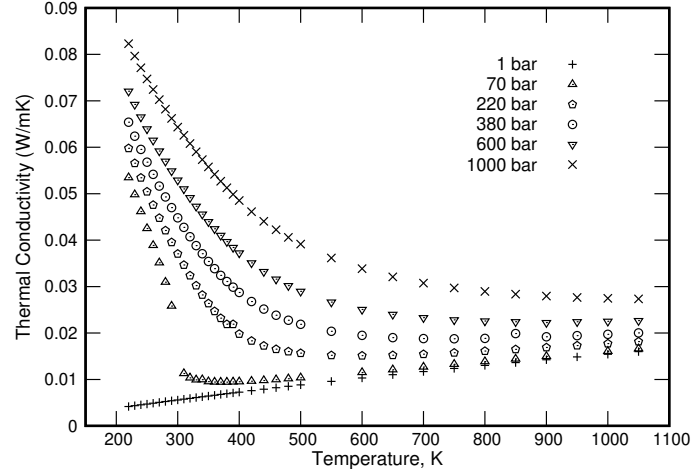
Figure 2.3. Thermal conductivity of xenon as a function of pressure and temperature based on the measurements of Rabinovich et al. [32]. Note that the critical point of xenon is 289.733 K and 58.42 bar; this is why there is such a drastic change in conductivity at low temperature between the 1 bar and 70 bar isobars.

where $q''(x, y)$ is the local heat flux vector and $\nabla T(x, y)$ is the local temperature gradient. Local temperature and heat flux are calculated by solving Equation (2.1) and (2.2). The components of the effective thermal conductivity tensors are calculated via

$$K_{\text{eff}}^x = -q_x'' \left\langle \frac{\partial x}{\partial T} \right\rangle \tag{2.3}$$

Where q_x'' is the mean heat flux in the x direction, and $\left\langle \frac{\partial x}{\partial T} \right\rangle$ is the average inverse temperature gradient in the x direction. The MOOSE Framework [41] was used to solve Equation (2.1) with Dirichlet boundary conditions at $x = 0$ and $x = L$ and Neumann (adiabatic) boundary conditions at $y = 0$ and $y = L$. The effective thermal conductivity was calculated using Equation (2.3).
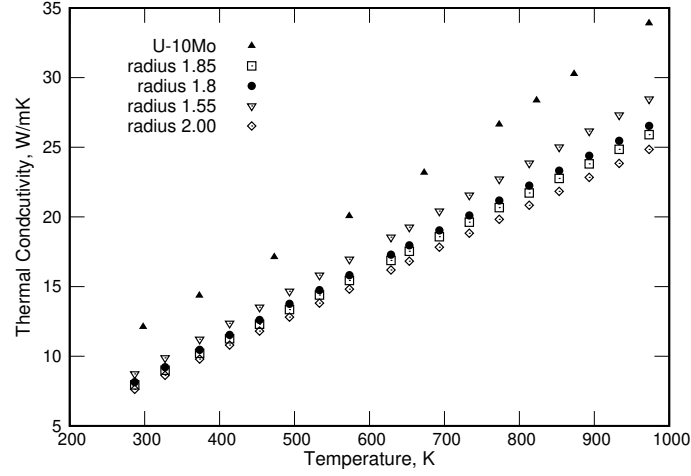
Figure 2.4. Comparison between the thermal conductivity of U-10Mo (from Kaufmann [33]) to the effective thermal conductivity of U-10Mo with intra-granular xenon bubbles of different diameters as arranged in Figure 2.1b.

2.3 Results and Discussion

2.3.1 Effect of Xenon Gas Bubbles on the Thermal Conductivity

We examined two broad categories of bubbles: inter-granular bubbles (i.e., bubbles that collect at grain boundaries), and intra-granular bubbles. The intra-granular case is intended to represent the effect of a gas bubble superlattice (GBS) on the conductivity. We will discuss each case in turn.

2.3.1.1 Intra-Granular Bubbles

A two-dimensional representation of a gas bubble superlattice, as shown in Figure 2.1, was used to simulate the effect of intra-granular bubbles on the thermal conductivity. Five different bubble sizes were used, each with the same superlattice constant (resulting in the same center–center distance between bubbles). Figure 2.4 shows the effective thermal conductivity due to the xenon bubble distribution in the intra-granular region. As is clear from Figure 2.4, the thermal conductivity decreases with increasing bubble size, and is 20–40 percent lower in all cases than it is for bubble-free U-10Mo. In these simulations, the thermal conductivity of xenon was assumed constant at its 1 bar value (it is still a

14

function of temperature). Figure 2.5 shows the result of the finite element method solution compared with the theoretical solution for porous materials' thermal conductivity from the Maxwell–Eucken equation [22],

$$\lambda = \lambda_s \frac{\lambda_p + 2\lambda_s + 2\nu_p(\lambda_p - \lambda_s)}{\lambda_p + 2\lambda_s - \nu_p(\lambda_p - \lambda_s)}, \tag{2.4}$$

where λ is the effective thermal conductivity of the fuel, λ_s is the thermal conductivity of the continuous phase (U-10Mo), λ_p is the thermal conductivity of the dispersed phase (xenon bubble), ν_p is the volume fraction of the dispersed phase (i.e., the volume fraction of xenon in U-10Mo). Equation (2.4) assumes the pore volume fraction is less than 15 percent, that the pores are dispersed uniformly in the solid, and that the distance between the pores is large enough that they do not interact [42, 43]. The result is also compared with the Hashin–Shtrikman upper bound, which is based on a theoretical expression derived for the magnetic permeability of a multiphase material [44],

$$\lambda = \frac{1}{4}\left[\lambda_p(3\nu_p - 1) + \lambda_s(2 - 3\nu_p) + \left(\left[\lambda_p(3\nu_p - 1) + \lambda_s(2 - 3\nu_p)\right]^2 + 8\lambda_s\lambda_p\right)^{\frac{1}{2}}\right]. \tag{2.5}$$

Figure 2.5 shows the effect of distributed gas bubbles in the intra-granular region (grain boundary bubbles were not included). Both theoretical models over-predict the conductivity by 5–10 percent, and the absolute error increases with temperature.

2.3.1.2 Inter-Granular Bubbles

Inter-granular fission gas bubbles are associated with bubbles that collect on or near grain boundaries. Bubbles are naturally drawn to grain boundaries because of the excess volume that accompanies grain boundaries, as well as the decreased energy associated with void formation at grain boundaries relative to the bulk.

To evaluate the effect of inter-granular fission gas on the overall thermal conductivity, Figure 2.2b was used as the simulation domain. As can be seen in Figure 2.2, fission gas
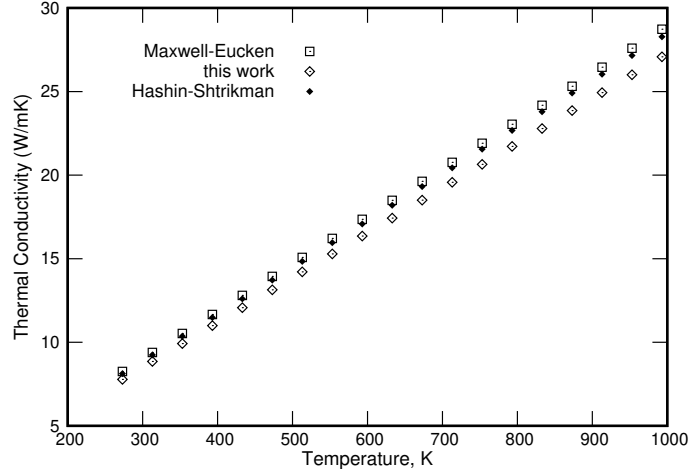
Figure 2.5. Comparison of the calculated effective thermal conductivity of U-10Mo with intra-granular xenon bubble (radius 1.55 nm, 10% porosity) with the Maxwell–Eucken [22] and Hashin–Shtrikman [44] models. In all cases, we find that the two theoretical models over-predict the thermal conductivity by about 5–10 percent compared with the numerical solution.

bubbles trapped on grain boundaries do not have consistent shapes. Note that this is only a snapshot in time of the grain structure: as burnup increases, the stress in the fuel changes, more fission gas is evolved, and the grains can rotate and change shape. For simplicity, the thermal conductivity values at 1 bar were used for xenon.

The presence of these (intra- and inter-granular) xenon bubbles decreased the thermal conductivity by more than 25 percent, as shown in Figure 2.6. According to Miller et al. [7], their sample (on which our simulations are based) went through a fission density of 3.46×10^{21} cm^{-3}. At this fission density, Burkes and coworkers [1] found that the experimental thermal conductivity of U-10Mo reduced to almost 33 percent of its unirradiated value at 473 K. It should be noted that the real material has a three-dimensional grain boundary structure with varying levels of fission gas at each cross section, meaning our estimates of the thermal conductivity (which effectively assume rod-like inclusions rather than spheres) will be too low. Past studies [21, 45] have indicated that conductivity in the presence of inclusions is underestimated in two-dimensional models. This suggests that the measured conductivity (33% of the conductivity of the unirradiated material) may be
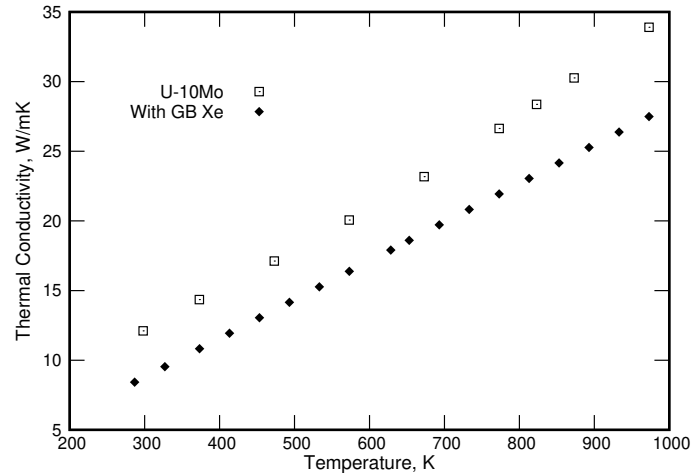
Figure 2.6. Comparison between the thermal conductivity of bubble-free U-10Mo with that of U-10Mo that has xenon bubbles decorating the grain boundaries according to the distribution in Figure 2.2. A 4% drop is observed, increasing with temperature.

reasonably consistent with the conductivity estimated here (i.e., 25% of the conductivity of the unirradiated material).

2.3.2   Effect of Xenon Pressure on the Overall Thermal Conductivity

To evaluate the impact of the pressure of the xenon bubbles on the overall thermal conductivity, we performed a study of the overall conductivity as a function of temperature for five different xenon bubble pressures given a fixed bubble distribution (Figure 2.1b). Each pressure has a distinct thermal conductivity (Figure 2.3) as a function of temperature. In this part of the study, a constant bubble size was used (radius 1.55 nm). The results are shown in Figure 2.7. The results show little to no change of the overall thermal conductivity of the fuel due to the bubbles' pressure over the range studied. However, though xenon has a wide range of thermal conductivities at different pressures (see Figure 2.3), the effect is negligible relative to the thermal conductivity of the fuel.
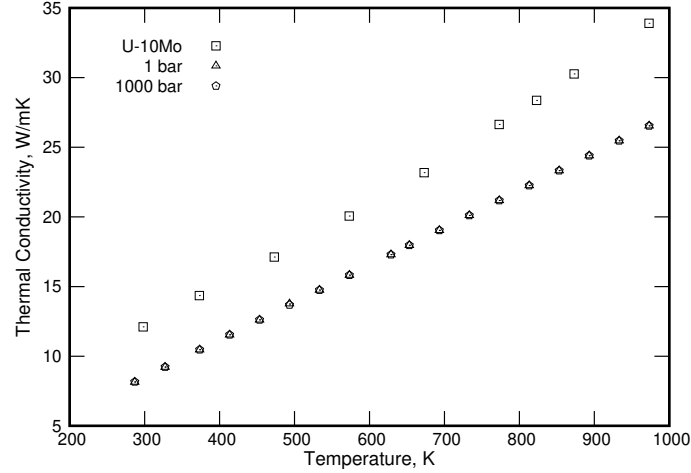
Figure 2.7. Overall thermal conductivity of U-10Mo using the thermal conductivity of xenon at two extremes of pressure (1 bar and 1000 bar), compared to that of pure (bubble-free) U-10Mo. Bubbles are distributed as in Figure 2.1b with radii of 1.55 nm.

2.3.3   Effect of Bubble Arrangement on Thermal Conductivity

We performed a series of simulations to determine whether bubble distribution has a significant influence on the overall thermal conductivity. Two cases were considered. In the first case, we used same number (16) of bubbles of the same diameter (1 nm) and organized them into five different arrangements. The arrangements are arbitrary, but each has the same area fraction of bubbles (xenon gas). In the first arrangement (Figure 2.8a), the bubbles are dispersed uniformly throughout the domain. In Figure 2.8b, the bubbles are arranged in a denser pattern with bubble-free portions near the high-temperature side. In Figure 2.8c, the bubbles are arranged in one corner. In Figure 2.8d, the bubbles are tightly clustered near the center of the domain, creating significant bubble-free regions at the top and bottom. The overall thermal conductivities for these arrangements are presented in Figure 2.9. In these simulations, heat is flowing from left to right, whereas the top and bottom boundaries are insulating (adiabatic).

Based on the results from Figure 2.8, arrangement (d) shows a minor deviation, particularly at high temperatures, compared to the other arrangements. The other four bubble

18
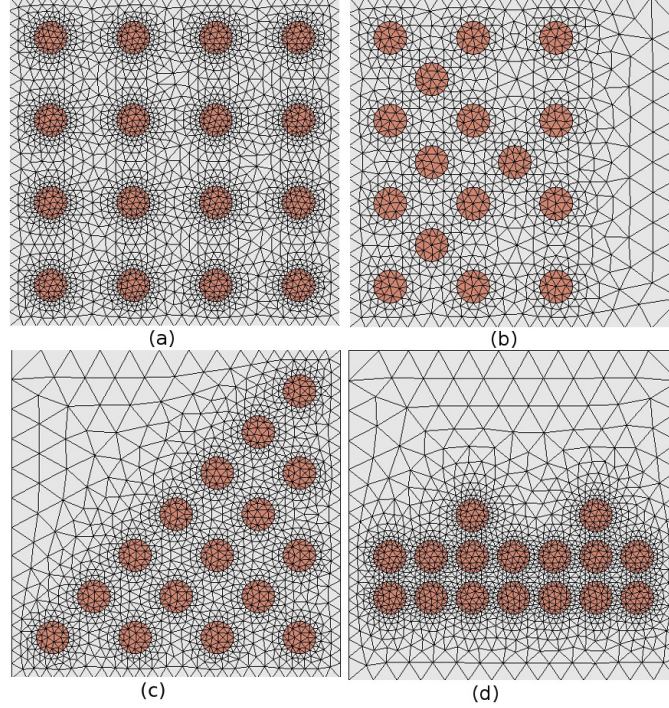
Figure 2.8. Different bubble arrangements in which the area of each bubble and the number of bubbles are the same. Heat flows from left to right in these simulations; only arrangement (d), with its uninterrupted "heat channel" in the top half of the domain, shows significantly different conductivity.

arrangements do not produce significantly different thermal conductivities. The reason for the deviation for case (d) is the relatively wide "heat channel" in the direction of the heat flow, which is absent in the other arrangements. The highest thermal conductivity difference between Figure 2.8d and the other arrangements is approximately 0.93 W/m·K, which is also a function of the open channel's area.

In the second case, different bubble sizes were used with constant total area. As the first case shows, bubble arrangement has minimal impact on the overall heat transfer unless it produces a significant heat transfer channel in direction of the heat flow. In this step, we kept the total area covered by the bubbles the same, but with different sizes of bubbles. To keep the area same while decreasing the bubble diameter, the number of bubbles increases. Figure 2.10 shows the four different arrangements with different bubble sizes. None of
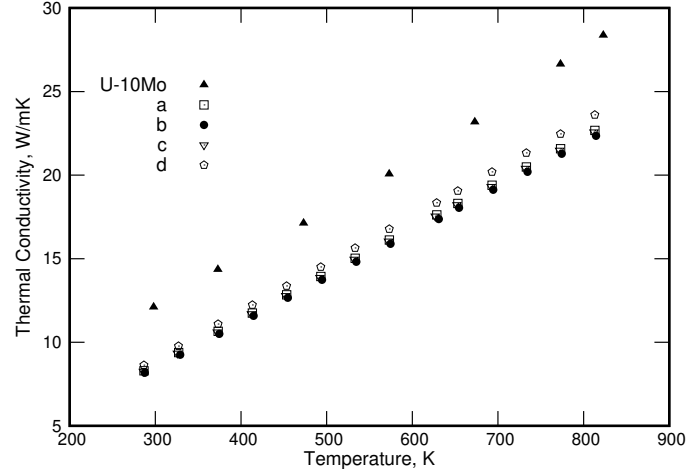
Figure 2.9. Comparison of the calculated thermal conductivity of different bubble arrangements (constant bubble area and diameter). Only arrangement (d), with its properly-oriented "heat channel," shows significant differences from the others, and such differences are relatively insignificant compared to the bubble-free conductivity.

the arrangements creates a heat transfer channel in the direction of heat flow. The results are shown in Figure 2.11. The results show no significant change in the overall thermal conductivity. We conclude that the bubble arrangement has little impact unless it produces a significant bubble-free heat transfer channel.

In our calculation, grain boundary xenon gas bubbles had very minimal impact on the overall heat transfer. That is because our sample has very low grain boundary fission gas areal density, less than 2% of the total area. Grain boundary fission gas bubble size increases with an increase in burnup [5]. With an increase in fission density, more fission gas usually diffuses to the grain boundary area and recrystallization [46] subdivides the grains to accommodate the fission gas near the grain boundaries. This also increases the grain boundary fission gas density. Our results were also compared with porosity correction models, specifically those of Bauer [47] and Peddicord [48]. Bauer's model ($\lambda = \lambda_0 e^{(-2.14v)}$, where λ_0 is the thermal conductivity of the 100% dense material and v is the porosity) over-predicts the porosity correction factor for thermal conductivity. Peddicord's model ($\lambda = \lambda_0(1 - v)^{2.58}$) agrees better with the effective thermal conductivity from
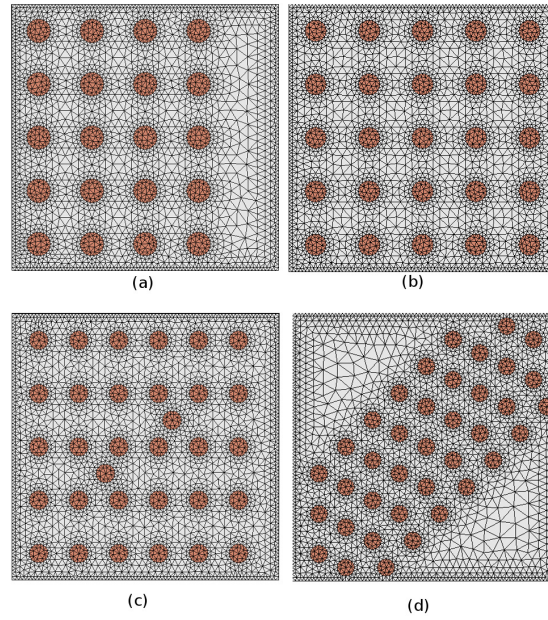
Figure 2.10. Different bubble arrangements where the area is the same but the bubbles have different diameters. (a) 20 bubbles, (b) 25 bubbles, (c) 32 bubbles, (d) 38 bubbles.
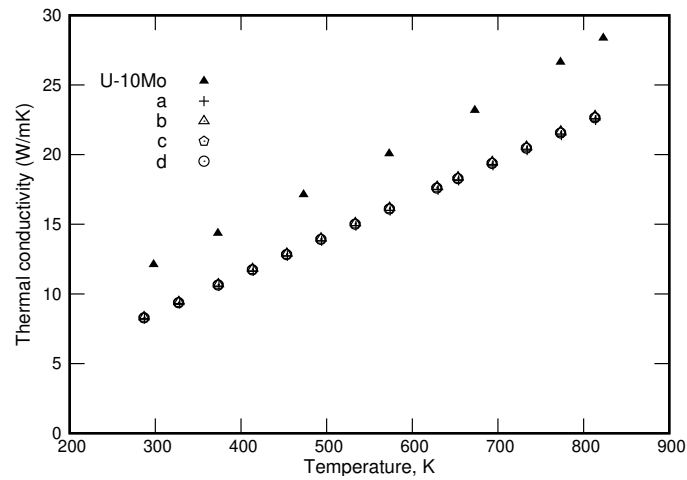
Figure 2.11. Comparison of thermal conductivity between different bubble diameters at constant total bubble area with bubble-free U-10Mo. Bubble arrangements are shown in Figure 2.10. Bubble diameters are (a) 0.894 nm (b) 0.8 nm (c) 0.707 nm and (d) 0.6488 nm; the bubble area fraction is 12.6% percent.

our simulations. All these empirical models are applicable to intragranular gas bubbles with uniform distribution and negligible fission gas thermal conductivity. In our calculation, all the thermal conductivities are measured from two-dimensional finite element models, but two-dimensional thermal conductivity usually represents the lower limit of the three-dimensional thermal conductivity [49]. Accurate estimation of this limit is very important.

2.4   Conclusions

Estimating the thermal conductivity of nuclear fuel is an important part of understanding fuel behavior in nuclear reactors. In our work, xenon gas was used to represent fission gas bubbles in U-10Mo monolithic fuels. The impact of distributed xenon bubbles on the overall thermal conductivity of U-10Mo is significant, resulting in a 25–35 percent drop in conductivity for the bubble volume fractions studied, largely independent of bubble arrangement. Both intra- and inter-granular gas bubble structures were used. For intragranular bubbles, a gas bubble superlattice structure was used. The results indicate that the Maxwell–Eucken and Hashin–Shtrikman models overestimate thermal conductivities by at least 5% for the bubble volume fraction studied.

The pressure dependence of xenon's thermal conductivity was also studied to estimate the impact of bubble pressure on the overall thermal conductivity of U-10Mo. Our results indicate that bubble pressure is not a significant factor for the bubble densities studied—the overall thermal conductivity remains largely unchanged between 1 bar and 1000 bar.

We find that both intra- and inter-granular xenon bubbles reduce the overall thermal conductivity by more than 25 percent. Different bubble arrangements have very little impact on the overall heat flow, unless the arrangement leads to a significant bubble-free channel through which heat can be conducted without interference from nearby bubbles. Bubble size is also not a significant factor, as different bubble sizes at the same bubble areal density produce a U-10Mo slab with identical overall conductivity.

References

1. Douglas E. Burkes, Andrew M. Casella, Amanda J. Casella, Edgar C. Buck, Karl N. Pool, Paul J. MacFarlan, Matthew K. Edwards, and Frances N. Smith. Thermal properties of U–Mo alloys irradiated to moderate burnup and power. *J. Nucl. Mater.*, 464:331–341, 2015.

2. Vincenzo V. Rondinella and Thierry Wiss. The high burn-up structure in nuclear fuel. *Mater. Today*, 13(12):24–32, 2010.

3. A. T. Blades, W. H. Fleming, and H. G. Thode. The ratio of xenon to krypton in U^{235} fission. *Can. J. Chem.*, 34(3):233–237, 1956.

4. J. A. Petruska, H. G. Thode, and R. H. Tomlinson. The absolute fission yields of twenty-eight mass chains in the thermal neutron fission of U^{235}. *Can. J. Phys.*, 33(11):693–706, 1955.

5. Yeon Soo Kim and G. L. Hofman. Fission product induced swelling of U–Mo alloy fuel. *J. Nucl. Mater.*, 419(1):291–301, 2011.

6. B. D. Miller, J. Gan, D. D. Keiser, Jr, A. B. Robinson, J. F. Jue, J. W. Madden, and P. G. Medvedev. Transmission electron microscopy characterization of the fission gas bubble superlattice in irradiated U–7wt% Mo dispersion fuels. *J. Nucl. Mater.*, 458:115–121, 2015.

7. Brandon D. Miller, Jian Gan, James Madden, Jan-Fong Jue, A. Robinson, and D. D. Keiser. Advantages and disadvantages of using a focused ion beam to prepare TEM samples from irradiated U–10Mo monolithic nuclear fuel. *J. Nucl. Mater.*, 424(1):38–42, 2012.

8. Jian Gan, D. D. Keiser, Dan M. Wachs, Adam B. Robinson, Brandon D. Miller, and Todd R. Allen. Transmission electron microscopy characterization of irradiated U–7Mo/Al–2Si dispersion fuel. *J. Nucl. Mater.*, 396(2):234–239, 2010.

9. Jian Gan, D. D. Keiser, Brandon D. Miller, Adam B. Robinson, Jan-Fong Jue, Pavel Medvedev, and Dan M. Wachs. TEM characterization of U–7Mo/Al–2Si dispersion fuel irradiated to intermediate and high fission densities. *J. Nucl. Mater.*, 424(1):43–50, 2012.

10. P. B. Johnson and D. J. Mazey. The gas-bubble superlattice and the development of surface structure in He^+ and H irradiated metals at 300 K. *J. Nucl. Mater.*, 93–94:721–727, 1980.

11. P. B. Johnson and D. J. Mazey. Hydrogen gas-bubble structure in proton-irradiated copper at 300 K. *J. Nucl. Mater.*, 91(1):41–46, 1980.

12. J. H. Evans. Void and bubble lattice formation in molybdenum: A mechanism based on two-dimensional self-interstitial diffusion. *J. Nucl. Mater.*, 119(2–3):180–188, 1983.

13. D. J. Mazey and J. H. Evans. Bubble lattice formation in titanium injected with krypton ions. *J. Nucl. Mater.*, 138(1):16–18, 1986.

14. J. H. Evans and D. J. Mazey. Solid bubble formation in titanium injected with krypton ions. *J. Nucl. Mater.*, 138(2-3):176–184, 1986.

15. P. B. Johnson, K. J. Stevens, and R. W. Thomson. Image processing techniques in the study of ordered bubble arrays: Bubble facetting in vanadium. *Nucl. Instrum. Meth. Phys. Res. B*, 62(2):218–227, 1991.

16. P. B. Johnson and D. J. Mazey. Gas-bubble superlattice formation in bcc metals. *J. Nucl. Mater.*, 218(3):273–288, 1995.

17. F. E. Lawson and P. B. Johnson. A temperature threshold for gas-bubble superlattice formation in molybdenum. *J. Nucl. Mater.*, 252(1-2):34–42, 1998.

18. N. M. Ghoniem, Daniel Walgraef, and S. J. Zinkle. Theory and experiment of nanostructure self-organization in irradiated materials. 8(1):1–38, 2001.

19. P. B. Johnson and Fenella Lawson. Helium gas-bubble superlattice formation in molybdenum. *Nucl. Instrum. Meth. Phys. Res. B*, 243(2):325–334, 2006.

20. J. Gan, D. D. Keiser, Jr., B. D. Miller, A. B. Robinson, D. M. Wachs, and M. K. Meyer. Thermal stability of fission gas bubble superlattice in irradiated U–10Mo fuel. *J. Nucl. Mater.*, 464:1–5, September 2015.

21. K. Bakker. Using the finite element method to compute the influence of complex porosity and inclusion structures on the thermal and electrical conductivity. *Int. J. Heat Mass Tran.*, 40(15):3503–3511, 1997.

22. James Clerk Maxwell. *A Treatise on Electricity and Magnetism*, volume 1. Clarendon Press, Oxford, 1881.

23. J. B. MacEwan, R. L. Stoute, and M. J. F. Notley. Effect of porosity on the thermal conductivity of UO_2. *J. Nucl. Mater.*, 24(1):109–112, 1967.

24. L. A. Goldsmith and J. A. M. Douglas. Measurements of the thermal conductivity of uranium dioxide at 670–1270 K. *J. Nucl. Mater.*, 47(1):31–42, 1973.

25. M. F. DeVries. An experimental determination of the thermal conductivity of a 304L stainless steel powder metallurgy material. *J. Heat Tran.*, 111:281, 1989.

26. Arthur L. Loeb. Thermal conductivity: VIII, A theory of thermal conductivity of porous materials. *J. Am. Ceram. Soc.*, 37(2):96–99, 1954.

27. M. E. Cunningham and K. L. Peddicord. Heat conduction in spheres packed in an infinite regular cubical array. *Int. J. Heat Mass Tran.*, 24(7):1081–1088, 1981.

28. Da Yu Tzou. The effect of internal heat transfer in cavities on the overall thermal conductivity. *Int. J. Heat Mass Tran.*, 34(7):1839–1846, 1991.

29. T. H. Bauer. A general analytical approach toward the thermal conductivity of porous media. *Int. J. Heat Mass Tran.*, 36(17):4181–4191, 1993.

30. Shenyang Hu, Andrew M. Casella, Curt A. Lavender, David J. Senor, and Douglas E. Burkes. Assessment of effective thermal conductivity in U–Mo metallic fuels with distributed gas bubbles. *J. Nucl. Mater.*, 462:64–76, 2015.

31. Trellis Pro. Computational simulation software. csimsoft, LLC., American Fork, Utah, 2012–2017.

32. Viktor Abramovich Rabinovich, A. A. Vasserman, V. I. Nedostup, and Lo S. Veksler. *Thermophysical Properties of Neon, Argon, Krypton, and Xenon*. Hemisphere Publishing Corporation, New York, NY, 1987.

33. Albert R. Kaufmann. *Nuclear Reactor Fuel Elements: Metallurgy and Fabrication*. Interscience Publishers, New York, 1962.

34. Douglas E Burkes, Cynthia A Papesch, Andrew P Maddison, Thomas Hartmann, and Francine J Rice. Thermo-physical properties of DU–10wt.% Mo alloys. *J. Nucl. Mater.*, 403(1):160–166, 2010.

35. G. W. Greenwood, A. J. E. Foreman, and D. E. Rimmer. The role of vacancies and dislocations in the nucleation and growth of gas bubbles in irradiated fissile material. *J. Nucl. Mater.*, 1(4):305–324, 1959.

36. H. Trinkaus. Energetics and formation kinetics of helium bubbles in metals. *Radiat. Eff.*, 78(1–4):189–211, 1983.

37. Hongxing Xiao, Chongsheng Long, Xiaofeng Tian, and Shujian Li. Atomistic simulations of the small xenon bubble behavior in U–Mo alloy. *Mater. Des.*, 74:55–60, 2015.

38. L. E. Thomas. Condensed-phase xenon and krypton in UO_2 spent fuel. In *Fundamental Aspects of Inert Gases in Solids*, pages 431–441. Springer, New York, 1991.

39. M. Ross and A. K. McMahan. Condensed xenon at high pressure. *Phys. Rev. B*, 21(4):1658–1664, 1980.

40. J. Zheng, Q. F. Chen, Y. J. Gu, Z. Y. Chen, and C. J. Li. Thermodynamics, compressibility, and phase diagram: Shock compression of supercritical fluid xenon. *J. Chem. Phys.*, 141(12):124, 2014.

41. Derek Gaston, Chris Newman, Glen Hansen, and Damien Lebrun-Grandie. MOOSE: A parallel computational framework for coupled systems of nonlinear equations. *Nucl. Eng. Des.*, 239(10):1768–1778, 2009.

42. C. R. Clark, G. C. Knighton, M. K. Meyer, and G. L. Hofman. Monolithic fuel plate development at Argonne National Laboratory. In *2003 International Meeting on Reduced Enrichment for Research and Test Reactors*, volume 1, Chicago, Illinois, October 2003.

43. David S. Smith, Arnaud Alzina, Julie Bourret, Benoît Nait-Ali, Fabienne Pennec, Nicolas Tessier-Doyen, Kodai Otsu, Hideaki Matsubara, Pierre Elser, and Urs. T. Gonzenbach. Thermal conductivity of porous materials. *J. Mater. Res.*, 28(17):2260–2272, 2013.

44. Zvi Hashin and Shmuel Shtrikman. A variational approach to the theory of the effective magnetic permeability of multiphase materials. *J. Appl. Phys.*, 33(10):3125–3131, 1962.

45. Brigitte Schulz. Thermal conductivity of porous and highly porous. *High Temp. High Press.*, 13:649–660, 1981.

46. Yeon Soo Kim, G.L. Hofman, and J. S. Cheon. Recrystallization and fission-gas-bubble swelling of U–Mo fuel. *J. Nucl. Mater.*, 436(1):14–22, 2013.

47. Theodore H. Bauer and John W. Holland. In-pile measurement of the thermal conductivity of irradiated metallic fuel. *Nucl. Technol.*, 110(3):407–421, 1995.

48. K. L. Peddicord, M. E. Cunningham, and A Tripathi. Porosity correction to thermal conductivity based on analytical temperature solutions. *Trans. Am. Nucl. Soc.*, 28:548, 1978.

49. K. Bakker, H. Kwast, and E. H. P. Cordfunke. Determination of a porosity correction factor for the thermal conductivity of irradiated UO_2 fuel by means of the finite element method. *J. Nucl. Mater.*, 226(1–2):128–143, 1995.

CHAPTER 3

FIRST-PRINCIPLES STUDY OF METALLIC URANIUM

A portion of this chapter was published as an article in Computational Material Science. The authors are A. Rafi M. Iasir and Karl D. Hammond of the University of Missouri.

3.1 Introduction

Uranium is the heaviest naturally-occurring element on Earth. The discovery of fission in uranium (specifically, in ^{235}U) impacted not only scientists and engineers all over the world, it also changed global politics forever. In nuclear research, the nucleus of the uranium atom is of much more importance than the electrons surrounding it, but the electronic structure is important to the thermodynamic properties, including crystal structure. The structural features are particularly important to the study of next-generation nuclear fuels, such as U-10Mo, that are based on metallic uranium. The electronic behavior of uranium, along with other light actinides (Pa–Pu), results in a low-symmetry crystal structure at ambient temperature and pressure—most metallic elements take on relatively high-symmetry structures (bcc, fcc, and hcp), but the light actinides are either orthorhombic or monoclinic at standard temperature and pressure. Pure uranium exists in three different solid phases at atmospheric pressure, depending on the temperature: α (base-centered orthorhombic), β (tetragonal) and γ (body-centered cubic). At atmospheric pressure, α-U transforms to β-U at approximately 935 K, and β-U transforms to γ-U at approximately 1045 K [1, 2]. The influence of $5f$ electron–electron correlation plays a pivotal role in the crystallographic be-

havior of uranium and other light actinides [3, 4]; with this in mind, proper representation of uranium's $5f$ electrons is very important.

The stability of the crystal structures of the inner transition metals has been the target of several electronic structure studies. Eriksson and coworkers [5, 6] performed comparative studies of thorium, protactinium, and uranium's crystal structures, calculating the equilibrium volume and bulk modulus using the full-potential linear-muffin-tin-orbital (FP-LMTO) technique and the local density approximation (LDA). The calculated lattice parameters and equilibrium unit cell volumes showed good agreement with experiments; the bulk modulus of protactinium was significantly underestimated, but the values for uranium and thorium were within the range of experimental values. Crocombette *et al.* [7] used norm-conserving pseudopotentials to study three metallic phases of uranium (α, γ, and a hypothetical fcc structure). The calculated equilibrium volume for α uranium was underestimated by more than 6 percent. Söderlind [8] calculated the equilibrium lattice parameters and also estimated the elastic moduli of α uranium using the FP-LMTO method. The calculated equilibrium lattice parameters were in good agreement with experimental values, but the elastic moduli did not agree particularly well with experimental values. The calculated elastic moduli were likely higher than experimental values because uranium undergoes strong phonon softening with increases in temperature, and the experimental values (taken at room temperature) would likely be lower than they would be at low temperatures [9].

Söderlind's [8] was the first attempt to calculate α-uranium's elastic moduli. Other theoretical studies of light actinides prior to 2000 using full-core (*i.e.*, non-pseudopotential-based) techniques are summarized by Jones *et al.* [10]. Taylor [11] studied uranium phases using the projector augmented-wave (PAW) method [12] with Perdew and Wang's 1991 (PW91) exchange–correlation functional [13, 14]. Taylor investigated α, bcc, and fcc uranium. The equilibrium lattice parameters of α-uranium were within 1% of experimental values at 50 K [15]. The lattice parameter of γ-uranium was also in good agreement with experimental values, though the lattice parameter of fcc uranium was overestimated com-

pared to the value calculated by Crocombette *et al*. [7]. Xiang *et al*. [16] used the Perdew–Burke–Ernzerhof (PBE) exchange–correlation functional [17, 18] to study the equilibrium volume of the α and γ uranium. He also studied the bct structure, an approximation of the β phase. Their results were also in good agreement with previous full potential studies and experimental results. Li *et al*. [19] also studied the structure, formation energies, and elastic moduli of α, β, γ, fcc, and hcp uranium using the PW91 exchange–correlation functional. Their pseudopotential produced reasonably accurate lattice parameters and cell volumes for γ-uranium and α-uranium accompanied by reasonable elastic moduli. Beeler *et al*. [20] utilized the PBE exchange–correlation functional to study uranium, and found similar values to Li *et al*., with the exception of the body-centered tetragonal case (approximating β-uranium).

In the present work, we investigate the crystal structure and elastic properties of metallic uranium with density functional theory (DFT) with a projector augmented wave (PAW) pseudopotential [12]. We investigate four structures of uranium: α, γ, bct, and fcc. Our results are compared with previously published electronic structure calculations and experiments. The electronic densities of states for all four crystal structures are also calculated. Our results for α-uranium are comparable to previous models, but predicted properties for γ-uranium are, in general, improvements on previously-published models.

3.2 The Many-Body Hamiltonian

The quantum theory of electrons and nuclei controls the characteristics of matter over wide ranges in temperature and pressure. One of the most fundamental qualities of solid is that it has a variety of properties which are not featured by a single atom. Electric conductivity as well as magnetism arise as collective properties of the particle in the system. The particles of a solid can be described by the Schrödinger's equation

$$\mathcal{H}\,|\Psi(t)\rangle = i\hbar\frac{\partial}{\partial t}\,|\Psi(t)\rangle\,, \tag{3.1}$$

The time-independent Schrödinger equation is as follows:

$$\mathcal{H} \left| \psi_j \right\rangle = E_j \left| \psi_j \right\rangle \tag{3.2}$$

where the Hamiltonian expresses the motion of the particles:

$$
\begin{aligned}
\mathcal{H} = &- \sum_j \frac{\hbar^2}{2m_e} \nabla_j^2 - \sum_a \frac{\hbar^2}{2M_a} \nabla_a^2 \\
&- \sum_{j,a} \frac{Z_a e^2}{\left| \mathbf{r}_j - \mathbf{R}_a \right|} + \frac{1}{2} \sum_{j,k}^{j \neq k} \frac{e^2}{\left| \mathbf{r}_j - \mathbf{r}_k \right|} + \frac{1}{2} \sum_{a,b}^{a \neq b} \frac{Z_a Z_b e^2}{\left| \mathbf{R}_a - \mathbf{R}_b \right|} \\
\mathcal{H} \overset{Htr.\ units}{=} &- \sum_j \frac{1}{2} \nabla_j^2 - \sum_a \frac{1}{2\tilde{M}_a} \nabla_a^2 \\
&- \sum_{j,a} \frac{Z_a}{\left| \mathbf{r}_j - \mathbf{R}_a \right|} + \frac{1}{2} \sum_{j,k}^{j \neq k} \frac{1}{\left| \mathbf{r}_j - \mathbf{r}_k \right|} + \frac{1}{2} \sum_{a,b}^{a \neq b} \frac{Z_a Z_b}{\left| \mathbf{R}_a - \mathbf{R}_b \right|} \\
= &\ T_e + T_N \\
&+ V_{Ne}(\mathbf{r}, \mathbf{R}) + V_{ee}(\mathbf{r}) + V_{NN}(\mathbf{r})
\end{aligned}
\tag{3.3}
$$

The second part of the equation is expressed in Hatree units (see Appendix A), which will be used for the remainder of the discussion. In these units, the electron mass m_e as well as the elementary charge e, the reduced Planck's constant $\hbar$ and Coulomb's constant $1/4\pi\epsilon_0$ are set to unity, leaving $\tilde{M}_a = M_a/m_e$ as the relative atomic mass of the nucleus of atom a. $\mathbf{r}_j$ denotes the position of the j-th electron, while $\mathbf{R}_a$ is the position of the nucleus of atom a. Z_a is that nucleus' charge number. A solution of the Schrödinger equation (3.2) would be a function dependent on the spatial coordinates of all particles in the system and is as such only obtainable for very small systems. The Schrödinger equation with the above Hamiltonian is impossible to solve exactly for most of systems of interest. A series of approximations and methods were therefore developed to reduce the complexity of the problem. With the help of Eqn (3.3) the Schrödinger equation (3.2) becomes

$$[T_e + T_N + V_{Ne}(\mathbf{r}, \mathbf{R}) + V_{ee}(\mathbf{r}) + V_{NN}(\mathbf{r})]\Phi(\mathbf{r}, \mathbf{R}) = E\Phi(\mathbf{r}, \mathbf{R}) \tag{3.4}$$

In order to simplify the equations, the electronic coordinates and spin indices are combined into a vector $\mathbf{r} = (\vec{r}, s)$ and $\mathbf{R}$ denotes the nuclear coordinates. The wave function here is a regular function of the atomic positions but a quantum state $|\Phi(x, t)\rangle$ in the Hilbert space for the electrons and nuclei, so that $\Phi(\vec{r}) = \langle\vec{r}|\Phi(\mathbf{r}, \mathbf{R})\rangle$. The nuclear mass exceeds the electron mass by more than three orders of magnitude, and so both move on different time scales. Thus the wave function $\Phi(\mathbf{r}, \mathbf{R})$ can be separated into an electronic part $\Psi(\mathbf{r}, \mathbf{R})$ and a nuclear wave function $\chi(\mathbf{R})$

$$\Phi(\mathbf{r}, \mathbf{R}) = \Psi(\mathbf{r}, \mathbf{R})\chi(\mathbf{R}) \tag{3.5}$$

The nuclear wave function is much more localized, which is why the Schrödinger equation can be separated into two parts:

$$[T_e + V_{ee}(\mathbf{r}) + V_{Ne}(\mathbf{r}, \mathbf{R})]\Psi(\mathbf{r}, \mathbf{R}) = \epsilon_n(\mathbf{R})\Psi(\mathbf{r}, R) \tag{3.6}$$

$$[T_N + V_{NN}(\mathbf{R}) + \epsilon_n(\mathbf{R})]\chi(\mathbf{r}) = E\chi(\mathbf{R}) \tag{3.7}$$

The nuclear positions ($\mathbf{R}$) in the equation (3.6) servs only as a parameter and it is possible to use the *adiabatic* or *Born-Oppenheimer* approximation. On the timescale of the nuclar motion the electron follow the ions adiabatically. As a further approximation, the quantum effects on the motion of the nuclei are neglected and time dependent Schrödinger equation is replaced by Newton's equation of motion:

$$\frac{\partial P_I}{\partial t} = -\nabla_I E_0(\mathbf{R}) \tag{3.8}$$

$$with \quad E_0(\mathbf{R}) = \epsilon_0(\mathbf{R}) + V_{NN}(\mathbf{R}) \tag{3.9}$$

This refers to the so called *ab-initio* molecular dynamics, where the forces around a nuclei are calculated from the electronic groudn state.

Equation 3.6 and 3.7 are not generally applicable. However, for several physical systems, the Born-Oppenheimer approximation works and Eqn. 3.6, 3.7 produces meaningful results. In solid state physics, Eqn (3.7) usually written in a classical form and Eqn (3.6) becomes the problem to be solved. It is still a very complicated equation, where the term describing the interaction between electrons would require the knowledge of 3^N variables for a sysmtem of N electrons. Such a large number of variables make the problem computationally not tractable and several approximated methods have been introduced. Some of those important methods will be discussed.

These approximation methods are based on the *independent particle* approximation, in which the Hamiltonian takes the form

$$\mathcal{H}' = \sum_j \mathcal{H}_j \tag{3.10}$$

The electrons wave function can be written as products of single particle wave functions. This leads to a further simplification of the Hamiltonian.

$$\mathcal{H}' \stackrel{\text{eqn.3.6}}{=} -\sum_j^N \frac{1}{2}\nabla_j^2 - \sum_j^N \sum_a^M \frac{Z_a}{|\mathbf{r}_j - \mathbf{R}_a|} + \frac{1}{2}\sum_{j\neq k}^N \sum_k^N \frac{1}{|\mathbf{r}_j - \mathbf{r}_k|}$$
$$= T_e + V^{\text{ext}} + \frac{1}{2}\sum_{j\neq k} \upsilon_{jk}(|\mathbf{r}_j - \mathbf{r}_k|) \tag{3.11}$$

3.3 Hartree-Fock Approach

A very simple way to write many-electron wavefunction is as a product of single-particle wavefunction:

$$\Psi(r_1, r_2, \ldots, r_N) = \prod_j^N \psi_j(r_j) \tag{3.12}$$

The Hamiltonian (3.11) is not just a sum of single-particle Hamiltonians, the true wave-functions cannot be written in the product of the form (3.12), furthermore, it does not have the *antisymmetry* property required for fermions.

The fermionic nature of the electrons imposes the Pauli exclusion principle as an additional constraint. One can achieve that by constructing a many-body wave function in an antisymmetric manner. This is achieved by writing the electronic wave function as a Slater determinant of single-paricle wave functions:

$$\Psi(r_1, r_2, \ldots, r_N) = \frac{1}{\sqrt{N!}} \begin{vmatrix} \psi_1(\mathbf{r}_1) & \psi_1(\mathbf{r}_2) & \ldots & \psi_1(\mathbf{r}_N) \\ \psi_2(\mathbf{r}_2) & \psi_2(\mathbf{r}_2) & \ldots & \\ \vdots & & \ddots & \\ \psi_N(\mathbf{r}_1) & & \ldots & \psi_N(\mathbf{r}_N) \end{vmatrix} \tag{3.13}$$

The expectation value of the Hamiltonian (3.11) can be calculated using the newly introduced wave function, which leads to an energy functional that can be minimised variationally (3.14). Additional constraints for the single particle orbitals is to be normalized (3.15).

$$E \leq E' \equiv \frac{\langle \Psi | H | \Psi \rangle}{\langle \Psi | \Psi \rangle} = \tag{3.14}$$

Here, for any state $|\Psi\rangle$ provides an upper bound E' for the exac ground-state energy E. The orthonormalization conditions,

$$\left\langle \psi_i(\mathbf{r}_i) \middle| \psi_j(\mathbf{r}_j) \right\rangle = \int d\mathbf{r}\, \psi_i(\mathbf{r})^* \psi_j(\mathbf{r}) = \delta_{ij} \tag{3.15}$$

The many-particle wave function (3.13) and the Hamiltonian (3.11) give the single particle Hatree-Fock[1](HF) Equations:

$$\mathcal{H}_i^{\text{HF}} \psi_i(\mathbf{r}_i) = \left[-\frac{\nabla^2}{2} + v^{\text{ext}}(\mathbf{r}_i) + v^{\text{H}}(\mathbf{r}_i) + v^{\text{EX}}(\mathbf{r}_i) \right] \psi_i(\mathbf{r}_i)$$

$$= \epsilon_i \psi_i(\mathbf{r}_i) \tag{3.16}$$

where the kinetic energy term T_e and the external potential V^{ext} are unchanged from Eqn (3.11), are divided into the single particle constributions, with $V^{\text{ext}} = \sum_{i=1}^{N} v^{\text{ext}}(\mathbf{r}_i)$. The third term in Eqn (3.11), the interaction between the electrons, produces two additional operators v^{H} and v^{EX}. The first term in called the *Hartree potential* and has the following form:

$$v^{\text{H}}(\mathbf{r}_i) = \sum_{j=1}^{N} \int \frac{\left| \psi_j(\mathbf{r}_j)^2 \right|}{\left| \mathbf{r}_i - \mathbf{r}_j \right|} d\mathbf{r}_j$$

$$= \int \frac{n(\mathbf{r}_j)}{\left| \mathbf{r}_i - \mathbf{r}_j \right|} d\mathbf{r}_j \tag{3.17}$$

where

$$n(\mathbf{r}) = N \int d\mathbf{r}_1, \ldots, d\mathbf{r}_N \left| \Psi^0(\mathbf{r}_1, \ldots, \mathbf{r}_N) \right|^2 \tag{3.18}$$

It takes account of the mean-field Coulomb interaction between the i th electron and the total electron density $n(\mathbf{r})$ as defined in Eqn (3.17). The second term in Eqn (3.16) can be written in its integral form

$$v^{\text{EX}} \psi_i(\mathbf{r}_i) = \sum_{j=1}^{N} \int d\mathbf{r}_j \psi_j^*(\mathbf{r}_j) \frac{1}{\left| \mathbf{r}_i - \mathbf{r}_j \right|} \psi_j(\mathbf{r}_i) \psi_i(\mathbf{r}_j) \tag{3.19}$$

It is known as *exchange potential* and takes account the antisymmetric nature of the total wave function. When the two particles have same coordinates the Hatree and exchange potential cancel each other.

The solution of the Hatree-Fock equation are the HF orbitals. Since the orbitals are also part of the equation the problem needs to be solved self-consistently. The exchange oper-

ator v^{EX} is usually referred to as a non-local operator, which makes it impossible to carry out full HF calculations for condensed matter system without introducing the local approximations. Evaluating v^{EX} is already a non trivial task, but the HF equation approximates the full many-body problem in a way that leaves out important contributions. What is not considered is usually referred to as *correlation* which adds an extra term in the Hamiltonian form (3.16). This contribution is small compared to the total energy of the system, but it is crucial for many solid systems. The *correlation* contribution to the Hamiltonian takes mainly account of the fact that one electron is screened by others from the interaction with the nuclei and more distant electrons. The HF method is usually works for system in which the particle do not "see" each other. HF performs badly for systems with large number of electrons in metals.

3.4 Density Functional Theory

In the Hatree-Fock approach where we used wave-functions to solve many-body problem which is solved self-consistly. The density $n(\mathbf{r})$ plays a prominent role in self-consistent calculations. This evokes the query as to whether there exists an *exact* theory for the ground state electronic system of the density $n(\mathbf{r})$. This question leads to the *density functional theory* (DFT). The simplest and oldest version of the DFT formalism is the Thomas-Fermi model [24, 25].

3.4.1 Density

The idea to shift focus from wavefunction ($\Psi(\mathbf{r})$) to denisty ($n(\mathbf{r})$) to solve many-body Schrödinger equation is very important. For many particle system the density, $n(\mathbf{r})$, is calculated by the expectatioin value of the single-particle density operator for many-body wavefunction.

$$\hat{n}(\mathbf{r}) = \sum_i^N \delta(\mathbf{r} - \mathbf{r}_i) \tag{3.20}$$

[1]From Hatree [21], who first postulated the factorization of the wave function in single particle states in 1928, and Fock [22], who redefined the method by including Slater determinant.

The density can be calculated as follows:

$$n(\mathbf{r}) = \langle \Psi | \hat{n}(\mathbf{r}) | \Psi \rangle = \sum_i^N \int \delta(\mathbf{r} - \mathbf{r}_i) |\Psi(\mathbf{r}_1, \ldots, \mathbf{r}_N)|^2$$
$$= N \int |\Psi(\mathbf{r}_2, \ldots, \mathbf{r}_N)|^2 \tag{3.21}$$

where $\mathbf{r}_i$ are the variable associated with each of the electrons. Assuming the wavefunction is normalised to unity, the above integration over all the space yields the total number of electrons.

$$\int d\mathbf{r} n(\mathbf{r}) = N \tag{3.22}$$

3.4.2 Energy in Terms of the Density

It is necessary to represent all the energy in terms of density to eliminate wavefunction dependency. This is necessary because the electronic energy needs to be minimized with respect to density to obtain the ground state energy and corresponding electronic density. This is one of the foundations of DFT that was proposed by Hohenberg and Kohn in 1964 [23].

As we have discussed earlier (HF theory), once the wavefunction is obtained by solving the Hamiltonian the observable of other operator can be calculated by calculating the expectation value of the operator. This allows to calculate the separate the energy terms associated to the potential operator given in the Hamiltonian (3.11). For the sake of completeness lets reproduce the Hamiltonian in a simplest form

$$\hat{\mathcal{H}}_e = \hat{T} + \hat{V}_{en} + \hat{V}_{ee}$$
$$\stackrel{eqn.3.11}{=} -\sum_j^N \frac{1}{2}\nabla_j^2 - \sum_j^N \sum_a^M \frac{Z_a}{|\mathbf{r}_j - \mathbf{R}_a|} + \frac{1}{2}\sum_{j \neq k}^N \sum_k^N \frac{1}{|\mathbf{r}_j - \mathbf{r}_k|} \tag{3.23}$$

Lets assume we have managed to solve many-body problem and obtained the wavefunction. The expectation value of the nuclei-electron interaction operator is given by

$$\langle \Psi(\mathbf{r}_1, \ldots, \mathbf{r}_N) | \hat{V}_{ne} | \psi(\mathbf{r}_1, \ldots, \mathbf{r}_N) \rangle = -\sum_{j}^{N} \sum_{a}^{M} \Psi^*(\mathbf{r}_1, \ldots, \mathbf{r}_N) \frac{Z_a}{|\mathbf{r}_j - \mathbf{R}_a|} \Psi(\mathbf{r}_1, \ldots, \mathbf{r}_N)$$

$$E_{ne} = -\sum_{a}^{M=Nn} \int n(\mathbf{r}) \frac{Z_a}{|\mathbf{r} - \mathbf{R}_a|} d\mathbf{r}$$

$$= \int n(\mathbf{r}) V_{ne}(\mathbf{r}) d\mathbf{r}$$

$$(3.24)$$

The equivalent derivation for electron-electron term is not trivial. This is because the electron-electron terms require two-particle density instead of single-particle density.

$$E_{ee} = \frac{1}{2} \int \int d\mathbf{r} d\mathbf{r}' \frac{n^{(2)}(\mathbf{r}, \mathbf{r}')}{|\mathbf{r} - \mathbf{r}'|} \tag{3.25}$$

where $n^{(2)}$ can be interpreted as the probability of finding an electron at location $\mathbf{r}$ given that a second electron exists at location $\mathbf{r}'$. Eqn. (3.25) makes the many-particle problem so hard to solve. It is required to know the conditional probability $n^{(2)}$ to solve the above equation exactly. However, to make approximation single-particle density is preferred. If the two electrons were complete uncorrelated then two-particle density can be written as the product of one-particle density.

$$n^{(2)} = n(\mathbf{r})n(\mathbf{r}') + \Delta n^{(2)}(\mathbf{r}, \mathbf{r}') \tag{3.26}$$

Where $n^{(2)}$ is a correction term. The electron-electron energy can be written as

$$E_{ee} = \frac{1}{2} \int \int d\mathbf{r} d\mathbf{r}' \frac{n(\mathbf{r})n(\mathbf{r})'}{|\mathbf{r} - \mathbf{r}'|} + \Delta E_{ee} \tag{3.27}$$

where the ΔE_{ee} term comes from the correction term in Eqn. (3.26). The kinetic energy operator has a derivative term, which creates a problem to calculate the expectation value. This is because of the derivative, it is not possible to collect wavefunction and its conjugate as a single norm square.

$$T = -\frac{1}{2} \int d\mathbf{r} \Psi^*(\mathbf{r}_1, \dots, \mathbf{r}_N) \nabla^2 \Psi(\mathbf{r}_1, \dots, \mathbf{r}_N) \tag{3.28}$$

In order to calculate kinetic energy the key assumptions of DFT is to expand the density as the sum of squares of single-particle orbitals

$$n(\mathbf{r}) = \sum_j^{N_e} |\phi_j(\mathbf{r})|^2 \tag{3.29}$$

These orbitals are called *Kohn-Sham* orbitals. Now the kinetic energy term can be written as single-particle kinetic energy plus a correction

$$T = -\frac{1}{2} \sum_j^{N_e} \int d\mathbf{r} \phi_j^*(\mathbf{r}) \nabla^2 \phi_j(\mathbf{r}) + \Delta T \tag{3.30}$$

The total ground state energy can be written as

$$
\begin{aligned}
E &= -\frac{1}{2} \sum_j^{N_e} \int d\mathbf{r} \phi_j^*(\mathbf{r}) \nabla^2 \phi_j(\mathbf{r}) + \int n(\mathbf{r}) V_{ne}(\mathbf{r}) d\mathbf{r} + \frac{1}{2} \int \int d\mathbf{r} d\mathbf{r}' \frac{n(\mathbf{r})n(\mathbf{r})'}{|\mathbf{r}-\mathbf{r}'|} + \Delta E_{ee} + \Delta T \\
&= -\frac{1}{2} \sum_j^{N_e} \int d\mathbf{r} \phi_j^*(\mathbf{r}) \nabla^2 \phi_j(\mathbf{r}) + \int n(\mathbf{r}) V_{ne}(\mathbf{r}) d\mathbf{r} + \frac{1}{2} \int \int d\mathbf{r} d\mathbf{r}' \frac{n(\mathbf{r})n(\mathbf{r})'}{|\mathbf{r}-\mathbf{r}'|} + E_{xc}
\end{aligned}
\tag{3.31}
$$

Here the two correction terms are replaced with E_{xc}, called the *exchange-corrlelation* energy. The origin of this term is the difference between N interacting and noninteracting particles. Several well-developed approximations exist for exchange-correlation, and one

of them is called local approximation

$$E_{xc} = \int d\mathbf{r} n(\mathbf{r}) \epsilon_{xc}([n], \mathbf{r}) \tag{3.32}$$

where ϵ_{xc} is an energy per electron at point $\mathbf{r}$ that depends only on the density $n(\mathbf{r})$. Thus, within the local density approximation the total energy can be written as

$$\begin{aligned}
E = &-\frac{1}{2} \sum_j^{N_e} \int d\mathbf{r} \phi_j^*(\mathbf{r}) \nabla^2 \phi_j(\mathbf{r}) + \int n(\mathbf{r}) V_{ne}(\mathbf{r}) d\mathbf{r} \\
&+ \frac{1}{2} \int \int d\mathbf{r} d\mathbf{r}' \frac{n(\mathbf{r}) n(\mathbf{r})'}{|\mathbf{r} - \mathbf{r}'|} + \int d\mathbf{r} n(\mathbf{r}) \epsilon_{xc}([n], \mathbf{r})
\end{aligned} \tag{3.33}$$

The above equation is used to derive to obtain Kohn-Sham equation which makes DFT applicable in practice. The functional form of the above equation can be written as follows:

$$E_{KS}[n] = T_s[n] + \int d\mathbf{r} V_{ext} n(\mathbf{r}) + E_H[n] + E_{xc}[n] \tag{3.34}$$

Here V_{ext} is the external potential due to the nuclei and other external field.

3.4.3 Kohn-Sham Equations

The previous section addressed the formation of K-S equation and the idea of self-consistency. In DFT based calculation, methods are classified based on the representation of the density, potential and especially KS orbitals. The choice of representation is made to increase the computational efficiency, while maintaining the accuracy. For a choice of basis, the coefficients are the only variable to be determined (density depends on KS orbitals). The total energy of DFT becomes variational, then the solution of the self-consistent KS equations requires to determine occupied orbitals that provides a minima of the total energy.

According to the second theorem of Hohenberg and Kohn, all properties such as kinetic energy, etc. are uniquely determined if $n(\mathbf{r})$ is specified. Eqn (3.33) shows the relationship. To minimize the total energy with respect of KS orbitals, the variational principle is usually

used. While performing the minimization, it is prefer to minimize with $\phi^*(\mathbf{r})$ (both yield the same result). Using the chain rule for functional derivatives, the equations becomes:

$$\frac{\delta E}{\delta \phi_i^*(\mathbf{r})} = \frac{\delta T_s}{\delta \phi_i^*(\mathbf{r})} + \left[\frac{\delta E_{\text{ext}}}{\delta n(\mathbf{r})} + \frac{\delta E_H}{\delta n(\mathbf{r})} + \frac{E_{xc}}{\delta n(\mathbf{r})} \right] \frac{\delta n(\mathbf{r})}{\delta \phi_i^*(\mathbf{r})} = 0 \qquad (3.35)$$

The kinetic energy may be differentiated separately with respect to orbital. In the above equation the E_{ei} is replaced with E_{ext} which means potential due to nuclei and any other external fields.

$$-\frac{1}{2}\nabla^2 \phi_i^*(\mathbf{r}) + \left[V_{\text{ext}}(\mathbf{r}) + \int d(\mathbf{r}') \frac{n(\mathbf{r}')}{|\mathbf{r} - \mathbf{r}'|} + \epsilon_{xc}(n) + n(\mathbf{r}) \frac{\delta \epsilon_{xc}[n]}{\delta n(\mathbf{r})} \right] \phi_i(\mathbf{r}) = \epsilon_i \phi_i(\mathbf{r}) \qquad (3.36)$$

Eqn 3.36 is a system of equations, represent the many-particle system in terms of single-particle orbitals. Each of these equations resemble a Schrödinger equation.

$$\left[\hat{T} + V_{eff} \right] \phi_i(\mathbf{r}) = \epsilon_i \phi_i(\mathbf{r}) \qquad (3.37)$$

Here the V_{eff} is the sum of the V_H, V_{xc} and V_{ext}, which depends on the density and indirectly depends on orbitals. Now we have an equation where any change in the orbitals effect also the potential on which they in turn depend on orbital. This problem is resolved by solving Kohn-Sham system of equations self-consistently.

3.5   Kohn-Sham problem for an isolated atom

For an one-electron atom, the Coulombic potential, $V(\mathbf{r}) = V(r) = -Z/r$ is spherically symmetric, the solution can be split into a radial and an angular part

$$\psi_{n\ell m}(\mathbf{r}) = \psi_{n\ell}(r)Y_{\ell m}(\theta, \phi) = r^{-1}\phi_{n\ell}(r)Y_{\ell m}(\theta, \phi) \qquad (3.38)$$

Initial guess

$n(\mathbf{r})$

Calculate effective potential

$$V_{eff}(\mathbf{r}) = V_{\text{ext}}(\mathbf{r}) + V_H[n] + V_{xc}[n]$$

Solve KS equations

$$\left[-\tfrac{1}{2}\nabla^2 + V_{eff}(\mathbf{r})\right]\phi_i(\mathbf{r}) = \epsilon_i\phi_i(\mathbf{r})$$

Calculate electron density

$$n(\mathbf{r}) = \sum_\alpha c_{i\alpha}\left|\phi_i(\mathbf{r})^2\right|$$

Self-consistent ?

no

yes

Output Quantities

Energy, forces, stresses, eigenvalues...
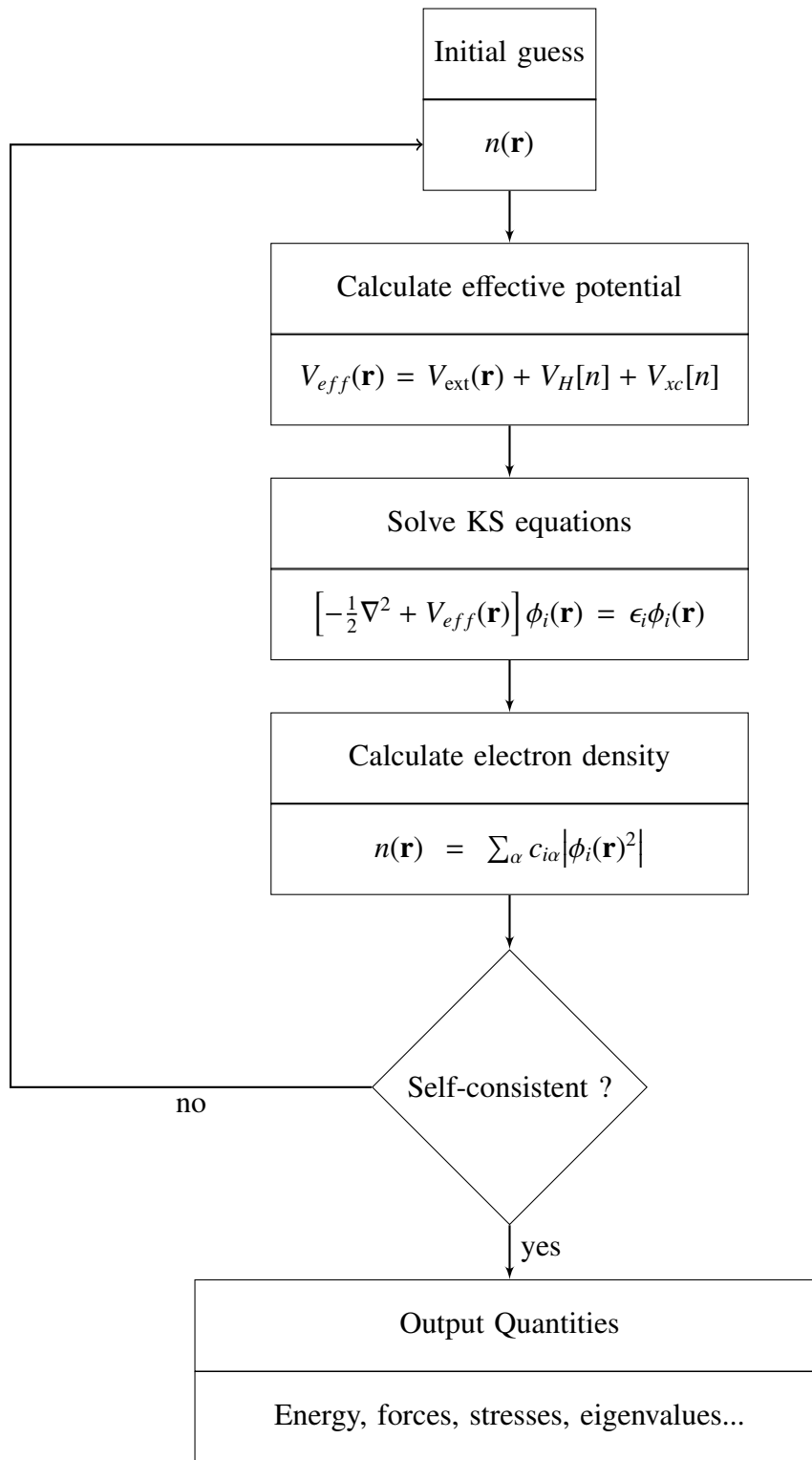
Figure 3.1. Schematic representation of the self-consistent loop solution of Kohn-Sham equations.

The above equation sometime is referred to as spherically symmetric Schrödinger equation and $Y_{\ell m}(\theta, \phi)$ are normalized spherical harmonics. Using the Laplacian in the spherical coordinates the wave equation can be reduced to the radial equation for principle quantum number n

$$-\frac{1}{2}\frac{d^2}{dr^2}\psi_{n\ell} + \left[\frac{\ell(\ell+1)}{2r^2} + V_{ext}(r) - \epsilon_{n\ell}\right]\psi_{n\ell} = 0 \qquad (3.39)$$

In the Kohn-Sham approach to the many-particle system, the form of the single-particle equations are identical to the above radial Schrödinger equation with an effective potential V_{eff} replacing the Coulomb potential. The effective potential ($V_{eff} = V_{ext}(r) + V_H(r) + V_{xc}(r)$) is spherically symmetric in the Kohn-Sham approach. The independent-particle Kohn-Sham states may be classified by the angular quantum numbers L = {ℓ, m}, and the one particle equations becomes analogous to the Schrödinger equation for one-electron atom.

$$-\frac{1}{2}\frac{d^2}{dr^2}\psi_{n\ell} + \left[\frac{\ell(\ell+1)}{2r^2} + V_{eff}(r) - \epsilon_{n\ell}\right]\psi_{n\ell} = 0 \qquad (3.40)$$

3.6 Theory of Pseudopotential

In Solids, the electrons and nuclei interact strongly through the Coulomb potential. However, according to the Fermi Liquid theory (FLT) the electronic excitation near the Fermi energy in metals behave as if they were independent particles. This leaves the strong interactions with the core electrons and the nuclei. In most cases, the core electrons are quite strongly bound, and do not respond effectively to the motions of the valence electrons. Hence, they can be regarded as essentially fixed. This is the essence of the pseudopotential approximation, the strong core potential is replaced by a pseudopotential, whose ground state wave function resembles the all electron wavefunction outside a selected core radius. In this way both the core states and the wiggles (Fig. 3.2) in the valance wavefunctions are removed. For many metals the pseudowavefunctions can be represented by lower number of planewaves. Thus making planewaves a simple and reasonable efficient basis for the pseudo wavefunctions.
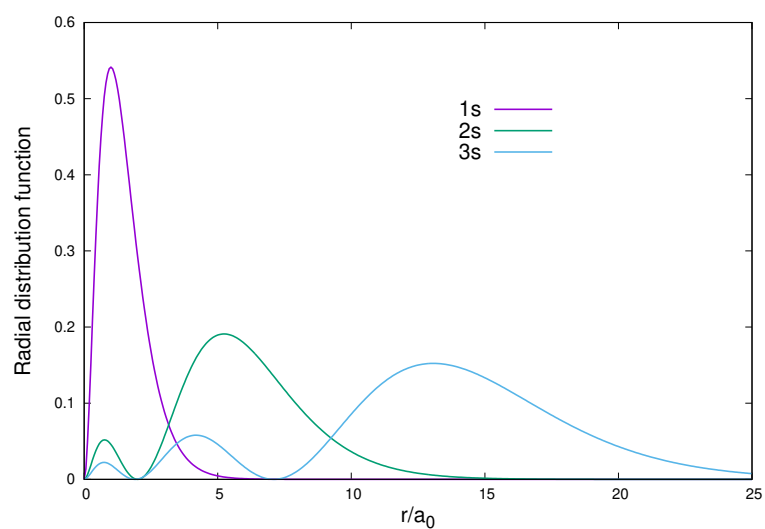
Figure 3.2. Radial distribution function of Hydrogenic 1s, 2s and 3s electron. It shows higher kinetic energy near the nucleus.
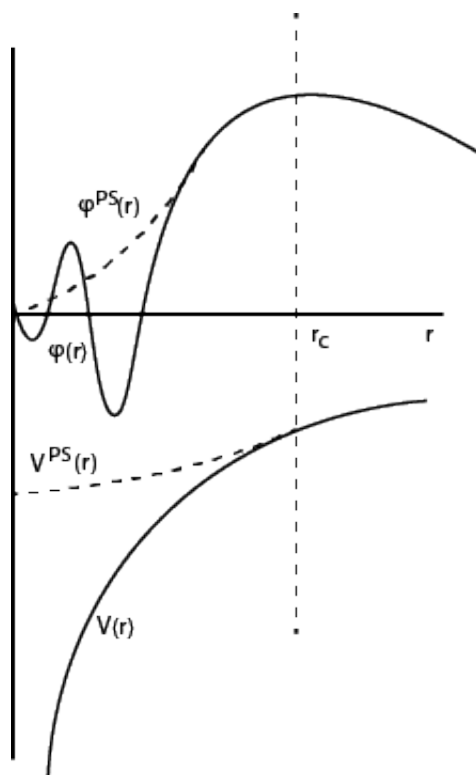
Figure 3.3. Schematic diagram of the replacement of all-electron wave function and core potential by a pseudo-wavefunction and pseudopotential.

3.6.1 Basic Phillips-Kleinman Construction

For a given many electron Hamiltonian, $\hat{H} = \hat{T} + \hat{U}$, where $\hat{T}$ is the kinetic energy operator and $\hat{U}$ is the potential energy operator, the core electron wave functions are defined by the Schrödinger equation

$$\hat{H} \, |\psi_i\rangle = \epsilon_i \, |\psi_i\rangle \quad (i = 1, ncore) \tag{3.41}$$

The valance electron wave function similarly can be found by the Hamiltonian

$$\hat{H} \, |\psi_v\rangle = \epsilon_v \, |\psi_v\rangle \tag{3.42}$$

The valence electron wave function is orthogonal to the core electron wave function ($\langle \psi_v | \psi_i \rangle = 0$), this orthogonality always has to be preserved, even if the core electrons are not treated explicitly. One way to preserve this orthogonality is to write valence electron wave function in a basis set that is priori orthogonal to the core electrons. The simple Gram-Shmidt orthogonalization technique can be used. Herring [30] was the first one to use Orthogonalized plane waves (OPWs)(Appendix C) as basis for the first quantitative calculations of bands. Using this idea, we can orthogonalize any arbitrary basis set $\{|\chi_n\rangle\}$ to the core electron wave functions by defining a new basis set $\{|\varrho_n\rangle\}$

$$|\varrho_n\rangle = |\chi_n\rangle - \sum_{i=1}^{ncore} \langle \psi_i | \chi_n \rangle \, |\psi_i\rangle \tag{3.43}$$

Here each of the new basis set, $\{|\varrho_n\rangle\}$, satisfies $\langle \chi_n | \psi_i \rangle = 0$ for each $|\psi_i\rangle$. Now we can express the valance electron wave function as a linear combination of the new basis sets,

$$|\psi_v\rangle = \sum_n C_n \, |\varrho_n\rangle \tag{3.44}$$

Using Eqn 3.43 into the Eqn 3.44, the valence electron can be expressed in the following way. The orthogonality condition with the core electron still valid.

$$|\psi_v\rangle = \sum_n C_n \left[|\chi_n\rangle - \sum_{i=1}^{ncore} |\psi_i\rangle \langle \psi_i | \chi_n\rangle \right] = |\phi\rangle - \hat{\Omega} |\phi\rangle \tag{3.45}$$

Here, $\hat{\Omega}$ is a projection operator for core electron wave function

$$\hat{\Omega} = \sum_{i=n}^{ncore} |\psi_i\rangle\langle\psi_i| \tag{3.46}$$

and a new wave function which is a linear combination of $|\chi_n\rangle$, sometime designated as pseudo-orbital,

$$|\phi\rangle = \sum_n C_n |\chi_n\rangle \tag{3.47}$$

This technique of representing the valance electron wave function in preorthogonalized basis set has been studied and used as a computational tool [30]. It took the insight of the Phillips and Kleinman [31]. The new pseudoorbitals satisfies the orthogonality condition, but it also change the Hamiltonian so that the eigen values are same with the valance electrons. Mathematically, it can be obtained by replacing original valance electron Hamiltonian equation (Eqn 3.42) with newly obtained pseudo wave function.

$$\hat{H} |\psi_v\rangle = \hat{H} \left[|\phi\rangle - \sum_n |\psi_i\rangle \langle \psi_i | \phi\rangle \right] = \epsilon_v \left[|\phi\rangle - \sum_n |\psi_i\rangle \langle \psi_i | \phi\rangle \right] \tag{3.48}$$

Rearranging the above equation provides a new Hamiltonian,

$$\left[\hat{H} + \sum_n^{ncore} (\epsilon_v - \epsilon_i) |\psi_i\rangle \langle \psi_i| \right] |\phi\rangle = \epsilon_v |\phi\rangle \tag{3.49}$$

The above equation has the form of the original valance electron eigenequation (3.42), but with an extra term for preorthogonalization. This extra potential ($V_{nl} = \sum_n^{core} |\psi_i\rangle\langle\psi_i|$), is a nonlocal operator, and the pseudo orbital ($|\phi\rangle$) is an eigenstate of the new effective

Hamiltonian, $\hat{H} + V_{nl}$. The new Hamiltonian has an extra potential V_{nl}, which depends on the angular momentum l due to the spherical symmetry. Because of its spherical symmetry, each angular momentum l, m can be treated separately. The dependence on l means that, a pseudopotential is an non-local operator, can be written in "semilocal" (SL) form

$$\hat{V}_{SL} = \sum_{lm} |Y_{lm}\rangle V_l(r) \langle Y_{lm}| \tag{3.50}$$

Where $Y_{lm}(\theta, \phi) = P_l(cos(\theta))e^{im\theta}$. It is semi-local because it is non local on the angular variables but local in the radial variable.[2]

The sophistication and accuracy have evolved considerably since the Phillips-Kleinman construction. This development produces many methods of generating pseudopotentials. All of these methods follow these goals: (1) Pseudopotential should be as soft as possible, so that it can allow representation of pseudo-wavefunction with fewer planewaves. (2) Transferability has to be maintained (it means a generated pseudopotential with a configuration should produce other properties accurately) (3) the pseudo-charge density should produce the valance charge density as accurately as possible.

3.6.2 Norm-Conserving Pseudopotentials

Hamann, Schlüter and Chiang [32] developed the concept of norm-conservation, which was a first step to fulfill all the above requirements. As the exchange-correlation energy of the electronic system depends on the electron density, it is necessary that outside the core region the real and pseudo wavefunctions be indentical. In the outer region ($r > r_c$), both functions coincide. Threfore, the total charge density created in the core region ($r < r_c$) must be the same after pseudisation:

$$\int_0^{r_c} \psi_{AE}^*(r)\psi_{AE}(r)dr = \int_0^{r_c} \psi_{ps}^*(r)\psi_{ps}(r)dr \tag{3.51}$$

---

[2]P_l is the Legendre polynomials

Where $\psi_{ae}(r)$ is the all electron wavefunction and ψ_{ps} is the pseudo wavefunction. The logarithmic derivatives of the real and pseudo wave function and their energy derivative agree in the outer region. These types of pseudopotentials are the most transferable since they are able to reproduce the scattering properties of an ion in different chemical environments [32]. The downsize of Norm-Conserving pseudopotenttial is a higher cutoff radiuss and thus increased memory and CPU requirements. Troullier and Martins [33] developed a more effective method to generate norm-conserving pseudopotentials for practical calculations.

3.6.3   Ultrasoft Pseudopotentials

The norm conservation requirement produces a very high requirement of cutoff energy for the plane-wave basis set. Particularly the tightly bound orbitals that have a substantial fraction of their weight inside the core region of the atom. There are some important cases where it was impossible to construct a pseudopotential that allows a significant reduction of the cutoff energy. Vanderbilt [34] suggested to relax the norm conservation criteria in favor of a smoother (i.e. softer) potential. The ultrasoft pseudopotentials are difficult to construct and require extensive testing [35].

3.6.4   Projector Augmented-Wave Method (PAW)

The electronic wave functions oscillate wildly near the nuclei (Fig. 3.2) than the bonding area between the atoms. Expanding these region using plane-wave creates computational challenges. Augmented-wave methods uses the separation of the wave functions in two regions to address this issue. The first part is partial wave expansion inside an atom-centered sphere called the augmentation region and a plane wave expansion outside. Both expansions are continuously differentiable at the boundary.

Blöchl [12] suggested that there is a linear transformation from the all-electron to the pseudo wave functions. The transformation is as follows:

$$|\Psi\rangle = |\tilde{\Psi}\rangle + \sum_i (|\phi_i\rangle - |\tilde{\phi}_i\rangle) \langle \tilde{p}_i | \tilde{\Psi}\rangle \qquad (3.52)$$

Here ϕ_i are the partial waves within the augmentation regions, and $\langle \tilde{p}_i |$ is a projector with a condition of $\langle \tilde{p}_i | \tilde{\phi}_i \rangle = \delta_{ij}$. The tilde quantities are related the pseudo representation. Kresse and Joubert [35] showed a connection between PAW and US-pp and how the PAW method can be implemented into existing code.

3.7   Computational Details

We perform all calculations using density functional theory (DFT) with plane-wave basis sets as implemented in the software QUANTUMESPRESSO [28]. We generated a uranium pseudopotential for use with the Perdew–Burke–Ernzerhof (PBE) exchange–correlation functional [17, 18]. The projector augmented wave (PAW) pseudopotential-generating software atompaw [36, 37] was used to generate the PAW pseudopotential for uranium. The same pseudopotential was used for all subsequent calculations.

One of the major challenges in studying actinides using DFT is how to treat the large number of electrons. The pseudopotential approach effectively reduces the number of electrons by modeling the "core" as a potential energy surface, so generating a pseudopotential requires one to choose the number of electrons that will be treated explicitly. There are two approaches common for uranium: "small-core" pseudopotentials and "large-core" pseudopotentials. In a large-core pseudopotential, the valence electrons are the $5f$, $6s$, $6p$, $6d$ and $7s$ shells (14 electrons). In small-core pseudopotentials, the $5s$, $5p$, and $5d$ shells are also included, which treats 32 electrons as valence electrons. Iche-Tarrat and Marsden [38] have discussed this topic and shown that the explicit treatment of 32 electrons only marginally improves the performance of DFT at significantly higher computational

cost. The valence electron configuration of uranium used when generating our pseudopotential was $6s^2 6p^6 7s^2 6d^1 5f^3$ (*i.e.*, it is a large-core pseudopotential). The radius of the augmentation region was chosen to be 2.5 bohr, which we determined by starting from half the experimental nearest-neighbor interatomic distance in α-uranium and adjusting based on energy–volume minimization. The pseudo-partial waves were generated using the RRKJ scheme [39], which uses a sum of Bessel functions to represent the pseudo-partial waves. A plane-wave cutoff energy analysis was performed and a 50 Ry energy cutoff was found to be sufficient based on a plot of total energy against cutoff energy. All calculations were performed on primitive cells using the cell geometries and coordinates given by Crocombette *et al.* [7] for α-uranium, Beeler *et al.* [20] for bct uranium, and values from the Structure of Crystals database [40] for all other structures. Periodic boundaries were applied in all directions. The Monkhorst–Pack scheme [41] was used for Brillouin zone sampling; the *k*-point meshes were $20 \times 20 \times 26$, $20 \times 20 \times 20$, $18 \times 18 \times 18$, and $20 \times 20 \times 20$ for the α, bct, γ, and fcc lattices, respectively. A Methfessel–Paxton [42] smearing method (width 0.02 Ry) was used to integrate the bands at the Fermi level. To calculate the nine unique elastic moduli of orthorhombic α-U, the energy–strain relationship (see appendix F) was used as described by Ravindran *et al.* [43]. For cubic structures, the elastic moduli were evaluated using volume-conserving orthorhombic and monoclinic distortions as described by Beckstein *et al.* [44].

3.8   Results

The pseudopotential itself is generated by atompaw [36, 37], which takes as input the augmentation radius (r_{PAW}), core radius (r_{core}), shape function cutoff (r_{shape}), matching radius (r_{vloc}), valence and core electron configurations, density functional, and the cutoff radii for each of the partial waves ($r_{c,i}$). We assumed $r_c = r_{PAW}$ for all valence electrons except the 6*s* and 7*s* electrons, for which r_c was adjusted. The cutoff radii are given in Table 3.1.

Table 3.1. Parameters used to generate the pseudopotential in atompaw [36, 37].

Cutoff	Value (bohr)
r_{PAW}	2.50
r_{shape}	2.02
r_{vloc}	1.50
r_{core}	1.80
$r_{c,i}$	r_{PAW}
EXCEPT	
$r_{c,6s}$	1.50
$r_{c,7s}$	1.50

These cutoffs, combined with the choice of density functional and valence electrons, are sufficient to reproduce the pseudopotential in atompaw.

Properties of several uranium phases as calculated with the pseudopotential presented above are detailed in the rest of this section.

3.8.1 α-Uranium

Uranium's α phase has a base-centered orthorhombic structure with space group *Cmcm* (no. 63). The asymmetric unit has uranium atoms at Wyckoff position $4c\left(0, \pm y, \pm\frac{1}{4}\right)$, where the position parameter *y* has been found to be a function of temperature [15]. At room temperature, the value of *y* has been measured to be 0.1024 [15, 45]. There are four atoms in the standard unit cell (two in the primitive cell). The α phase is thermodynamically favorable at temperatures below 935 K and pressures up to 100 GPa [2, 46]. This makes the α phase important to the nuclear energy community because it is the naturally-occurring phase of uranium. The solid-state physics community also shows interest in α-uranium because of certain unusual characteristics, including charge density wave transitions and superconductivity.

The total energy as a function of unit cell volume for α uranium is shown in Figure 3.4; Table 3.2 summarizes the optimized lattice parameters, the distance parameter *y*, and the calculated elastic moduli, along with results from previously published calculations and

experiments. We confirm that α-U is the lowest-energy crystal structure among those we tested. Our pseudopotential predicts an equilibrium volume of 20.49 Å^3, which is in close agreement with the experimental value of 20.530 Å^3 (at 50 K). The position parameter y exhibits a minimum-energy value of 0.0986 at the equilibrium volume of 20.49 Å^3. This trend in y is similar to that observed in the calculations of Wills and Eriksson [5].

Our cell volume results differ from previous calculations using PAW [20], which obtained an equilibrium volume of 19.987 Å^3. A Murnaghan [47] fit to the total energy as a function of volume for α-uranium yielded a bulk modulus of 132.1 GPa, which is larger than the experimental value of 104 ± 2 GPa [46], but agrees closely with the quantum molecular dynamics (QMD) results of Hood *et al.* [48] (133.5 GPa) and the diamond anvil cell (DAC) experiments of Yoo *et al.* [49], which reported a bulk modulus of 135.5 GPa. Our pseudopotential-based results are in close agreement with the all-electron FP-LMTO calculations of Söderlind [8], which gave an equilibrium volume of 20.67 Å^3 and a bulk modulus of 133.0 GPa. A published PAW-based pseudopotential from Beeler *et al.* [20] yields an equilibrium volume of 19.92 Å^3, which is lower than our result and farther from both the experimental value and the result from all-electron calculations.

The elastic moduli predicted by our pseudopotential are presented in Table 3.2. Like all materials with orthorhombic symmetry, α-U has nine unique elastic moduli. Our model overestimates most of the elastic moduli relative to experiments. The three primary-direction elastic moduli (C_{11}, C_{22}, and C_{33}) show good agreement with other theoretical results and with experiment, though all three principal elastic moduli are overestimated. The order ($C_{33} > C_{11} > C_{22}$) of these three elastic moduli is also consistent with experiments. For C_{55} and C_{13}, the present results also show good agreement with experiments. The value of C_{66} is overestimated relative to experiment, but closer than any existing prediction from a pseudopotential-based calculation. The other elastic moduli are generally similar to existing theoretical predictions.
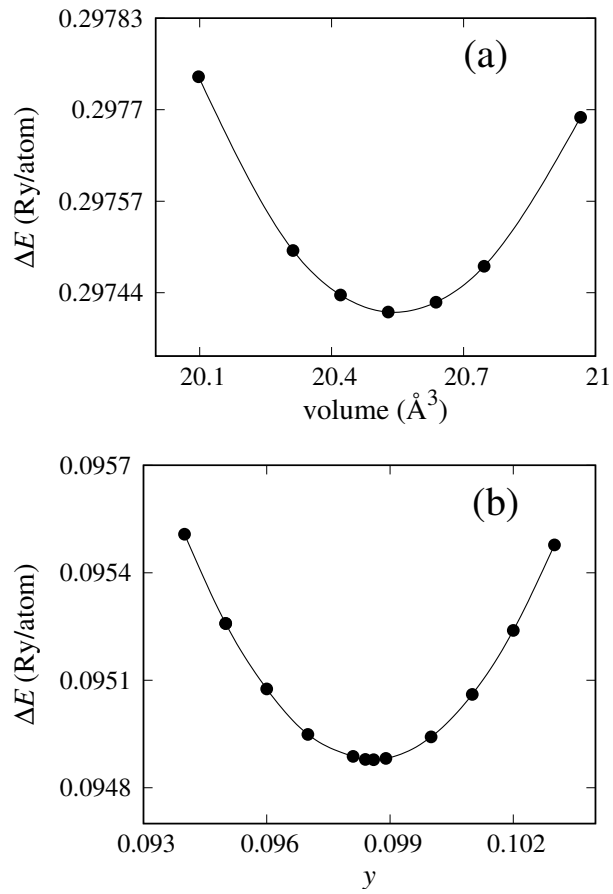
Figure 3.4. (a) Calculated total energy as a function of volume for α uranium. (b) Calculated total energy as a function of the positional parameter y for α uranium. The calculation of y is constrained to an equilibrium volume of 20.49 Å^3.

Table 3.2. Ground-state properties and elastic moduli of α-U from present work, compared with the PAW pseudopotential calculations of Beeler *et al*. [20], the full-core calculations of Söderlind [8], and experiments from Barrett [15], Le Bihan *et al*. [46], and Fisher and McSkimin [50] (295 K).

	Theory			Experiment		
	present work	Beeler [20]	Söderlind [8]	Barrett [15]	Le Bihan [46]	Fisher [50]
a (Å)	2.834	2.793	2.845	2.836	2.8553	-
b (Å)	5.862	5.849	5.818	5.867	5.8702	-
c (Å)	4.932	4.893	4.996	4.936	4.9568	-
y	0.0986	0.097	0.103	0.102	0.102	-
volume/atom (Å^3)	20.48	19.987	20.674	20.535	20.770	-
B (GPa)	132.1	151	133	-	104(2)	-
B'	5.27	-	5.4	-	6.2	-
C_{11} (GPa)	315	299	300	-	-	215
C_{22} (GPa)	213	231	220	-	-	199
C_{33} (GPa)	387	364	320	-	-	267
C_{44} (GPa)	135	100	150	-	-	124
C_{55} (GPa)	87	150	93	-	-	73
C_{66} (GPa)	104	132	120	-	-	74
C_{12} (GPa)	58	59	50	-	-	46
C_{13} (GPa)	45	30	5	-	-	22
C_{23} (GPa)	146	144	110	-	-	108

3.8.2 γ-U: Crystal Structure and Elastic Moduli

The structure of γ-uranium at high temperature was first elucidated by Wilson and Rundle [51] at Iowa State University in 1949 using powdered uranium at 800 °C. The γ phase of uranium has a body-centered cubic (bcc; Structurbericht designation A2) structure with two atoms in the standard unit cell [52, 53]. It is thermodynamically stable from 1050 K to the melting point of 1406 K [49].

In the nuclear fuels community, γ uranium is preferred to α-uranium because it undergoes isotropic thermal expansion and radiation-induced swelling [54]. As Wilson and Rundle observed [51], it is not possible to quench pure γ-uranium to room temperature, but a metastable bcc phase can be retained at room temperature in U–Mo alloys. Recently, it was found that the bcc structure can be retained by alloying uranium with other metals, such as platinum, palladium, niobium, and zirconium [55]. In particular, the eutectoid point of γ-uranium with molybdenum impurities is at approximately 89 weight-percent uranium; to

Table 3.3. The equilibrium lattice parameters and volume per atom of γ-uranium. Results are compared with the PAW pseudopotential calculations of Beeler *et al*. [20] and Taylor [11], as well as the norm-conserving pseudopotential calculations of Crocombette *et al*. [7] and the experiments of Wilson and Rundle [51] at room temperature. Elastic moduli are compared with previous PAW pseudopotential calculations from Beeler *et al*. [20] and Taylor [11].

	Theory				Experiment	
	present work	Beeler [20]	Taylor [11]	Crocombette [7]	Wilson [51]	Yoo [49]
a (Å)	3.45	3.427	3.43	3.37	3.47	-
volume/atom (Å^3)	20.56	20.124	20.18	19.14	20.89	-
C_{11} (GPa)	40	86	161	-	-	-
C_{12} (GPa)	145	155	184	-	-	-
C_{44} (GPa)	42	37	56	-	-	-
B (GPa)	110	132	176	170	-	113.3

take advantage of the depressed phase transition temperature (and the associated increase in stability of the bcc phase), uranium alloyed with 10 wt% molybdenum ($\approx$ 21.6 at.%; U-10Mo) is currently being developed as a potential high-density low-enrichment uranium (LEU) fuel for high-performance research reactors. The lattice parameters, volume per atom, and elastic moduli as calculated with our pseudopotential-based model are presented in Table 3.3.

The lattice parameters for γ-uranium as calculated with the pseudopotential presented here are in good agreement with experiments. The elastic moduli are comparable with those of Beeler *et al*. [20] and Taylor [11]. The value of C_{12} is larger than that of C_{11}, which is a violation of one of the stability criteria for cubic crystals ($C_{11} - C_{12} > 0$), often called the Born stability criteria [56–58]. This violation is expected, as the bcc phase of uranium is unstable at low temperatures. The experimental value of bulk modulus by Yoo *et al*. [49] is in good agreement with our result.

3.8.3 Body-centered Tetragonal Uranium

The β-phase of uranium is stable at atmospheric pressure between 935 and 1045 K [1]. Tucker [60] determined that it has a tetragonal structure with 30 atoms per unit cell, but his space group assignment was later disputed. The assignment of a space group remained a

Table 3.4. The optimized lattice parameters (Å), volume per atom (Å^3) and elastic moduli of bct uranium. Our calculated results are compared with those of Beeler *et al*. [20], Li *et al*. [19], Xiang *et al*. [16], and Söderlind [59].

	present work	Beeler [20]	Li [19]	Xiang [16]	Söderlind [59]
a (Å)	3.44	3.695	3.72	-	-
c/a	0.8125	0.8	1.24	-	0.82
volume/atom (Å^3)	20.44	20.268	31.896	20.5	-
C_{11} (GPa)	270	264	230	-	-
C_{33} (GPa)	257	254	204	-	-
C_{12} (GPa)	65	55	61	-	-
C_{13} (GPa)	32	68	61	-	-
C_{44} (GPa)	59	56	79	-	-
C_{55} (GPa)	71	56	39	-	-
B (GPa)	115.4	130	114	-	-

controversy until 1988, when Lawson and coworkers [1] published neutron powder diffraction results. The experimental difficulties lie in the preparation of a single crystal of β-uranium and the need to operate at high temperature. Single crystals of a β-uranium alloy containing 1.4 atom% chromium were created by Tucker [61] and quenched to room temperature, but he did not establish whether this alloy had the same crystal structure as pure β-uranium [1]. An overview of the development of the crystal structure of β-uranium is given by Donohue and Einspahr [62, 63]. The present consensus is that β-uranium has a tetragonal crystal structure with with space group $P4_2/mnm$ (no. 136) and 30 atoms in the unit cell.

We chose to simulate a body-centered tetragonal structure instead of β uranium because of the latter's complexity and computational expense. A similar simplification was used in studies similar to ours [19, 20]. The bct structure has only two atoms per unit cell, and is therefore less computationally expensive than β uranium. The equilibrium lattice parameters of bct uranium are presented in Table 3.4, alongside values from Beeler *et al*. [20] and Li *et al*. [19]. The volume per atom agrees well with Beeler *et al*. but is significantly different from that of Li *et al*. Xiang *et al*. [16] also studied the bct structure

Table 3.5. The equilibrium lattice parameter, volume per atom, and elastic moduli of fcc uranium. Results are compared with PAW pseudopotential calculations of Beeler *et al*. [20], Taylor [11], and Crocombette *et al*. [7].

	present work	Beeler [20]	Taylor [11]	Crocombette [7]
a (Å)	4.300	4.433	4.48	4.30
volume/atom (Å^3)	21.765	21.774	22.48	19.88
C_{11} (GPa)	67	46	184	-
C_{12} (GPa)	130	144	267	-
C_{44} (GPa)	38	40	28	-
B (GPa)	108.7	111	239	148

of uranium, though they did not provide the equilibrium lattice parameter or c/a ratio; their value of the equilibrium volume per atom was 20.5 Å^3, similar but larger than our value. Our c/a ratio is in good agreement with both Beeler *et al*. [20] (0.8) and Söderlind [59] (0.82).

3.8.4 Face-Centered Cubic Uranium

Face-centered cubic uranium does not exist in nature, but it is a reasonable way to check the pseudopotential. Beeler *et al*. [20] and Taylor [11] studied this structure as well, so we compare our results with theirs. Table 3.5 shows the equilibrium parameters and elastic moduli as calculated with our model and with several other published pseudopotentials. Our results are in good agreement with other pseudopotential calculations, particularly those of Beeler *et al*. [20]; the bulk modulus shows good agreement with their value as well. It should be noted that C_{12} is still higher than C_{11}, confirming that this model predicts the fcc phase to be unstable.

3.8.5 Electronic Density of States

The electronic densities of states (DOS) of α, bct, γ, and fcc uranium are shown in Figure 3.5. The partial densities of states for the $5f$ and $6d$ orbitals are shown in Figure 3.6. We have only shown the partial densities of states for the $5f$ and $6d$ orbitals because these
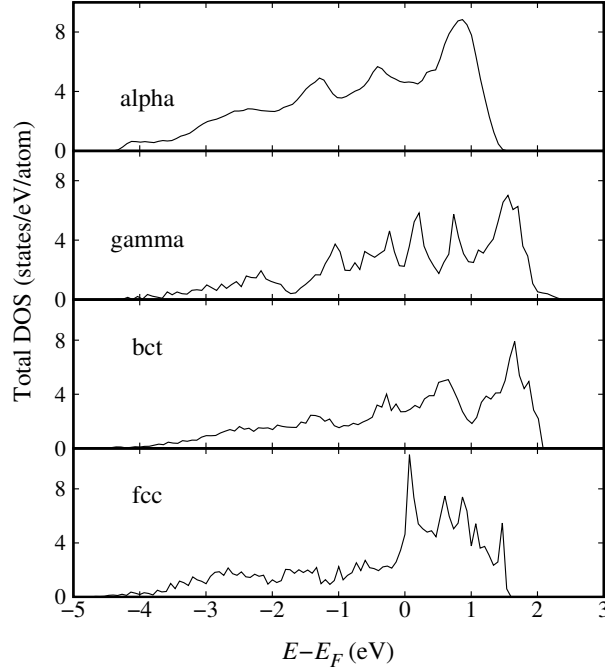
Figure 3.5. Total electronic densities of states of α, γ, bct, and fcc uranium near the Fermi level.

are the dominant orbitals near the Fermi level of uranium. There are also contributions from $6s$, $6p$, and $7s$ orbitals near the Fermi level, but these contributions are not as significant as the dominant $5f$ and $6d$ orbitals. Electrons near the Fermi level are important because they are responsible for most of the metallic behavior. From Figure 3.5, it can be seen that the DOS spreads over energies between -4 eV and 2 eV relative to the Fermi level. The density of states with our model is comparable to those calculated by Beeler *et al.* [20] and Xiang *et al.* [16]. For bcc and bct uranium, the f orbitals spread over a broader range of energies near the Fermi level and show multiple peaks above the Fermi level. The high density of states at energies above the Fermi level in the bct and γ phases suggest that these phases would be favored over α-uranium at high temperature.
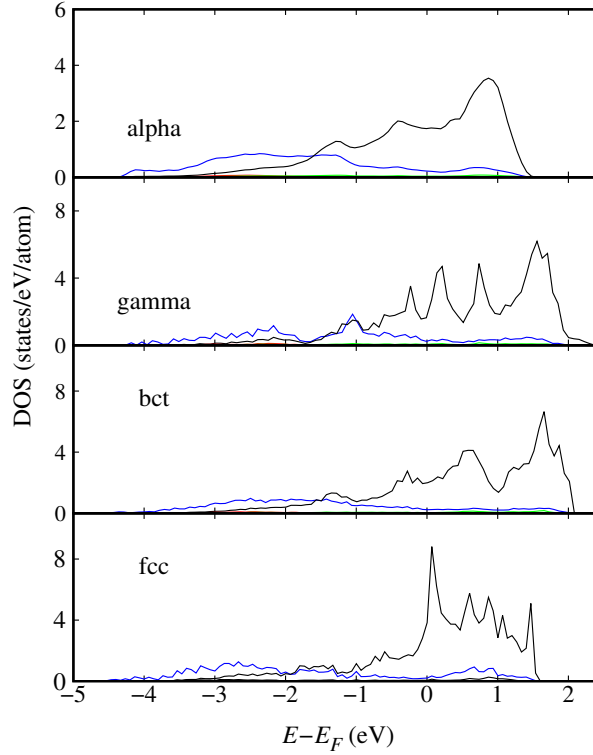
Figure 3.6. The partial electronic densities of states of α, γ, bct, and fcc uranium near the Fermi level. The $6d$ (blue line) and $5f$ (black line) electronic orbitals are shown. The s (red) and p (green) electronic orbitals are also included, but due to their very low contributions near the Fermi level, they are barely visible.

3.9   Conclusion

The equilibrium structures, cell volumes, and elastic moduli have been calculated using DFT with a newly parameterized pseudopotential model for four different uranium phases (α, γ, body-centered tetragonal, and face-centered cubic). Our results are either in good agreement with previous work or show improvement in comparison with experiments. Studying pure uranium is the first step in exploring different alloys of uranium that are of interest to the nuclear fuels community. Due to the lower cutoff energies that can typically be used, PAW-based pseudopotentials allow one to study larger supercells, which in turn provide more accurate studies of vacancy formation, grain boundaries, and fission gas transport.

According to our pseudopotential, α-uranium is the lowest-energy crystal structure of the ones tested. The calculated elastic moduli show good agreement with previous DFT studies and experiments. Our model shows good agreement with previous pseudopotentials, but generally provides results that are either comparable to previously published pseudopotentials or closer to experimental values than previously published pseudopotentials. The three elastic moduli associated with shear (C_{44}, C_{55}, and C_{66}) show better agreement with experimental results than the tensile components. The lattice parameters of the bct structure are also very similar to those predicted by Beeler *et al.* [20], but they deviate significantly from those of Li *et al.* [19]. The elastic moduli show very similar trends to previously published models, apart from C_{23}, which is over-predicted by our model.

For γ uranium, which is of great interest for the development of low-enrichment uranium fuel, the lattice parameters are in close agreement with those of of Taylor *et al.* [11] and with experiments. Apart from the elastic modulus C_{11}, the values of all computed parameters show very little discrepancy compared with those from the work of Taylor *et al.* [11] and Beeler *et al.* [20]. The bulk modulus shows very good agreement with experiment.

For fcc uranium, a hypothetical crystal structure, the computed lattice parameter is in close agreement with values reported by Beeler *et al.* [20] and by Crocombette *et al.* [7]. The equilibrium volume per atom does show a discrepancy from Crocombette but is in good agreement with Beeler *et al.* The elastic modulus C_{44} is also in good agreement with Beeler *et al.*, whereas C_{11} is intermediate between the value predicted by Beeler *et al.* and that predicted by Taylor *et al.* Lastly, the electronic density of states shows that the $5f$ orbital partial density of states is the largest contribution to the total density of states at the Fermi energy, and the $5f$ electrons therefore contribute the most to the bonding and conductivity of uranium. Most of the $5f$ orbital electron density is spread over energies between -4 and 2 eV relative to the Fermi level. We also find that γ-uranium has the highest

density of states at values above the Fermi level, confirming that it should be favored at high temperature.

References

1. A. C. Lawson, C. E. Olsen, J. W. Richardson, M. H. Mueller, and G. H. Lander. Structure of β-uranium. *Acta Crystallogr. B*, 44(2):89–96, 1988.

2. J. Akella, S. Weir, J. M. Wills, and P. Söderlind. Structural stability in uranium. *J. Phys. Condens. Matter*, 9(39):L549–L555, 1997.

3. G. H. Lander. G h lander. *Science*, 301:1057, 2003.

4. Arthur J. Freeman and G. H. Lander. *Handbook on the Physics and Chemistry of the Actinides*, volume 1,2. North-Holland, Amsterdam, 1984.

5. J. M. Wills and Olle Eriksson. Crystal-structure stabilities and electronic structure for the light actinides Th, Pa, and U. *Phys. Rev. B*, 45(24):13879, 1992.

6. Olle Eriksson, Per Söderlind, J. M. Wills, and A. M. Boring. First principles studies of crystal structures of f elements. *Phys. C Supercond.*, 190(1):5–11, 1993.

7. J. P. Crocombette, F. Jollet, L. Thien Nga, and T. Petit. Plane-wave pseudopotential study of point defects in uranium dioxide. *Phys. Rev. B*, 64(10):104107, 2001.

8. Per Söderlind. First-principles elastic and structural properties of uranium metal. *Phys. Rev. B*, 66(8):085113, 2002.

9. A. C. Lawson, B. M. Artinez, J. A. Roberts, B. I. Bennett, and J. W. Richardson, Jr. Melting of the light actinides. *Philos. Mag. B*, 80(1):53–59, 2000.

10. M. D. Jones, J. C. Boettger, R. C. Albers, and D. J. Singh. Theoretical atomic volumes of the light actinides. *Phys. Rev. B*, 61(7):4644, 2000.

11. Christopher D. Taylor. Evaluation of first-principles techniques for obtaining materials parameters of α-uranium and the (0 0 1) α-uranium surface. *Phys. Rev. B*, 77(9):094119, 2008.

12. P. E. Blöchl. Projector augmented-wave method. *Phys. Rev. B*, 50(24):17953–17979, December 1994.

13. J. P. Perdew, J. A. Chevary, S. H. Vosko, K. A. Jackson, M. R. Pederson, D. J. Singh, and C. Fiolhais. Atoms, molecules, solids, and surfaces: Applications of the generalized gradient approximation for exchange and correlation. *Phys. Rev. B*, 46(11):6671–6687, September 1992.

14. J. P. Perdew, J. A. Chevary, S. H. Vosko, K. A. Jackson, M. R. Pederson, D. J. Singh, and C. Fiolhais. Erratum: Atoms, molecules, solids, and surfaces: Applications of the generalized gradient approximation for exchange and correlation. *Phys. Rev. B*, 48(7):4978, 1993.

15. C. S. Barrett, M. H. Mueller, and R. L. Hitterman. Crystal structure variations in alpha uranium at low temperatures. *Phys. Rev.*, 129(2):625, 1963.

16. Shikai Xiang, Hanchen Huang, and L. M. Hsiung. Quantum mechanical calculations of uranium phases and niobium defects in γ-uranium. *J. Nucl. Mater.*, 375(1):113–119, 2008.

17. John P. Perdew, Kieron Burke, and Matthias Ernzerhof. Generalized gradient approximation made simple. *Phys. Rev. Lett.*, 77(18):3865–3868, October 1996.

18. John P. Perdew, Kieron Burke, and Matthias Ernzerhof. Generalized gradient approximation made simple (errata). *Phys. Rev. Lett.*, 78(7):1396, 1997.

19. J. H. Li, Q. B. Ren, C. H. Lu, L. Lu, Y. Dai, and B. X. Liu. Structure, formation energies and elastic constants of uranium metal investigated by first principles calculations. *J. Alloy Compd.*, 516:139–143, 2012.

20. Benjamin Beeler, Chaitanya Deo, Michael Baskes, and Maria Okuniewski. First principles calculations of the structure and elastic constants of α, β and γ uranium. *J. Nucl. Mater.*, 433(1-3):143–151, 2013.

21. Douglas R Hartree. The wave mechanics of an atom with a non-coulomb central field. part i. theory and methods. *Mat. Proc. Cambridge Philos. Soc.*, 24:89, 1928.

22. Vladimir Fock. Näherungsmethode zur lösung des quantenmechanischen mehrkörperproblems. *Zeitschrift für Physik*, 61(1-2):126–148, 1930.

23. Pierre Hohenberg and Walter Kohn. Inhomogeneous electron gas. *Phys. Rev.*, 136(3B):B864, 1964.

24. Llewellyn H. Thomas. The calculation of atomic fields. In *Mathematical Proceedings of the Cambridge Philosophical Society*, volume 23, pages 542–548. Cambridge University Press, 1927.

25. Enrico Fermi. Un metodo statistico per la determinazione di alcune priorieta dell'atome. *Rend. Accad. Naz. Lincei*, 6(602-607):32, 1927.

26. David C. Langreth and John P. Perdew. The exchange-correlation energy of a metallic surface. *Solid State Commun.*, 17(11):1425–1429, 1975.

27. Walter Kohn and Lu Jeu Sham. Self-consistent equations including exchange and correlation effects. *Phys. Rev.*, 140(4A):A1133, 1965.

28. Paolo Giannozzi, Stefano Baroni, Nicola Bonini, Matteo Calandra, Roberto Car, Carlo Cavazzoni, Davide Ceresoli, Guido L. Chiarotti, Matteo Cococcioni, Ismaila Dabo, Andrea Dal Corso, Stefano de Gironcoli, Stefano Fabris, Guido Fratesi, Ralph Gebauer, Uwe Gerstmann, Christos Gougoussis, Anton Kokalj, Michele Lazzeri, Layla Martin-Samos, Nicola Marzari, Francesco Mauri, Riccardo Mazzarello, Stefano Paolini, Alfredo Pasquarello, Lorenzo Paulatto, Carlo Sbraccia, Sandro Scandolo, Gabriele Sclauzero, Ari P. Seitsonen, Alexander Smogunov, Paolo Umari, and Renata M. Wentzcovitch. QUANTUM ESPRESSO: A modular and open-source software project for quantum simulations of materials. *J. Phys. Condens. Matter*, 21(39):395502, September 2009.

29. Xavier Gonze, J-M Beuken, R. Caracas, F. Detraux, M. Fuchs, G-M Rignanese, Luc Sindic, Matthieu Verstraete, G. Zerah, F. Jollet, et al. First-principles computation of material properties: the abinit software project. *Comput. Mater. Sci.*, 25(3):478–492, 2002.

30. Conyers Herring. A new method for calculating wave functions in crystals. *Phys. Rev.*, 57(12):1169, 1940.

31. James C Phillips and Leonard Kleinman. New method for calculating wave functions in crystals and molecules. *Phys. Rev.*, 116(2):287, 1959.

32. D. R. Hamann, M. Schlüter, and C. Chiang. Norm-conserving pseudopotentials. *Phys. Rev. Lett.*, 43(20):1494, 1979.

33. Norman Troullier and José Luís Martins. Efficient pseudopotentials for plane-wave calculations. *Phys. Rev. B*, 43(3):1993, 1991.

34. David Vanderbilt. Soft self-consistent pseudopotentials in a generalized eigenvalue formalism. *Phys. Rev. B*, 41(11):7892, 1990.

35. Georg Kresse and D. Joubert. From ultrasoft pseudopotentials to the projector augmented-wave method. *Phys. Rev. B*, 59(3):1758, 1999.

36. N. A. W. Holzwarth, A. R. Tackett, and G. E. Matthews. A projector augmented wave (PAW) code for electronic structure calculations, part I: atompaw for generating atom-centered functions. *Comput. Phys. Commun.*, 135(3):329–347, 2001.

37. A. R. Tackett, N. A. W. Holzwarth, and G. E. Matthews. A projector augmented wave (PAW) code for electronic structure calculations, part II: pwpaw for periodic solids in a plane wave basis. *Comput. Phys. Commun.*, 135(3):348–376, 2001.

38. Nathalie Iché-Tarrat and Colin J. Marsden. Examining the performance of dft methods in uranium chemistry: Does core size matter for a pseudopotential? *The Journal of Physical Chemistry A*, 112(33):7632–7642, 2008.

39. Andrew M. Rappe, Karin M. Rabe, Efthimios Kaxiras, and J. D. Joannopoulos. Optimized pseudopotentials. *Phys. Rev. B*, 41(2):1227, 1990.

40. Naval Research Laboratories. Structure of Crystals. `http://aflowlib.duke.edu/users/egossett/lattice/`, 2015.

41. James D. Pack and Hendrik J. Monkhorst. "special points for Brillouin-zone integrations"—a reply. *Phys. Rev. B*, 16(4):1748–1749, 1977.

42. M. Methfessel and A. T. Paxton. High-precision sampling for Brillouin-zone integration in metals. *Phys. Rev. B*, 40(6):3616–3621, 1989.

43. P. Ravindran, Lars Fast, P. A. Korzhavyi, B. Johansson, J. Wills, and O. Eriksson. Density functional theory for calculation of elastic properties of orthorhombic crystals: Application to TiSi$_2$. *J. Appl. Phys.*, 84(9):4891–4904, 1998.

44. O. Beckstein, J. E. Klepeis, G. L. W. Hart, and O. Pankratov. First-principles elastic constants and electronic structure of α-pt$_2$ si and PtSi. *Phys. Rev. B*, 63(13):134112, 2001.

45. G. H. Lander, E. S. Fisher, and S. D. Bader. The solid-state properties of uranium: A historical perspective and review. *Adv. Phys.*, 43(1):1–111, 1994.

46. T. Le Bihan, S. Heathman, M. Idiri, G. H. Lander, J. M. Wills, A. C. Lawson, and Andreas Lindbaum. Structural behavior of α-uranium with pressures to 100 GPa. *Phys. Rev. B*, 67(13):134102, 2003.

47. F. D. Murnaghan. The compressibility of media under extreme pressures. *Proc. Natl. Acad. Sci. U. S. A.*, 30(9):244–247, 1944.

48. Randolph Q. Hood, L. H. Yang, and John A. Moriarty. Quantum molecular dynamics simulations of uranium at high pressure and temperature. *Phys. Rev. B*, 78(2):024116, 2008.

49. Choong-Shik Yoo, Hyunchae Cynn, and Per Söderlind. Phase diagram of uranium at high pressures and temperatures. *Phys. Rev. B*, 57(17):10359, 1998.

50. E. S. Fisher and H. J. McSkimin. Adiabatic elastic moduli of single crystal alpha-uranium. *J. Appl. Phys.*, 29(10):1473–1484, 1958.

51. A. S. Wilson and R. E. Rundle. The structures of uranium metal. *Acta Crystallogr.*, 2(2):126–127, 1949.

52. Harry L. Yakel. Review of x-ray diffraction studies in uranium alloys. Technical report, Oak Ridge National Laboratory, Tennessee (USA), 1973.

53. I. Grenthe, J. Drozdzynski, T. Fujino, E. C. Buck, T. E. Albrecht-Schmitt, and S. F. Wolf. *The Chemistry of the Actinide and Transactinide Elements*, volume 1. Springer, Dordrecht, 2006.

54. J. H. Kittel, B. R. T. Frost, J. P. Mustelier, K. Q. Bagley, G. C. Crittenden, and J. Van Dievoet. History of fast reactor fuel development. *J. Nucl. Mater.*, 204:1–13, 1993.

55. N.-T. H Kim-Ngan and L. Havela. Superconductivity in U-T alloys (T = Mo, Pt, Pd, Nb, Zr) stabilized in the cubic γ-u structure by splat-cooling technique. *J. Sci. Adv. Mater. Dev.*, 1(2):121–127, 2016.

56. Max Born. On the stability of crystal lattices. I. *Proc. Camb. Phil. Soc.*, 36(2):160–172, 1940.

57. Max Born and Kun Huang. *Dynamical Theory of Crystal Lattices*. Clarendon Press, 1954.

58. Félix Mouhat and François-Xavier Coudert. Necessary and sufficient elastic stability conditions in various crystal systems. *Phys. Rev. B*, 90:224104, 2014.

59. Per Söderlind. Theory of the crystal structures of cerium and the light actinides. *Adv. Phys.*, 47(6):959–998, 1998.

60. C. W. Tucker, Jr. An approximate crystal structure for the beta phase of uranium. Technical Report KAPL-388, Knolls Atomic Power Laboratory, 1950.

61. C. W. Tucker. The crystal structure of the β phase of uranium. *Acta Crystallogr.*, 4(5):425–431, 1951.

62. Jerry Donohue and Howard Einspahr. The structure of β-uranium. *Acta Crystallogr. B*, 27(9):1740–1743, 1971.

63. Jerry Donohue. *Structures of the Elements*. John Wiley and Sons, 1974.

CHAPTER 4

XENON MOBILITY IN BCC-URANIUM AND
URANIUM–MOLYBDNEUM ALLOYS

This chapter is based on work that will be submitted for publication to the Journal of Physics: Condensed Matter. The authors are A. Rafi M. Iasir and Karl D. Hammond of the University of Missouri.

4.1   Introduction

High performance research reactors require high-enrichment uranium (HEU) fuels to attain the desired neutron flux. The replacement of HEU fuels with low-enrichment uranium (LEU) is an important antiproliferation initiative. The United States High-Performance Research Reactor (USHPRR) program is currently aiming to replace the HEU fuels currently used in high performance reactors with LEU fuels [1]. LEU fuels require a higher uranium density than that of uranium oxides to compensate the decrease in ^{235}U enrichment. Metallic uranium shows a great promise in this regard.

Metallic fuels are usually chosen because of their high thermal conductivity and high density. Isotropic swelling behaviour is desirable, but uranium, like other light actinides (Pa–Pu), has a low-symmetry crystal structure (the orthorhombic α phase) at ambient temperature and pressure, which results in anisotropic thermal and radiation-induced expansion. Pure uranium has three allotropes at atmospheric pressure: α (base-centred orthorhombic), β (tetragonal), and γ (body-centred cubic). At atmospheric pressure, α-U

65

transforms to β-U at approximately 935 K, and β-U transforms to γ-U at approximately 1045 K [2, 3].

The γ-uranium allotrope (which is body-centred cubic) is preferred to α-uranium by nuclear engineers because it undergoes both isotropic thermal expansion and isotropic radiation-induced swelling [4]. It is not possible to quench pure γ-uranium to room temperature; however, a metastable bcc phase can be obtained at room temperature by alloying with molybdenum [5–8]. A study by Kim-Ngan and Havela [9] showed that the bcc structure can also be retained at temperatures below the ordinary phase transition temperature by alloying uranium with metals such as platinum, palladium, niobium, and zirconium. Molybdenum stabilises uranium's γ phase at concentrations near the eutectoid point (11.1 wt% Mo) and lowers the phase transition temperature from 1045 K for pure γ-uranium to 828 K for a U–Mo alloy at the eutectoid point [10, 11]. Uranium alloyed with 10 wt% molybdenum (U-10Mo, which is approximately 21.6 at.% molybdenum) is currently being developed as a potential high-density, low-enrichment uranium fuel for high-performance research reactors [12–14].

Uranium–molybdenum alloys have been studied extensively both experimentally [6, 15, 16] and theoretically [17–21]. Castellano *et al*. [22] showed that the addition of molybdenum to uranium leads to the stabilisation of the γ phase using *ab initio* molecular dynamics. This thermodynamic stabilisation is important because un-alloyed γ-uranium would quickly revert back to α-uranium, causing high stresses and cracking of the fuel and cladding.

Fission creates a variety of products, resulting in gas bubbles, metallic precipitates, and solutes in the fuel matrix. Among the many fission products, fission gas (*i.e.*, xenon and krypton) produces some of the most significant challenges associated with nuclear fuel development. Fission gas influences the thermal conductivity, causes swelling, and impacts the neutron economy of the reactor [23, 24].

The atomic-scale transport processes in U–Mo alloys are of great interest to understand fuel performance during irradiation. Specifically, the characteristics of fission gas are an

important performance-limiting factor. For these reasons, the behaviour of fission gas has been extensively researched for common fuels such as UO_2 [25–29]. A number of theoretical approaches have also been used to understand the behaviour of fission products in UO_2, including electronic structure theory [30–38]. In particular, vacancies play an important role in the diffusion of xenon because of its size relative to the metal atoms.

Solute diffusion in light actinides is a very interesting phenomenon because such solutes typically have very high diffusivities. Diffusion of solutes in metallic uranium has not been studied extensively. However, there are some early works that provide some information about defect and impurity diffusion in uranium [39–46]. Recently, Smirnova *et al.* [47] studied self-diffusion in γ-uranium and U–Mo alloys using molecular dynamics. They showed that diffusion in γ-uranium is anomalously fast compared to other bcc metals.

In recent years, there have been many attempts to calculate diffusion coefficients using electronic structure and atomistic methods [48–55]. Electronic structure calculations based on DFT and multi-frequency models have shown their usefulness in various works. Five-frequency models of face-centred cubic crystals [56–58] and nine-frequency (or sometimes four-frequency) models of bcc crystals [59, 60] have been widely used. Methods based on electronic structure theory involve calculating the activation energies of an atom jumping to a vacancy in one of the atom's nearest-neighbour positions. This is often referred to as vacancy-mediated diffusion. The calculations employed here are based on DFT coupled with classical transition state theory (TST), which treats vibration using the harmonic oscillator approximation [61, 62].

In this study, we use DFT and TST to study the diffusion of xenon and molybdenum in γ-uranium alloys such as U–7Mo and U–10Mo by varying the local molybdenum concentration around the diffusing solute atom. We find that molybdenum's migration energy is much higher than xenon's in γ–U alloys and that the presence of molybdenum in the local environment of a xenon atom tends to decrease the mobility of xenon in γ-uranium alloys.

We also calculate the vacancy–solute binding energies of several solutes in γ-uranium and find that such binding energies are generally higher in γ-uranium than in iron or aluminium.

4.2 Thermodynamics of Vacancies in Solid

4.3 Theory

Diffusion coefficients in crystalline solids are often described by an Arrhenius equation over a wide range of temperatures. This model consists of two parameters, the migration energy, E_m, and the pre-exponential factor, D_0, with the diffusion coefficient given by

$$D = D_0 e^{-E_m/k_B T},\tag{4.1}$$

where k_B is the Boltzmann constant and T is the absolute temperature. If D_0 is independent of temperature, an Arrhenius plot (D against $1/T$) gives a straight line; if D_0 changes with T, it yields a curve that falls away from the constant-D_0 line at high temperature (the left of the plot).

The migration energy is the activation energy for an atom to jump onto a nearby vacancy. According to classical transition state theory (TST), the rate at which a vacancy exchanges its place with neighbouring atom can be expressed by the Eyring–Polanyi equation [62–64],

$$v = v^\ddagger \exp\left(\frac{-\Delta G_m}{k_B T}\right) \approx \frac{k_B T}{h} \frac{Q_{TS}}{Q_{IS}} \exp\left(\frac{-E_m}{k_B T}\right) \approx \frac{k_B T}{h} \exp\left(\frac{-E_m}{k_B T}\right),\tag{4.2}$$

where Q_{IS} is the vibrational partition function of the initial state and Q_{TS} is the vibrational partition function of the transition state with the vibrational mode along the minimum-energy pathway removed. In the current work, we did not calculate the jump frequencies, which are part of the Q_i terms; we instead make the approximation that the vibrational partition functions not associated with the minimum energy pathway are unity (*i.e.*,

$Q_{\text{TS}}/Q_{\text{IS}} \approx 1$). The diffusion coefficient is proportional to the rate of a jump: $D = \nu\lambda^2/6$, where $\lambda = a/\sqrt{8}$ for bcc lattices [65] and a is the lattice parameter.

Metals that undergo irradiation produce point defects such as self-vacancies and self-interstitials in the lattice. The diffusion of these defects results in microstructural changes that impact the mechanical properties. The diffusion of vacancies is of significant interest because they form voids, dislocation loops, and clusters, and they facilitate the diffusion of substitutional solute atoms. This method of solute diffusion is controlled by the interaction between a vacancy and a solute atom. The diffusion of vacancies is particularly influenced by the presence of nearby substitutional solute atoms. Sometimes the vacancy and the solute can coexist as an atom–vacancy complex. Hence, understanding solute–vacancy interactions is an important step in developing models of diffusion in irradiated materials. The binding energy between vacancies and solute atoms is a key factor in understanding solute diffusion [66, 67]. Nearby solute atoms can influence the energy of solute binding with vacancies. The authors are not aware of any previous results regarding solute–vacancy binding in γ-uranium for any solutes, so we calculated them as part of this work.

We used defects in supercells to calculate the binding energies of solute–vacancy ($X - \square$) pairs. The binding energy is the difference between the energy at infinite separation and the energy at nearest-neighbour separation. We used the following expression to calculate the binding energy of a solute to a vacancy:

$$E_{\text{bind}}^{X-\square} = E_{\text{U}_{N-1}}^{X_1} + E_{\text{U}_{N-1}}^{\square_1} - E_{\text{U}_{N-2}}^{X_1\square_1} - E_{\text{U}_N} \tag{4.3}$$

For a bcc supercell with N sites, the cell may contain no defects (energy E_{U_N}), may contain a vacancy (energy $E_{\text{U}_{N-1}}^{\square_1}$), a solute impurity ($E_{\text{U}_{N-1}}^{X_1}$ or a solute–vacancy pair ($E_{\text{U}_{N-2}}^{X_1\square_1}$). A positive binding energy means the complex is bound. Equation (4.3) can also be conveniently written as the energy required to form a vacancy next to a solute (X) atom. The

vacancy formation energy is

$$E_f^{\square} = E_{\mathrm{U}_{N-1}}^{\square_1} - \frac{N-1}{N} E_{\mathrm{U}_N},$$ (4.4)

where E_{U_N} is the energy of a supercell with N uranium atoms.

The disordered nature of U–Mo alloys creates some challenges for electronic structure studies. The manner in which molybdenum is distributed among the uranium atoms produces different diffusion pathways for xenon, and there are several ways to arrange molybdenum atoms on the lattice sites around a xenon atom. We use a combinatorial approach to assess the probabilities (Table 4.1) of having various numbers of molybdenum atoms in the first-nearest-neighbour shell of the bcc structure around a xenon atom. Assuming the molybdenum atoms are arranged randomly, the probability of a particular U/Mo combination on the sites near a xenon atom can be calculated using the following equation:

$$\mathcal{P} = \binom{n}{k} x_{\mathrm{Mo}}^k (1 - x_{\mathrm{Mo}})^{n-k},$$ (4.5)

where n is the number of available nearest-neighbour positions not occupied by the vacancy (for bcc, $n = 7$), k is the number of molybdenum atoms in the nearest-neighbour shell, and x_{Mo} is the (overall) mole fraction of molybdenum. According to Table 4.1, the probability ($\mathcal{P}$) of having more than three molybdenum atoms in the first nearest-neighbour shell is low ($< 5\%$). We assume, for simplicity, that $x_{\mathrm{Xe}} \approx 0$.

4.4 Methodology

All calculations used the QUANTUM ESPRESSO [68] simulation package with the projector-augmented wave (PAW) method [69]. A full description of the uranium pseudopotential can be found in our earlier work [70]. For the elements Mo, Xe, Fe, Co, Au, Nb, and Zr, we used PAW-based pseudopotentials from the QUANTUM ESPRESSO PS Library [71, 72]. We

Table 4.1. Probability of having different numbers of molybdenum atoms in the nearest-neighbour (NN) location for a bcc uranium–molybdenum alloy. We have used Eq. (4.5) to calculate the probabilities.

# of Mo	U–10Mo ($x_{Mo} = 0.216$)	U–7Mo ($x_{Mo} = 0.157$)
0	0.182	0.302
1	0.351	0.394
2	0.290	0.221
3	0.133	0.069
4	0.037	0.013
5	0.006	0.001
6	0.0006	8.95×10^{-5}
7	2.19×10^{-5}	2.39×10^{-6}

used the exchange–correlation functional of Perdew, Burke, and Ernzerhof (PBE) [73, 74] for all calculations.

DFT calculates the ground state properties of a system; however, γ-uranium is mechanically unstable at 0 K, which results in negative shear moduli [75]. Other elements (*e.g.*, Ti, Zr, Pr, and Hf) also have high-temperature bcc structures that are unstable at low temperature [76, 77]. It is consequently challenging to study γ-uranium with DFT, particularly using a supercell that includes vacancies or defects. To perform our calculations, we used the so-called shell method [78], in which the outer layer of atoms is fixed at crystallographic coordinates and the rest of the atoms are allowed to move freely. We used a $3 \times 3 \times 3$ supercell of bcc uranium, which consists of 54 atoms in the absence of heteroatoms or vacancies. A convergence test showed that a Monkhorst–Pack k-point mesh of $5 \times 5 \times 5$ is suitable to yield formation and migration energies that are converged to within 0.01 eVÅ^{-1}.

To calculate the migration energy, each initial state was relaxed with respect to internal coordinates and volume. We determined the transition state by way of a nudged elastic band (NEB) [79, 80] calculation with a climbing image as implemented in QUANTUM ESPRESSO. We used five images in the NEB calculations.

Table 4.2. Vacancy formation energy (eV) of γ-U compared with previously-published results.

Source	Energy (eV)
Present work	1.28
Beeler *et al.* [78]	1.384
Xian *et al.* [81]	1.08
Matter *et al.* (expt.) [82]	1.2 ± 0.3
Lund *et al.* (expt.) [83]	1.6 ± 0.2

4.5 Results and Discussion

4.5.1 Vacancy Formation and Impurity–Vacancy Binding Energies

The formation energy of a single vacancy is calculated using Eq. (4.4). Our results are compared with previously-published DFT calculations and experimental results in Table 4.2. Our results are in good agreement with both previous DFT studies. Xian *et al.* [81] also used 54 atoms in their supercell, but our vacancy formation energy is higher by 0.2 eV. Discrepancies could arise from their use of a 6×6×6 *k*-point mesh, whereas we used 5×5×5. Beeler *et al.* [78] used a supercell of 128 atoms to calculate the vacancy formation energy. The experimental values bracket our results and those of Beeler *et al.* [78]: The earlier work of Matter *et al.* [82] found a formation energy of 1.2 ± 0.3 eV, whereas Lund *et al.* [83] found 1.6 ± 0.2 eV.

We are not aware of any previous reports of calculations of solute–vacancy ($X - \square$) binding energies in γ-uranium, so we calculated these ourselves. We chose solutes so as to compare to diffusion measurements by Rothman and coworkers [40–42]. The results are shown in Table 4.3. All of the solute–vacancy binding energies in γ-uranium are substantially higher than in other bcc metals. For example, in aluminium and magnesium, the $X - \square$ binding energy varies from −0.4 to 0.5 eV for a variety of solutes [67, 84, 85]. In γ-uranium, however, the binding energy varies from 5.715 eV ($Fe - \square$) to 6.619 eV ($Cr - \square$),

Table 4.3. Solute–vacancy binding energies in γ-uranium for various solutes near a vacancy. Positive energies indicate energetically-favourable binding.

Solute	Binding energy (eV)
Xe	6.034
Mo	6.249
Fe	5.715
Co	5.876
Au	6.450
Cr	6.619
Zr	6.318
Nb	6.113

which indicates that the solute–vacancy binding energy is much higher in bcc uranium than it is in other bcc metals.

The solute–vacancy binding energy characterizes the interaction between a solute and a vacancy, which modifies the local concentration of vacancies near a solute. In the case of γ-uranium, the interaction between solute and vacancy is strongly attractive. The total solute–vacancy binding energy can be decomposed into two factors: elastic effects and electrostatic effects [86]. The elastic energy (or elastic binding energy) is the energy that is released if the strain fields of a solute and a vacancy interact [87, 88]. Due to the unstable nature of γ-U at low temperatures, the elastic binding energy contributes the most to the total solute–vacancy binding energy and is the primary reason for the high value of the solute–vacancy binding energy in bcc uranium.

4.5.2 Xenon and Molybdenum Diffusion

Migration energies are calculated using the climbing-image nudged elastic band method. We calculated the migration energies of xenon and molybdenum moving from the centre of the supercell to one of the nearest-neighbour lattice sites. Such solute–vacancy exchange is the primary mechanism of diffusion of xenon and molybdenum because of their size relative to uranium. Table 4.4 presents our findings. Note that in bcc lattices, all eight

nearest-neighbour sites are symmetrically equivalent, so there is only one unique migration energy for xenon near seven uranium atoms and one vacancy. As the amount of molybdenum in the nearest-neighbor shell increases, there are more and more symmetrically distinct migration pathways. Xenon's migration energy in the absence of any molybdenum in the nearest-neighbour positions is significantly lower than molybdenum's migration energy. The Xe$-\square$ binding energy is also lower than the Mo$-\square$ binding energy, which may occur in part because xenon tends to find its energetic minimum location in between the empty lattice site and the site closest to the xenon atom, resulting in shorter jump distances and lower barriers.

We studied the xenon migration energy in the presence of molybdenum in a systematic way by including various numbers of molybdenum atoms in the nearest-neighbour (NN) shell around a xenon atom and calculating all symmetrically distinct xenon migration energies associated with each distinct arrangement of molybdenum atoms around a central xenon atom. One molybdenum in the NN shell creates three symmetrically equivalent xenon jumps (see Fig. 4.1b). These three migration pathways (labeled 1, 2, and 3) show higher activation energies than the case with no molybdenum in the NN shell.

There is more than one way to put two molybdenum atoms in the NN shell around a solute atom in a bcc crystal, and each of these arrangements creates a distinct xenon migration pathway. Figure 4.2 shows all symmetrically-distinct locations for two molybdenum atoms around a xenon atom and the resulting symmetrically-distinct jumps that could result if a vacancy were in another position nearby. Migration energies with two molybdenum atoms present range from 0.110 eV to 0.532 eV. Both the positions of the two molybdenum atoms and direction of the migration influence the migration energy. Directions 1 and 2 (Fig. 4.2a) have migration energies of 0.110 and 0.212 eV, respectively; direction 2 has almost double the migration energy of direction 1. Directions 1, 4 and 6, which all have a molybdenum atom on the corner of the cube adjacent to the vacancy, have the lowest migration energies.
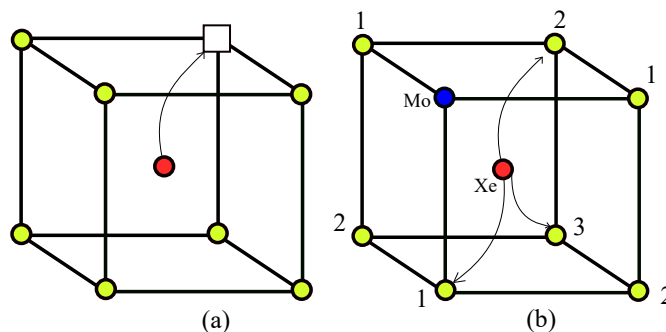
Figure 4.1. (a) Diagram of a xenon jump from the centre site to a nearest-neighbour vacancy in γ-uranium. (a) All eight jumps are symmetrically equivalent with no molybdenum present; (b) with one molybdenum atom in the nearest neighbour shell, there are three unique solute jumps (1, 2, and 3).

Figure 4.3 shows the symmetrically-distinct arrangements of three molybdenum atoms in the nearest neighbour shell. This local concentration creates seven distinct jumps of a xenon atom to the nearest neighbour vacancy (Fig. 4.3). The migration energies for three-molybdenum configurations vary from 0.201 eV for direction 4 to 1.213 eV for direction 7. The highest migration energy is for a xenon atom that jumps to a site between two molybdenum atoms (site 7 in Fig. 4.3c). Figure 4.3a shows the arrangements of three molybdenum on the same (1 0 0) plane, which produces three distinct jumps with migration energies ranging from 0.515 eV to 0.917 eV, the highest one being for direction 3, where xenon moves to the opposite corner from the three molybdenum atoms. Figure 4.3b has a combination of two molybdenum atoms on one face of the cell and one molybdenum in the lower corner on the opposite site. This configuration reduces the migration energy compared to the configuration in which all three molybdenum atoms are coplanar.

We did not calculate the migration energy of xenon with more than three molybdenum atoms in the nearest-neighbour shell. The assumption of a random (binomial) distribution (Table 4.1) implies that the probability of having 0–3 molybdenum is much higher (> 96%) than having more than three molybdenum in U-10Mo or U-7Mo.

75
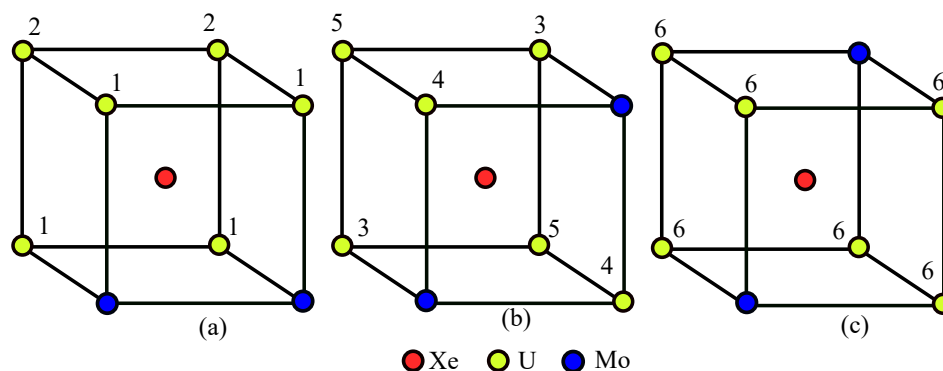
Figure 4.2. The three sets of symmetrically-inequivalent hops of xenon from the centre with two molybdenum atoms in the nearest-neighbour shell. The numbers denote symmetrically distinct pathways.
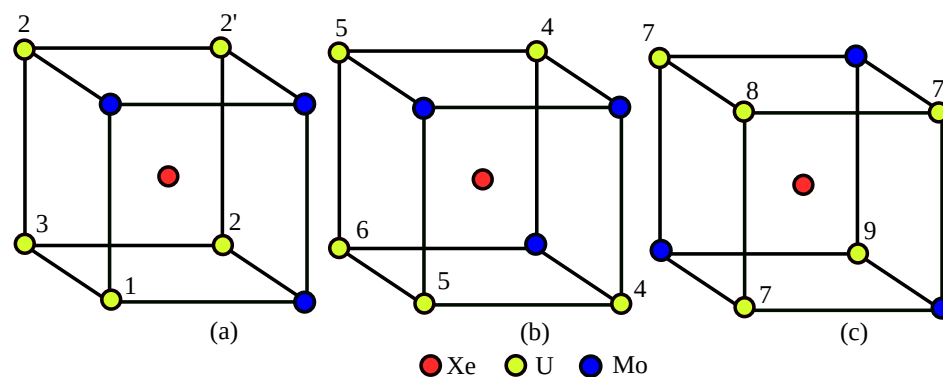
Figure 4.3. The three sets of symmetrically-distinct hops from the centre site with three molybdenum atoms in the nearest-neighbour shell. The numbers denote symmetrically distinct pathways.

Table 4.4. Xenon migration energy (E_m) for different configurations.

Composition[a]	Xe Jump	E_m (eV)
7 U	$\langle 1\,1\,1 \rangle$ (Fig. 4.1a)	0.161
1 Mo	1 (Fig. 4.1b)	0.313
	2 (Fig. 4.1b)	0.172
	3 (Fig. 4.1b)	0.261
2 Mo	1 (Fig. 4.2a)	0.110
	2 (Fig. 4.2a)	0.212
	3 (Fig. 4.2b)	0.532
	4 (Fig. 4.2b)	0.108
	5 (Fig. 4.2b)	0.224
	6 (Fig. 4.2c)	0.110
3 Mo	1 (Fig. 4.3a)	0.515
	2 (Fig. 4.3a)	still running
	2′ (Fig. 4.3a)	0.917
	3 (Fig. 4.3a)	0.579
	4 (Fig. 4.3b)	0.201
	5 (Fig. 4.3b)	0.384
	6 (Fig. 4.3b)	0.386
	7 (Fig. 4.3c)	1.213
	8 (Fig. 4.3c)	still running
	9 (Fig. 4.3c)	still running
	Mo Jump	E_m (eV)
7 U	$\langle 1\,1\,1 \rangle$ (Fig. 4.1a)	2.067

[a]The eight nearest-neighbour sites consist of one vacancy plus the atoms listed, with the remaining sites occupied by uranium atoms.

4.6 Conclusions

We calculated solute–vacancy binding energies for different solutes in bcc uranium. Uranium shows relatively high vacancy–solute binding energies compared to iron and aluminium. The unstable nature of γ-U at low temperature contributes to a significant increase in solute–vacancy binding energy relative to other bcc metals. The higher elastic binding energy in bcc uranium produces a high solute–vacancy binding energy.

We also calculated migration energies of xenon and molybdenum in pure bcc uranium. Molybdenum's migration energy is very high compared to that of xenon, indicating that in pure bcc uranium, xenon moves much faster than molybdenum. The relatively low diffusivity of molybdenum also supports our assumptions that molybdenum is randomly distributed in uranium–molybdenum alloys. We also studied migration energies of xenon in the presence of molybdenum in U–Mo alloys. Different combinations of molybdenum in the nearest neighbour and xenon's distinct jump paths are identified and studied. A combinatorial analysis suggests that having up to three molybdenum atoms in the nearest-neighbour shell is highly probable in U-10Mo and U-7Mo alloys. The presence of molybdenum in the nearest neighbour shell of a xenon atom has an impact on the migration energy, but it does not generally increase or decrease the migration energy; both the location of the molybdenum atoms and direction of the jump influence the migration energy. Having one molybdenum atom in the nearest-neighbour shell increases the activation energy between 0.01 eV and 0.15 eV, depending on the location of the molybdenum atom relative to the xenon atom and the vacancy. If xenon has two molybdenum atoms nearby, we found a similar increase, though there are combinations for which the migration energy is lower than it is in the single-molybdenum cases. For xenon with three nearby molybdenum atoms, the migration energy increases for all molybdenum/vacancy arrangements. While there are several molybdenum arrangements that result in decreased migration energies relative to some of the two-molybdenum configurations, the general trend with the addition of molybdenum in

the nearest neighbour shell near xenon is to increase the migration energy, hence reducing xenon mobility in U–Mo alloys.

We did not consider the influence of molybdenum in the second-nearest neighbour shell in bcc uranium. Future work should include a determination of diffusion coefficient of xenon using the kinetic Monte Carlo method.

References

1. James L. Snelgrove, G. L. Hofman, M. K. Meyer, C. L. Trybus, and T. C. Wiencek. Development of very-high-density low-enriched-uranium fuels. *Nucl. Eng. Des.*, 178(1):119–126, 1997.

2. A C Lawson, C E Olsen, J W Richardson, M H Mueller, and G H Lander. Structure of β-uranium. *Acta Crystallogr. B*, 44(2):89–96, 1988.

3. J Akella, S Weir, J M Wills, and P Söderlind. Structural stability in uranium. *J. Phys. Condens. Matter*, 9(39):L549–L555, 1997.

4. J H Kittel, B R T Frost, J P Mustelier, K Q Bagley, G C Crittenden, and J Van Dievoet. History of fast reactor fuel development. *J. Nucl. Mater.*, 204:1–13, 1993.

5. A S Wilson and R E Rundle. The structures of uranium metal. *Acta Crystallogr.*, 2(2):126–127, 1949.

6. V P Sinha, P V Hegde, G J Prasad, G K Dey, and H S Kamath. Phase transformation of metastable cubic γ-phase in u–mo alloys. *J. Alloy Compd.*, 506(1):253–262, 2010.

7. Harry L Yakel. Crystal structures of transition phases formed in U/16.60 at% Nb/5.64 at% Zr alloys. *J. Nucl. Mater.*, 33(3):286–295, 1969.

8. V P Sinha, P V Hegde, G J Prasad, G K Dey, and H S Kamath. Effect of molybdenum addition on metastability of cubic γ-uranium. *J. Alloy Compd.*, 491(1-2):753–760, 2010.

9. N.-T. H Kim-Ngan and L. Havela. Superconductivity in U-T alloys (T = Mo, Pt, Pd, Nb, Zr) stabilized in the cubic γ-U structure by splat-cooling technique. *J. Sci. Adv. Mater. Dev.*, 1(2):121–127, 2016.

10. Hiroaki Okamoto, Mark E. Schlesinger, and Erik M. Mueller, editors. *Mo (Molybdenum) Binary Alloy Phase Diagrams*, volume 3 of *ASM Handbook*, pages 489–498. ASM International, 2016.

11. A. Berche, N. Dupin, C. Guénau, C. Rado, B. Sundman, and J. C. Dumas. Calphad thermodynamic description of some binary systems involving U. *J. Nucl. Mater.*, 411:131–143, 2011.

12. Ramprashad Prabhakaran. U-mo monolithic fuel for nuclear research and test reactors. *JOM*, 69(12):2529–2531, 2017.

13. M. K. Meyer, J. Gan, J. F. Jue, D. D. Keiser, E. Perez, A. Robinson, D. M. Wachs, N. Woolstenhulme, G. L. Hofman, and Y. S. Kim. Irradiation performance of U-Mo monolithic fuel. *Nucl. Eng. Technol.*, 46(2):169–182, 2014.

14. WJ Williams, AB Robinson, and BH Rabin. Post-irradiation non-destructive analyses of the afip-7 experiment. *JOM*, 69(12):2546–2553, 2017.

15. Austin E Dwight. The uranium-molybdenum equilibrium diagram below 900 C. *J. Nucl. Mater.*, 2(1):81–87, 1960.

16. K Tangri and GI Williams. Metastable phases in the uranium molybdenum system and their origin. *J. Nucl. Mater.*, 4(2):226–233, 1961.

17. A Berche, N Dupin, C Guéneau, C Rado, B Sundman, and J C Dumas. Calphad thermodynamic description of some binary systems involving U. *J. Nucl. Mater.*, 411(1-3):131–143, 2011.

18. X Zhang, Y F Cui, G L Xu, W J Zhu, H S Liu, B Y Yin, and Z P Jin. Thermodynamic assessment of the U–Mo–Al system. *J. Nucl. Mater.*, 402(1):15–24, 2010.

19. E L Losada and J E Garcés. On the ground state of the U-Mo system. *J. Nucl. Mater.*, 518:380–385, 2019.

20. A Landa, P Söderlind, and P E A Turchi. Density-functional study of U–Mo and U–Zr alloys. *J. Nucl. Mater.*, 414(2):132–137, 2011.

21. P R Alonso and G H Rubiolo. The role of multisite interactions in the formation energy of bcc γ (U, Mo) disordered phase. *Model. Simulat. Mater. Sci. Eng.*, 15(3):263, 2007.

22. Aloïs Castellano, François Bottin, Boris Dorado, and Johann Bouchet. Thermodynamic stabilization of γ-U–Mo alloys: Effect of Mo content and temperature. *Phys. Rev. B*, 101(18):184111, 2020.

23. Vincenzo V. Rondinella and Thierry Wiss. The high burn-up structure in nuclear fuel. *Mater. Today*, 13(12):24–32, 2010.

24. A Rafi M Iasir, Nickie J Peters, and Karl D Hammond. Estimation of effective thermal conductivity in u-10mo fuels with distributed xenon gas bubbles. *J. Nucl. Mater.*, 508:159–167, 2018.

25. Younsuk Yun, Hanchul Kim, Heemoon Kim, and Kwangheon Park. Atomic diffusion mechanism of Xe in UO_2. *J. Nucl. Mater.*, 378(1):40–44, 2008.

26. J C Carter, E J Driscoll, and T S Elleman. Xenon-133 diffusion and trapping in single-crystal uranium dioxide. *Phys. Status Solidi A*, 14(2):673–680, 1972.

27. Hj Matzke. Diffusion in doped UO_2. *Nucl. Appl.*, 2(2):131–137, 1966.

28. J R MacEwan and W H Stevens. Xenon diffusion in UO_2: Some complicating factors. *J. Nucl. Mater.*, 11(1):77–93, 1964.

29. Katsumi Une, Isami Tanabe, and Masaomi Oguma. Effects of additives and the oxygen potential on the fission gas diffusion in UO_2 fuel. *J. Nucl. Mater.*, 150(1):93–99, 1987.

30. Charles Richard Arthur Catlow. Fission gas diffusion in uranium dioxide. *Proc. Roy. Soc. Lond. Math. Phys. Sci.*, 364(1719):473–497, 1978.

31. R A Jackson, A D Murray, J H Harding, and C R A Catlow. The calculation of defect parameters in UO_2. *Philos. Mag. A*, 53(1):27–50, 1986.

32. Robin W Grimes, C Richard A Catlow, and A Marshall Stoneham. Calculations of solution energies of fission products in uranium dioxide. *J. Am. Ceram. Soc.*, 72(10):1856–1860, 1989.

33. Richard G J Ball and Robin W Grimes. Diffusion of Xe in UO_2. *J. Chem. Soc. Faraday Trans.*, 86(8):1257–1261, 1990.

34. R W Grimes and Charles Richard Arthur Catlow. The stability of fission products in uranium dioxide. *Phil. Trans. A Math. Phys. Eng. Sci.*, 335(1639):609–634, 1991.

35. Th Petit, G Jomard, C Lemaignan, B Bigot, and A Pasturel. Location of krypton atoms in uranium dioxide. *J. Nucl. Mater.*, 275(1):119–123, 1999.

36. Jean-Paul Crocombette. Ab initio energetics of some fission products (Kr, I, Cs, Sr and He) in uranium dioxide. *J. Nucl. Mater.*, 305(1):29–36, 2002.

37. M Freyss, N Vergnet, and T Petit. Ab initio modeling of the behavior of helium and xenon in actinide dioxide nuclear fuels. *J. Nucl. Mater.*, 352(1–3):144–150, 2006.

38. D A Andersson, B P Uberuaga, P V Nerikar, C Unal, and C R Stanek. U and Xe transport in $UO_2 \pm x$: Density functional theory calculations. *Phys. Rev. B*, 84(5):054105, 2011.

39. Y Adda and A Kirianenko. Etude de l'autodiffusion de l'uranium en phase γ. *J. Nucl. Mater.*, 1(2):120–126, 1959.

40. N L Peterson and S J Rothman. Diffusion in gamma uranium. *Phys. Rev.*, 136(3A):A842, 1964.

41. S J Rothman, L T Lloyd, R Weil, and A L Harkness. Self-diffusion in gamma uranium. Technical report, Argonne National Lab., Lemont, Ill., 1959.

42. S J Rothman. The diffusion of gold in gamma uranium. *J. Nucl. Mater.*, 3(1):77–80, 1961.

43. Y Adda and A Kirianenko. Etude de l'autodiffusion de l'uranium en phase α. *J. Nucl. Mater.*, 6(1):130–134, 1962.

44. R Resnick and L L Seigle. The self-diffusion of alpha-uranium. *J. Nucl. Mater.*, 5(1):5–11, 1962.

45. S J Rothman, J Gray, Jr, J P Hughes, and A L Harkness. Self-diffusion in beta uranium. *J. Nucl. Mater.*, 3(1):72–76, 1961.

46. Yajun Liu, Di Yu, Yong Du, Guang Sheng, Zhaohui Long, Jiang Wang, and Lijun Zhang. Atomic mobilities, diffusivities and their kinetic implications for U–X (X = Ti, Nb and Mo) bcc alloys. *Calphad*, 37:49–56, 2012.

47. D E Smirnova, A Yu Kuksin, S V Starikov, and V V Stegailov. Atomistic modeling of the self-diffusion in γ-U and γ-U-Mo. *Phys. Met. Metallogr.*, 116(5):445–455, 2015.

48. J B Adams, S M Foiles, and W G Wolfer. Self-diffusion and impurity diffusion of fee metals using the five-frequency model and the embedded atom method. *J. Mater. Res.*, 4(1):102–112, 1989.

49. Peter E Blöchl, Enrico Smargiassi, Roberto Car, D B Laks, W Andreoni, and S T Pantelides. First-principles calculations of self-diffusion constants in silicon. *Phys. Rev. Lett.*, 70(16):2435, 1993.

50. Peter E Blöchl, C G Van de Walle, and S T Pantelides. First-principles calculations of diffusion coefficients: Hydrogen in silicon. *Phys. Rev. Lett.*, 64(12):1401, 1990.

51. W Frank, U Breier, C Elsässer, and M Fähnle. First-principles calculations of absolute concentrations and self-diffusion constants of vacancies in lithium. *Phys. Rev. Lett.*, 77(3):518, 1996.

52. A Janotti, M Krčmar, C L Fu, and R C Reed. Solute diffusion in metals: Larger atoms can move faster. *Phys. Rev. Lett.*, 92(8):085901, 2004.

53. M Krčmar, Chong Long Fu, Anderson Janotti, and R C Reed. Diffusion rates of 3d transition metal solutes in nickel by first-principles calculations. *Acta Mater.*, 53(8):2369–2376, 2005.

54. V Milman, M C Payne, V Heine, R J Needs, J S Lin, and M H Lee. Free energy and entropy of diffusion by ab initio molecular dynamics: Alkali ions in silicon. *Phys. Rev. Lett.*, 70(19):2928, 1993.

55. Nils Sandberg, Blanka Magyari-Köpe, and Thomas R Mattsson. Self-diffusion rates in Al from combined first-principles and model-potential calculations. *Phys. Rev. Lett.*, 89(6):065901, 2002.

56. A. B. Lidiard. CXXXIII. Impurity diffusion in crystals (mainly ionic crystals with the sodium chloride structure). *Philos. Mag. Series 7*, 46(382):1218–1237, 1955.

57. A. B. Lidiard. The influence of solutes on self-diffusion in metals. *Philos. Mag. A*, 5(59):1171–1180, 1960.

58. A. D. Leclaire and A. B. Lidiard. LIII. Correlation effects in diffusion in crystals. *Philos. Mag. A*, 1(6):518–527, 1956.

59. A. D. Le Claire. Solvent self-diffusion in dilute b.c.c. solid solutions. *Philos. Mag. A*, 21(172):819–832, 1970.

60. Helmut Mehrer. *Diffusion in Solids: Fundamentals, Methods, Materials, Diffusion-Controlled Processes*, volume 155. Springer Science & Business Media, 2007.

61. G H Vineyard and G J Dienes. The theory of defect concentration in crystals. *Phys. Rev.*, 93(2):265–268, 1954.

62. George H Vineyard. Frequency factors and isotope effects in solid state rate processes. *J. Phys. Chem. Solid*, 3(1-2):121–127, 1957.

63. Henry Eyring. The activated complex in chemical reactions. *J. Chem. Phys.*, 3(2):107–115, February 1935.

64. M. G. Evans and M. Polanyi. Some applications of the transition state method to the calculation of reaction velocities, especially in solution. *Trans. Faraday Soc.*, 31:875–894, 1935.

65. K. Heinola and T. Ahlgren. Diffusion of hydrogen in bcc tungsten studied with first principle calculations. *J. Appl. Phys.*, 107(11):113531, 2010.

66. R. W. Balluffi and P. S. Ho. *Diffusion*, page 83. American Society for Metals, Metals Park, Ohio, 1973.

67. C Wolverton. Solute–vacancy binding in aluminum. *Acta Mater.*, 55(17):5867–5872, 2007.

68. Paolo Giannozzi, Stefano Baroni, Nicola Bonini, Matteo Calandra, Roberto Car, Carlo Cavazzoni, Davide Ceresoli, Guido L. Chiarotti, Matteo Cococcioni, Ismaila Dabo, Andrea Dal Corso, Stefano de Gironcoli, Stefano Fabris, Guido Fratesi, Ralph Gebauer, Uwe Gerstmann, Christos Gougoussis, Anton Kokalj, Michele Lazzeri, Layla Martin-Samos, Nicola Marzari, Francesco Mauri, Riccardo Mazzarello, Stefano Paolini, Alfredo Pasquarello, Lorenzo Paulatto, Carlo Sbraccia, Sandro Scandolo, Gabriele Sclauzero, Ari P. Seitsonen, Alexander Smogunov, Paolo Umari, and Renata M. Wentzcovitch. QUANTUM ESPRESSO: A modular and open-source software project for quantum simulations of materials. *J. Phys. Condens. Matter*, 21(39):395502, September 2009. http://www.quantum-espresso.org/.

69. P. E. Blöchl. Projector augmented-wave method. *Phys. Rev. B*, 50(24):17953–17979, December 1994.

70. A Rafi M Iasir and Karl D Hammond. Pseudopotential for plane-wave density functional theory studies of metallic uranium. *Comput. Mater. Sci.*, 171:109221, 2020.

71. QUANTUM ESPRESSO. PS library. http://www.quantum-espresso.org/pseudopotentials, 2019.

72. Andrea Dal Corso. Pseudopotentials periodic table: From H to Pu. *Comput. Mater. Sci.*, 95:337–350, 2014.

73. John P. Perdew, Kieron Burke, and Matthias Ernzerhof. Generalized gradient approximation made simple. *Phys. Rev. Lett.*, 77(18):3865–3868, October 1996.

74. John P. Perdew, Kieron Burke, and Matthias Ernzerhof. Generalized gradient approximation made simple (errata). *Phys. Rev. Lett.*, 78(7):1396, 1997.

75. Per Soderlind. Theory of the crystal structures of cerium and the light actinides. *Adv. Phys.*, 47(6):959–998, 1998.

76. Y.-Y. Ye, Y. Chen, K.-M. Ho, B. N. Harmon, and P.-A. Lindgrd. Phonon-phonon coupling and the stability of the high-temperature bcc phase of Zr. *Phys. Rev. Lett.*, 58(17):1769–1772, 1987.

77. J M Sanchez and D De Fontaine. Model for anomalous self-diffusion in group-IV B transition metals. *Phys. Rev. Lett.*, 35(4):227–230, 1975.

78. B Beeler, B Good, S Rashkeev, C Deo, M Baskes, and M Okuniewski. First principles calculations for defects in U. *J. Phys. Condens. Matter*, 22(50):505703, 2010.

79. Graeme Henkelman, Blas P Uberuaga, and Hannes Jónsson. A climbing image nudged elastic band method for finding saddle points and minimum energy paths. *J. Chem. Phys.*, 113(22):9901–9904, 2000.

80. Graeme Henkelman and Hannes Jónsson. Improved tangent estimate in the nudged elastic band method for finding minimum energy paths and saddle points. *J. Chem. Phys.*, 113(22):9978–9985, 2000.

81. Shikai Xiang, Hanchen Huang, and LM Hsiung. Quantum mechanical calculations of uranium phases and niobium defects in γ-uranium. *J. Nucl. Mater.*, 375(1):113–119, 2008.

82. H Matter, J Winter, and W Triftshäuser. Investigation of vacancy formation and phase transformations in uranium by positron annihilation. *J. Nucl. Mater.*, 88(2-3):273–278, 1980.

83. K R Lund, K G Lynn, M H Weber, and M A Okuniewski. Vacancy formation enthalpy in polycrystalline depleted uranium. *J. Phys. Conf. Ser.*, 443:012021, 2013.

84. Dongwon Shin and Christopher Wolverton. First-principles study of solute–vacancy binding in magnesium. *Acta Mater.*, 58(2):531–540, 2010.

85. James E Saal and C Wolverton. Solute–vacancy binding of the rare earths in magnesium from first principles. *Acta Mater.*, 60(13–14):5151–5159, 2012.

86. J Burke. The measurement of solute-vacancy interaction energies. *Journal of the Less-Common Metals*, 28:441–456, 1972.

87. Xiang-Shan Kong, Xuebang Wu, Yu-Wei You, CS Liu, QF Fang, Jun-Ling Chen, G-N Luo, and Zhiguang Wang. First-principles calculations of transition metal–solute interactions with point defects in tungsten. *Acta Mater.*, 66:172–183, 2014.

88. Toshiharu Ohnuma, Naoki Soneda, and Misako Iwasawa. First-principles calculations of vacancy–solute element interactions in body-centered cubic iron. *Acta Mater.*, 57(20):5947–5955, 2009.

CHAPTER 5

CONCLUSIONS AND FUTURE WORK

Things to cover here in the future work.

- How can I improve the model for thermal conductivity model.

- Can include grain boundary growth. Can through in a swelling model.

- Studying the stability of U–Mo alloy with respect to temperature, which can be studied using ab initio molycular dynamcis.

- Collecting all the rate limiting steps of xenon diffusion in u–mo alloys.

- Come up with a kinetic Monte Carlo Method.

- Improve the model somehow , I don't know how.

APPENDIX A

ATOMIC UNITS

There are special units of measurement which is convenient for atomic physics and DFT calculations. They are named after the Physicist Douglas Hatree [1]. In this system the numerical values of the four fundamental physical constants are assumed to be unity. They are as follows:

- Reduced planck constant: $\hbar = 1$, atomic unit of action.

- Elementary Charge: $e = 1$, atomic unit of charge.

- Bohr radius: $a_0 = 1$, atomic unit of length.

- Electronic mass: $m_e = 1$, atomic unit of mass.

Now we will explore how it simplifies quantum mechanical calculation of hydrogen atom. The hydrogen atom consists of a heavy proton (charge e) with a much lighter electron (charge $-e$) that orbits around it. The potential energy (in SI units) is

$$V(\mathbf{r}) = -\frac{Ze^2}{4\pi\epsilon_0|r|} \tag{A.1}$$

where Z is the atomic number and $\mathbf{r}$ is the position relative to the nuclear site. The radial Schrödinger equation including the centrifugal term is:

$$\left[-\frac{\hbar^2}{2m_e}\nabla_r^2 + \frac{\hbar^2\ell(\ell+1)}{2m_e r^2} - \frac{Ze^2}{4\pi\epsilon_0|r|} - E\right]rR(r) = 0 \tag{A.2}$$

The above equation can be simplified by introducing dimensionless quantities. Multiplying Eq. (A.2) with $m_e/\hbar^2$ the equation becomes:

$$\left[-\nabla_r^2 + \frac{\ell(\ell+1)}{r^2} + \frac{2m_eZe^2}{4\pi\epsilon_0\hbar^2}\frac{1}{r} - \frac{2m_eE}{\hbar^2}\right]rR(r) = 0$$

$$\left[-\frac{1}{2}\nabla_r^2 + \frac{\ell(\ell+1)}{2r^2} + \frac{Z}{a_0r} - \frac{E}{E_0a_0^2}\right]rR(r) = 0 \tag{A.3}$$

$$\left[-\frac{1}{2}\nabla_\zeta^2 + \frac{\ell(\ell+1)}{2\zeta^2} + \frac{Z}{\zeta} - \frac{E}{E_0}\right]\zeta R(\zeta a_0) = 0$$

The above equation has two units, one is for length scale, the Bohr radius a_0 and the other one is an energy scale, the Hartree E_0.

A.0.1 Bohr Radius

$$a_0 = \frac{4\pi\epsilon_0\hbar^2}{m_e e^2} \tag{A.4}$$

The Bohr radius is the length unit of the Hatree atomic unit system. It corresponds to the radius of a classical electron circling a proton at the ground energy of the hydrogen atom. Using all the fundamental constants in Eq. (A.4) the standard atomic unit of Bohr becomes

$$1 \text{ bohr} = \frac{4\pi\epsilon_0\hbar^2}{m_e e^2} = 0.529\,177\,25 \times 10^{-10}\text{m} = 0.52917725 \text{ Å} \tag{A.5}$$

A.0.2 Hatree

$$E_0 = \frac{\hbar^2}{m_e a_0^2} = \frac{m_e e^4}{(4\pi\epsilon_0\hbar)^2} \tag{A.6}$$

The Hartree is the energy unit in the Hatree atomic unit system. One Hartree is twice the binding energy of an electron in the hydrogen atom. To satisfy $a_0 = 1$, all the fundamental units becomes unity ($\hbar = m_e = e = 4\pi\epsilon_0 = 1$), according to Eq. (A.4). The unit of Hatree

can also be calculated from the fundamental units.

$$1 \text{ hartree} = \frac{\hbar^2}{m_e a_0^2} = \frac{m_e e^4}{(4\pi\epsilon_0\hbar)^2} = 4.359\,748\,2 \times 10^{-10}\text{J} = 27.211396 \text{ eV} \tag{A.7}$$

In Hatree units, the Schrödinger equation of an electron in the Coulomb potential of the nucleus has the following form:

$$\left(-\frac{1}{2}\nabla^2 - \frac{Z}{r} - E\right)|\psi\rangle = 0 \tag{A.8}$$

A.0.3 Rydberg Atomic Units

The Rydberg atomic unit is another useful atomic unit which is widely used in DFT and atomic physics. In Hatree atomic units, the assumption is $\hbar^2/2m_e = \frac{1}{2}$. In Rydberg atomic units the assumption is:

$$\hbar = 2m_e = e^2/2 = 1$$

Using the above relations, the length unit does not change in Rydberg units.

$$a_0 = \frac{4\pi\epsilon_0\hbar^2}{2m_e e^2/2} = \frac{4\pi\epsilon_0\hbar^2}{m_e e^2} = 0.52917725 \text{ Å} \tag{A.9}$$

The energy unit does change as follows:

$$1 \text{ Ry} = \frac{\hbar^2}{2m_e a_0^2} = \frac{1}{2}\frac{\hbar^2}{m_e a_0^2} = 13.605693 \text{ eV} \tag{A.10}$$

References

1. Douglas R Hartree. The wave mechanics of an atom with a non-coulomb central field. part i. theory and methods. *Mat. Proc. Cambridge Philos. Soc.*, 24:89, 1928.

APPENDIX B

HELIUM INTERACTION WITH BCC LITHIUM

Lithium is one of the promising plasma facing material in ITER. In the near surface of plasma facing materials high density of interstitials and vacancies are being produced in addition to higher concentration of hydrogen and helium. This defects and gases will change the microstructure of the material. It is therefore important to determine the property of point defects in Lithium and its interaction with helium atom.

We perform all our calculations using density functional theory (DFT) with plane-wave basis sets as implemented in the software QUANTUMESPRESSO []. The PAW based pseudopotential were used from PS library. The generalized gradient approximation of Perdew–Burke–Ernzerhof (PBE) was used as exchange-correlation functional []. We used a $4 \times 4 \times 4$ of bcc lithium, which consists of 128 atoms to simulate point defects. Brillouin zone sampling was performed using Monkhorst and Pack scheme []. The plane wave cutoff energy was 50 Ry. The equilibrium lattice parameter obtained was 3.436 Å. All the calculations were performed at constant volume fully relaxing the atomic positions in the supercells.

The formation energies are calculated as follows:

$$
\begin{aligned}
E_{\text{oct}}^{f} &= E_{\text{Li}+\text{He}_{\text{oct}}} - E_{\text{Li}} - E_{\text{He}_{\text{iso}}} \\
E_{\text{tetr}}^{f} &= E_{\text{Li}+\text{He}_{\text{tetr}}} - E_{\text{Li}} - E_{\text{He}_{\text{iso}}} \\
E_{\square}^{f} &= E_{\text{Li}}^{\square_{1}} - \frac{N-1}{N} E_{\text{Li}_{N}} \\
E_{\text{subs}}^{f} &= E_{\text{Li}+\text{He}_{\square}} - \frac{N-1}{N} E_{\text{Li}_{N}} - E_{\text{He}_{\text{iso}}}
\end{aligned}
\tag{B.1}
$$

Table B.1. Formation energies (in eV) for a single He atom positioned in the octahedral or tetrahedral interstitial sites as well as in substitution. He migration energy (eV). The Calculations are done using 128 atom supercells.

eV	Li–He	W–He [1]	Fe–He [2]
E_{oct}^{f}	1.142	6.38	4.60
E_{tetr}^{f}	1.132	6.16	4.37
E_{subs}^{f}	1.213	4.70	4.08
E_{mig}^{t-t}	0.003	0.06	0.06

Table B.2. Formation of He–He dumbbells around a vacancy in lithium using (B.4)

Dumbbell Configuration	Formation Energy (eV)
$\langle 1\,1\,1 \rangle$	1.348
$\langle 1\,1\,0 \rangle$	1.367
$\langle 0\,1\,0 \rangle$	1.383

The binding energy between vacancy and solute is calculated as follows

$$E_{\text{b}}^{\text{He}-\square} = E_{\text{Li}_{N-1}}^{\text{He}_1} + E_{\text{Li}_{N-1}}^{\square_1} - E_{\text{U}_{N-2}}^{\text{He}_1\square_1} - E_{\text{Li}_N} \tag{B.2}$$

The binding energies of two helium atoms is determined as obtained as:

$$E_{\text{b}}^{A_1-A_2} = E_N^{A_1} + E_N^{A_2} - E_N^{A_1+A_2} - E_N \tag{B.3}$$

The He–He dumbbell formation energy can be calculated using the following equation:

$$E_f^{\text{He}-\square-\text{He}} = E_{N-1}^{\text{He}-\square-\text{He}} - E_{N-1}^{\square} - 2E_{\text{He}_{\text{iso}}} \tag{B.4}$$

References

1. CS Becquart and C Domain. Ab initio calculations about intrinsic point defects and he in w. *Nuclear Instruments and Methods in Physics Research Section B: Beam Interactions with Materials and Atoms*, 255(1):23–26, 2007.

2. Tatiana Seletskaia, Yuri Osetsky, Roger E Stoller, and George Malcolm Stocks. Magnetic interactions influence the properties of helium defects in iron. *Phys. Rev. Lett.*, 94(4):046403, 2005.

APPENDIX C

ORTHOGONAL PLANE WAVE

For now we will try to approximate time-independent Schrödinger equation so that we can achieve self-consistency. We let $V(r)$ the potential seen by each electron. Then each energy eigenfunction will satisfy the following equation:

$$H\psi_i = (T + V(r))\psi_i = E_i\psi_i \qquad (C.1)$$

Here T is the kinetic energy $(-\hbar^2\nabla^2/2m)$, and E_i is the energy of the ith state. The next step is to distinguish between the core and the valance state. The index α will be used for core and v will be used for conduction band. According to our second assumption, the core states are the same as in the isolated ion, but their energies are different, i.e. E_α, are different:

$$(T + V(r))\psi_\alpha = E_\alpha\psi_\alpha \qquad (C.2)$$

Here, the subscript α not only denotes the position of the ion as well as the energy and angular-momentum quantum numbers of the state in the equation. We have an well defined eigen value problem, apart from not knowing $V(r)$. We can approach the problem in several ways. The choice of basis function is often used physics. The plane wave basis sets is often used in band structure calculations. If we expand the Schrödinger equation C.2 with complete set of states, then we may obtain a linear simultaneous equations in the expansion coefficients. The problem of solving differential equations become a matrix diagonilizing problem. The choice of plane waves has its pros and cons. One of the difficulties of

using plane waves, is that, it requires a large number of plane waves to give a reasonable description of the wave function. Thus the solution becomes very difficult. Core electron has higher kinetic energy (s orbital) near the nucleus (see Fig. 3.2), which makes it really hard for plane wave to approximate those oscillation. Herring [1] suggested that, rather than expanding the conduction electron wave function in plane waves, a more rapidly convergent procedure is to expand in *orthogonalized* plane waves (OPWs). Hopefully, the expansions in terms of OPWs, would require fewer terms and therefore yield a easier calculation. The OPWs with wave number **k** can be defined as follows:

$$OPW_{\mathbf{k}} = e^{i\mathbf{k}.\mathbf{r}} - \sum_{\alpha} \psi_{\alpha}(\mathbf{r})\psi_{\alpha}^{*}e^{i\mathbf{k}.\mathbf{r}}d\tau' \tag{C.3}$$

An example would be sodium, where it has a ground state configuration of $1s^2 2s^2 2p^6 3s^1$, the core level would represent $1s^2 2s^2 2p^6$. For so-called simple metal (i.e. Na, Mg and Al), the convergent electron wave function is rapidly convergent in the OPW basis. Before going any further, lets check whether this OPW (C.3) is orthogonal to the core states. Lets assume an arbitrary core wave function ψ_{β} and check the orthogonality with C.3.

$$\int \psi_{\beta}^{*}(\mathbf{r}) OPW_{\mathbf{k}} d\tau' = \int \psi^{*}(\mathbf{r}) e^{i\mathbf{k}.\mathbf{r}} d\tau - \sum_{\alpha} \delta_{\alpha\beta} \int \psi^{*}(\mathbf{r}') e^{i\mathbf{k}.\mathbf{r}'} d\tau' = 0 \tag{C.4}$$

It is convenient to normalize the plane waves in the unit cell volume of the metal Ω, and we will bra and ket notation for the wave functions from now on. The plane wave becomes

$$|\mathbf{k}\rangle \equiv \Omega^{-1/2} e^{i\mathbf{k}.\mathbf{r}} \tag{C.5}$$

For core electron wave functions

$$|\alpha\rangle \equiv \psi_{\alpha}(\mathbf{r}) \tag{C.6}$$

where a bra operators is defined as $\langle\alpha| = |\alpha\rangle^*$, the other representation an integral:

$$\langle\alpha|\mathbf{k}\rangle = \Omega^{-1/2} \int \psi_\alpha^*(\mathbf{r}) e^{i\mathbf{k}.\mathbf{r}} \tag{C.7}$$

Thus the OPW equations becomes

$$OPW_\mathbf{k} = |\mathbf{k}\rangle - \sum_\alpha |\alpha\rangle\langle\alpha|\mathbf{k}\rangle \tag{C.8}$$

The projection operator P can be defined as follows:

$$P = \sum_\alpha |\alpha\rangle\langle\alpha| \tag{C.9}$$

The P operator projects any function onto core states. In terms of P operator the OPW can take following form

$$OPW_\mathbf{k} = (1 - P)|\mathbf{k}\rangle \tag{C.10}$$

Now, we can expand the conduction-band (valence electron) state in terms of the general linear combination of OPW's:

$$\psi_k = \sum_q a_q(\mathbf{k})(1 - P)|\mathbf{k} + \mathbf{q}\rangle \tag{C.11}$$

Before going a bit further, lets see how kinetic energy is represented by planewaves.

$$\langle q'| - \frac{\hbar^2}{2m}\nabla^2 |q\rangle = \frac{1}{2}\frac{\hbar^2}{2m}|\vec{q}|^2 \delta_{\vec{q}\vec{q}'} \tag{C.12}$$

In the above approximation of kinetic energy we assumed the normalizing factor is one. Now we are going to expand C.2 with OPWs, and the Schrödinger equation becomes

$$H\psi_k = \sum_q a_q(\mathbf{k})H(1 - P)|\mathbf{k} + \mathbf{q}\rangle = E_k \sum_q a_q(\mathbf{k})(1 - P)|\mathbf{k} + \mathbf{q}\rangle \tag{C.13}$$

Where , H consists both the kinetic energy and the potential. Multiplying on the left by $\langle \mathbf{k} + \mathbf{q}' |$, and using Equation (C.12) we obtain

$$a_{q'}(\mathbf{k}) \frac{\hbar^2}{2m} |\mathbf{k} + \mathbf{q}'|^2 + \sum_q a_q(\mathbf{k})$$

$$\times [\langle \mathbf{k} + \mathbf{q}' | V | \mathbf{k} + \mathbf{q} \rangle - \sum_\alpha E_\alpha \langle \mathbf{k} + \mathbf{q}' | \alpha \rangle \langle \alpha | \mathbf{k} + \mathbf{q} \rangle] = [a_{q'}(\mathbf{k}) - \sum_q a_q(\mathbf{k}) \langle \mathbf{k} + \mathbf{q}' | P | \mathbf{k} + \mathbf{q} \rangle] E_{\mathbf{k}}$$

$$(\text{C.14})$$

The above equation can be solve by diagonalizing some of matrix element. If we can evaluate some of the various matrix elements (integrals), we obtain a set of linear algebraic equation.

References

1. Conyers Herring. A new method for calculating wave functions in crystals. *Phys. Rev.*, 57(12):1169, 1940.

APPENDIX D

PROJECTOR AUGMENTED WAVE

Pseudopotential technique has been proven to be accurate for a large variety of systems, but there is no strict gurantee that it will produce the same results as an all-electron calculation. The challenge with norm-conserving pseudopotentials is that it limits the *softness*. Another way to say it, it needs higher cut-off energy. In the plane-wave basis set for the pseudo wavefunctions is defined by the shortest wave lentgh $\lambda = 2\pi/\left|\vec{G}\right|$, where $\vec{G}$ is the wave vector. Projector augmented waves (PAW) introduces projectors and auxiliary localized functions to increase the softness of the pseudopotential, at the same time keeping full wave function. In this section I will try to introduce PAW with some basic formalism. The origin of the PAW method lies a transformation that maps the true wavefunctions with their complete nodal structure into auxiliary wavefunctions. The purpose of this transformation is to have a smooth auxiliary wavefunctions, which have a rapidly convergent plane-wave expansion. The PAW method was first proposed by Blöchl in 1994 [1]. The linear transformation is as follows.

$$|\Psi_n\rangle = \hat{\mathcal{T}}\left|\tilde{\Psi}_n\right\rangle \tag{D.1}$$

Where, $|\Psi_n\rangle$ is the true all-electron KS single particle wave function, $\left|\tilde{\Psi}_n\right\rangle$ is auxiliary smooth wave function, and $\hat{\mathcal{T}}$ is a linear transformation operator. Since the true wave functions are already smooth at a certain minimum distance from the core, $\tilde{\mathcal{T}}$ should only modify the wave function close to the nuclei. Thus the transformation operator becomes

$$\tilde{\mathcal{T}} = 1 + \sum_a \tilde{\mathcal{T}}^a \tag{D.2}$$

Where a is an atom index, $\tilde{\mathcal{T}}^a$, has no effect outside a certain atom-specific augmentation region, r_C^a. Inside the augmentation spheres, the true wave function can be expanded in the partial waves ϕ_i^a, for a corresponding auxiliary smooth partial wave can be defined as $\tilde{\phi}_i^a$, and they connected by the following relation.

$$\left|\phi_i^a\right\rangle = (1 + \hat{\mathcal{T}}^a)\left|\tilde{\phi}_i^a\right\rangle \Rightarrow \hat{\mathcal{T}}^a\left|\phi_i^a\right\rangle = \left|\phi_i^a\right\rangle - \left|\tilde{\phi}_i^a\right\rangle \tag{D.3}$$

Here a is an atom index, i comes from partial waves. Outside the augmentation sphere, the partial wave and its smooth counterpart should be identical.

$$\phi_i^a(\mathbf{r}) = \tilde{\phi}_i^a(\mathbf{r}), \quad for \quad r > r_c^a \tag{D.4}$$

Where $\phi_i^a(\mathbf{r}) = \left\langle\mathbf{r}|\phi_i^a\right\rangle$, and similar for $\tilde{\phi}_i^a$. If the smooth partial waves form a complete set inside the augmentation sphere, we can expand the smooth all electron wave functions as

$$\left|\tilde{\Psi}_i^a\right\rangle = \sum_i P_{ni}^a\left|\tilde{\phi}_i^a\right\rangle, \quad |\mathbf{r} - \mathbf{R}| < r_c^a \tag{D.5}$$

Where, P_{na}^a are expansion coefficients, and need to be determined. And also, the index a stands for atomic sites, i to dintinguish different partials waves and n connected to quantum numbers (l, m). Since the transformation operator connects the smooth pseudo wave function to true wave function.

$$|\Psi_n\rangle = \hat{\mathcal{T}}\left|\tilde{\Psi}_n\right\rangle = \sum_i P_{ni}^a\left|\psi_i^a\right\rangle, \quad |\mathbf{r} - \mathbf{R}| < r_c^a \tag{D.6}$$

Something really interesting about the above equation, the true wave function has the same expansion coefficient (P_{ni}^a) as the pseudo wavefucntion. The transformation operator $\hat{\mathcal{T}}$ is required to be linear, the coefficient must be linear functionals of $\left|\tilde{\Psi}_n\right\rangle$, i.e.

$$P_{ni}^a = \left\langle\tilde{p}_i^a|\tilde{\Psi}_n\right\rangle \tag{D.7}$$

Where $\left|\tilde{p}_i^a\right\rangle$ are some fixed functions termed smooth projector functions. As there is no overlap between the augmentation spheres, we expect the smooth all electron wave function, $\left|\tilde{\Psi}_n^a\right\rangle = \sum_i \left|\tilde{\phi}_i^a\right\rangle \left\langle \tilde{p}_i^a \middle| \tilde{\Psi}_n \right\rangle$. The projectors have to be localized within an augmentation region

$$\sum_i \left|\tilde{\phi}_i^a\right\rangle\left\langle\tilde{p}_i^a\right| = 1 \tag{D.8}$$

This also implied that

$$\left\langle \tilde{p}_{i_1}^a \middle| \tilde{\phi}_{i_2}^a \right\rangle = \delta_{i_1,i_2}, \quad for \quad < r_c^a \tag{D.9}$$

the projector functions should be orthonormal to the smooth partial waves inside the augmentation sphere. The choice of projectors and partial waves can be found more detailed form original work of Blöchl [1]. Using the completeness relation from Eqn D.8

$$\hat{\mathcal{T}}^a = \sum_i \hat{\mathcal{T}}^a \left|\tilde{\phi}_i^a\right\rangle\left\langle\tilde{p}_i^a\right| = \sum_i \left(\left|\phi_i^a\right\rangle - \left|\tilde{\phi}_i^a\right\rangle\right)\left\langle\tilde{p}_i^a\right| \tag{D.10}$$

Remember, the operator $\hat{\mathcal{T}}^a$ operates only inside the sphere, outside sphere it behave like this $\left|\phi_i^a\right\rangle - \left|\tilde{\phi}_i^a\right\rangle$. Thus the total transformation operator becomes

$$\hat{\mathcal{T}} = 1 + \sum_a \sum_i \left(\left|\phi_i^a\right\rangle - \left|\tilde{\phi}_i^a\right\rangle\right)\left\langle\tilde{p}_i^a\right| \tag{D.11}$$

To summarize, we obtain the all electron KS wave function $\left|\Psi_n(\mathbf{r})\right\rangle = \left\langle\mathbf{r}|\Psi_n\right\rangle$ from the transformation

$$\Psi_n(\mathbf{r}) = \tilde{\Psi}_n(\mathbf{r}) + \sum_a \sum_i \left(\phi_i^a(\mathbf{r}) - \tilde{\phi}_i^a(\mathbf{r})\right)\left\langle\tilde{p}_i^a \middle| \tilde{\psi}_n\right\rangle \tag{D.12}$$

The equation above has three different components in the right. The first is the auxiliary wave function. The second term is the sum of partial waves, the last term is the sum of pseudo partial waves that must be subtracted inside the augmentation region. To make it a

simple KS wave function representation

$$\psi_n(\mathbf{r}) = \tilde{\psi}_n(\mathbf{r}) + \sum_a \left(\psi_n^a(\mathbf{r} - \mathbf{R}^a) - \tilde{\psi}_n^a(\mathbf{r} - \mathbf{R}^a) \right) \tag{D.13}$$

The trouble of the original KS wave functions, was that they display rapid oscillations in some of the space and smooth behavior in other parts of space. By decomposing the wave function, the achievement is that the original wave function is separated into auxiliary wave functions which are smooth everywhere.

References

1. Peter E Blöchl. Projector augmented-wave method. *Phys. Rev. B*, 50(24):17953, 1994.

APPENDIX E

PAW PSEUDOPOTENTIAL GENERATION

PAW calculation method requires a set of basis (partial-waves) and projectors functions and some additional atomic data in the so called *PAW dataset*. The PAW dataset generation is done using the following procedure.

- Solve the all-electron atomic problem in the DFT formalism using an exchange-corrleation functional (with scalar-rlativistic approximation). It is a spherical problem and usually solved in logarithmic grid.

- Separation of core and valance electron. The core density is then deduced from the core electron wave functions. For a given radius (r_{core}), the outer density is calculated so that the core density is identical to the outer.

- Choose the PAW basis (number of partial-waves and projectors).

- Generation of the pseudo partial-waves.

- Test the PAW dataset on electronic structure calculation. Repeat the procedure if necessary to satisfy the calculated property.

The atompaw input file used to generate the pseudopotential for uranium is below:

```
1  U 92
2  GGA-PBE scalarrelativistic loggridv4 700
3  7 6 6 5 0 !6s2 6p6 5f3 6d1 7s2 (from Beelar (2012), ns_max np_max
      nd_max nf_max ng_max
4  6 2 1 !6d1, only empty or partially occupied shells are entered
5  5 3 3 !5f3
6  0 0 0
7  c !1s2   1
8  c !2s2   2
9  c !3s2   3
10 c !4s2   4
11 c !5s2   5
12 v !6s2   6    1
13 v !7s2   7    2
14 c !2p6   8
15 c !3p6   9
16 c !4p6   10
17 c !5p6   11
18 v !6p6   12     3
19 c !3d10  13
20 c !4d10  14
21 c !5d10  15
22 v !6d1   16     4
23 c !4f14  17
24 v !5f3   18     5
25 3
26 2.5 2.02 1.5 1.8  !rpaw, rshape, rvloc, rcore, in a.u , changesd the
      rshape for the first time below 2.0
27 n
28 y        !one additional p partial wave
29 0.00
30 n        !no additional p partial wave
31 y        !one additional d partial wave
32 0.2      !
33 n        !no additional d partial wave
34 y        !one additional f partial wave
35 3.0
36 n        !no additional f partial wave
37 custom  rrkj besselshape     !for PWscf, UPF format needs bessels
38 4 0.0 !bessel          !l quantum number, reference energy (Ry),
      bessel for simplicity
39 1.5    !1 s       ! r_c matching radius for second s partial wave
40 1.5    !2 s       ! rc for s
41 2.5    !3 p       ! rc for p
42 2.5    !4 p       ! rc for p
43 2.5    !5 d         ! rc for d, 1.3 gives very good result
44 2.5    !6 d         ! rc for  d,  1.3 gives very good result, 4.0 energy
45 2.5    !7 f         ! rc for f
46 2.5    !8 f         ! rc for  f
47 PWSCFOUT
48 default
49 0
```

APPENDIX F

CALCULATION OF ELASTIC PARAMETERS OF

ALPHA-URANIUM

In this appendix, we will discuss the stress-strain relationships that was used to calculated the nine independent elastic constants of α-uranium. The base-centered orthorhombic phase of uranium has three lattice parameters a, b, and c, with the Bravais lattice matrix.

$$\mathbf{R} = \begin{pmatrix} \frac{a}{2} & -\frac{b}{2} & 0 \\ \frac{a}{2} & \frac{b}{2} & 0 \\ 0 & 0 & c \end{pmatrix} \tag{F.1}$$

Applying a small strain to the equilibrium lattice changes the total energy, and from this information, the elastic parameters are deduced. The elastic parameters are identified as proportional to the second order coefficient in a polynomial fit of the total energy as a function of the distortion parameter δ [1]. The distortion of lattice vector follows the rule $\mathbf{R}' = \mathbf{RD}$. Here $\mathbf{R}'$ is a matrix containing the components of the distorted lattice vectors and $\mathbf{D}$ is the symmetric distortion matrix.

The internal energy of a crystal under strain, δ, can be Taylor expanded in powers of the strain tensor with respect to initial energy of the unstrained crystal in the following way:

$$E(V, \delta) = E(V_0, 0) + V_0 \left(\sum_i \tau_i \xi_i d_1 + 1/2 \sum_{ij} c_{ij} \delta_i \xi_i \delta_j \xi_j \right) + O(\delta^3) \tag{F.2}$$

The unstrained volume is V_0, and $E(V_0, 0)$ is the energy of the unstrained system. The Voight notation has been used in the above equation, i.e. *xx, yy, zz, yz, xz* and *xy* are

replaced with 1–6. Here yz, xz and xy are equal to zy, zx and yx and for this reason ξ_i is equal to 1 for $i = 1$, 2, and 3 and 2 for $i = 4$, 5 and 6. τ_i is a component of stress tensor. The first three elastic constants c_{11}, c_{22} and c_{33} are obtained form the following distortions:

$$D_1 = \begin{pmatrix} 1+\delta & 0 & 0 \\ 0 & 1 & 0 \\ 0 & 0 & 1 \end{pmatrix} \tag{F.3}$$

$$D_2 = \begin{pmatrix} 1 & 0 & 0 \\ 0 & 1+\delta & 0 \\ 0 & 0 & 1 \end{pmatrix} \tag{F.4}$$

$$D_3 = \begin{pmatrix} 1 & 0 & 0 \\ 0 & 1 & 0 \\ 0 & 0 & 1+\delta \end{pmatrix} \tag{F.5}$$

The internal energies for these three distortions can be obtained from

$$E(V, \delta) = E(V_0, 0) + V_0 \tau_i \delta + \frac{V_0 C_{ii} \delta^2}{2} \tag{F.6}$$

The c_{44}, c_{55} and c_{66} are related to the distortion equations:

$$D_4 = \begin{pmatrix} \frac{1}{(1-\delta^2)^{1/3}} & 0 & 0 \\ 0 & \frac{1}{(1-\delta^2)^{1/3}} & \frac{\delta}{(1-\delta^2)^{1/3}} \\ 0 & \frac{\delta}{(1-\delta^2)^{1/3}} & \frac{1}{(1-\delta^2)^{1/3}} \end{pmatrix} \tag{F.7}$$

$$D_5 = \begin{pmatrix} \frac{1}{(1-\delta^2)^{1/3}} & 0 & \frac{\delta}{(1-\delta^2)^{1/3}} \\ 0 & \frac{1}{(1-\delta^2)^{1/3}} & 0 \\ \frac{\delta}{(1-\delta^2)^{1/3}} & 0 & \frac{1}{(1-\delta^2)^{1/3}} \end{pmatrix} \tag{F.8}$$

$$D_6 = \begin{pmatrix} \frac{1}{(1-\delta^2)^{1/3}} & \frac{\delta}{(1-\delta^2)^{1/3}} & 0 \\ \frac{\delta}{(1-\delta^2)^{1/3}} & \frac{1}{(1-\delta^2)^{1/3}} & 0 \\ 0 & 0 & \frac{1}{(1-\delta^2)^{1/3}} \end{pmatrix} \tag{F.9}$$

These three elastic constants can be calculated from the corresponding internal energy:

$$E(V,\delta) = E(V_0,0) + V_0\tau_i\delta + \frac{V_0 C_{ii}\delta^2}{2} \tag{F.10}$$

The last three distortions are:

$$D_7 = \begin{pmatrix} \frac{1+\delta}{(1-\delta^2)^{1/3}} & 0 & 0 \\ 0 & \frac{1-\delta}{(1-\delta^2)^{1/3}} & 0 \\ 0 & 0 & \frac{1}{(1-\delta^2)^{1/3}} \end{pmatrix} \tag{F.11}$$

$$D_8 = \begin{pmatrix} \frac{1+\delta}{(1-\delta^2)^{1/3}} & 0 & 0 \\ 0 & \frac{1}{(1-\delta^2)^{1/3}} & 0 \\ 0 & 0 & \frac{1-\delta}{(1-\delta^2)^{1/3}} \end{pmatrix} \tag{F.12}$$

$$D_9 = \begin{pmatrix} \frac{1}{(1-\delta^2)^{1/3}} & 0 & 0 \\ 0 & \frac{1+\delta}{(1-\delta^2)^{1/3}} & 0 \\ 0 & 0 & \frac{1-\delta}{(1-\delta^2)^{1/3}} \end{pmatrix} \tag{F.13}$$

The internal energies related with these three distortions are given by the following equations:

$$E(V,\delta) = E(V_0,0) + V_0\left[\tau_1 - \tau_2\right]\delta + \frac{1}{2}(c_{11} + c_{22} - 2c_{12})\delta^2 \tag{F.14}$$

$$E(V,\delta) = E(V_0,0) + V_0\left[\tau_1 - \tau_3\right]\delta + \frac{1}{2}(c_{11} + c_{33} - 2c_{13})\delta^2 \tag{F.15}$$

$$E(V,\delta) = E(V_0,0) + V_0\left[\tau_2 - \tau_3\right]\delta + \frac{1}{2}(c_{22} + c_{33} - 2c_{23})\delta^2 \tag{F.16}$$

The above equations can be used to calculated the remaining elastic constants c_{12}, c_{13}, and c_{23}. The energy and strain relations are calculated and included in Figure F.1, F.2, and F.3.

References

1. Duane C. Wallace. *Thermodynamics of Crystals*. Courier Corporation, 1998.
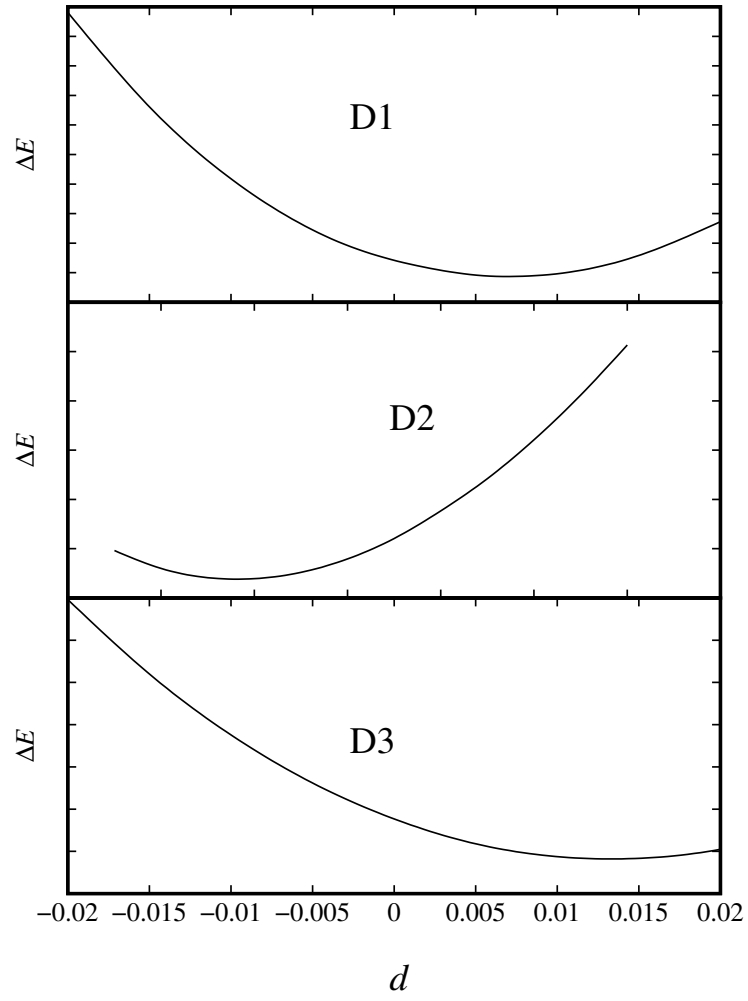
Figure F.1. Changes in the strain energy as a function of strain using distortion matrix D_1 (F.3), D_2 (F.4) and D_3 (F.5).
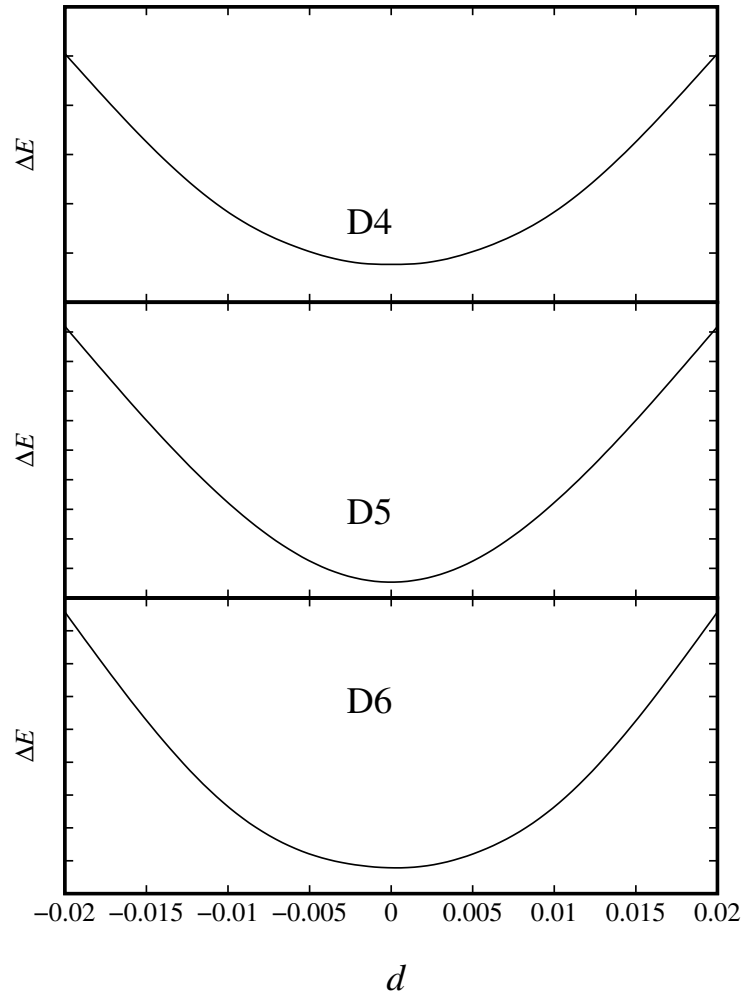
Figure F.2. Changes in the strain energy as a function of strain using distortion matrix D_4 (F.7), D_5 (F.8) and D_6 (F.9).
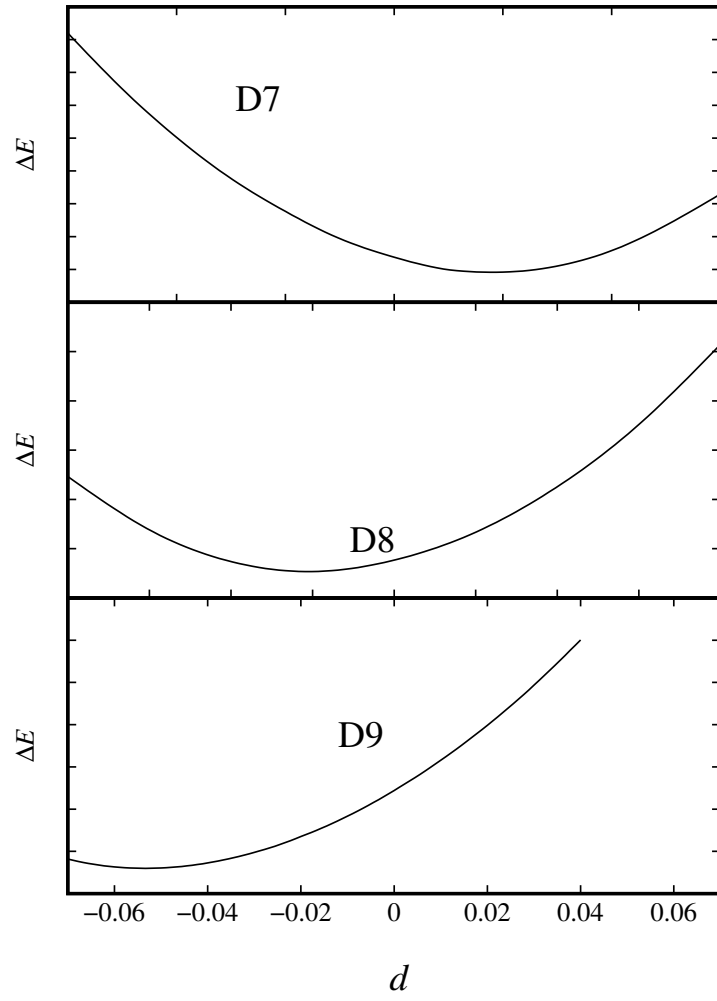
Figure F.3. Changes in the strain energy as a function of strain using distortion matrix D_7 (F.11), D_8 (F.12) and D_9 (F.13).

APPENDIX G

ELASTIC PARAMETER CALCULATION FOR BCC CRYSTAL

Applying a small strain (δ) to the equilibrium lattice changes the total energy, and from this information, the elastic parameters are deduced. The distortion of a lattice vector follows the rule $\mathbf{R}' = \mathbf{R}\mathbf{D}$. Here, $\mathbf{R}$ is the Bravais lattice vector, $\mathbf{R}'$ is a matrix containing the components of the distorted lattice vectors, and $\mathbf{D}$ is the symmetric distortion matrix.

By symmetry, there are only three independent elastic parameters for a cubic system (*i.e.*, C_{11}, C_{12}, and C_{44}). Elastic parameters are evaluated from the total energy of the crystal, to which volume-conserving orthorhombic [$C' = (C_{11} - C_{12})/2$] and monoclinic (C_{44}) distortions are applied. The relevant distortion matrices are

$$\mathbf{D}_{\text{ortho}} = \begin{bmatrix} 1 + \delta_o & 0 & 0 \\ 0 & 1 - \delta_o & 0 \\ 0 & 0 & \frac{1}{1-\delta_o^2} \end{bmatrix} \tag{G.1}$$

and

$$\mathbf{D}_{\text{mono}} = \begin{bmatrix} 1 & \delta_m & 0 \\ \delta_m & 1 & 0 \\ 0 & 0 & \frac{1}{1-\delta_m^2} \end{bmatrix}. \tag{G.2}$$

The associated total energy change for an orthorhombic distortion is

$$\Delta E = V(C_{11} - C_{12})\delta_o^2 + O(\delta_o^4). \tag{G.3}$$

For a monoclinic distortion, the energy change is

$$\Delta E = 2VC_{44}\delta_m^2 + O(\delta_m^4). \tag{G.4}$$

A sample python code to generate and run the distorted lattice in quantum espresso is shown below.

References

1. A Rafi M Iasir and Karl D Hammond. Pseudopotential for plane-wave density functional theory studies of metallic uranium. *Comput. Mater. Sci.*, 171:109221, 2020.

2. Andrea Dal Corso. Pseudopotentials periodic table: From H to Pu. *Computational Materials Science*, 95:337–350, 2014.

3. Quantum Espresso. PS library. `http://www.quantum-espresso.org/pseudopotentials`, 2019.
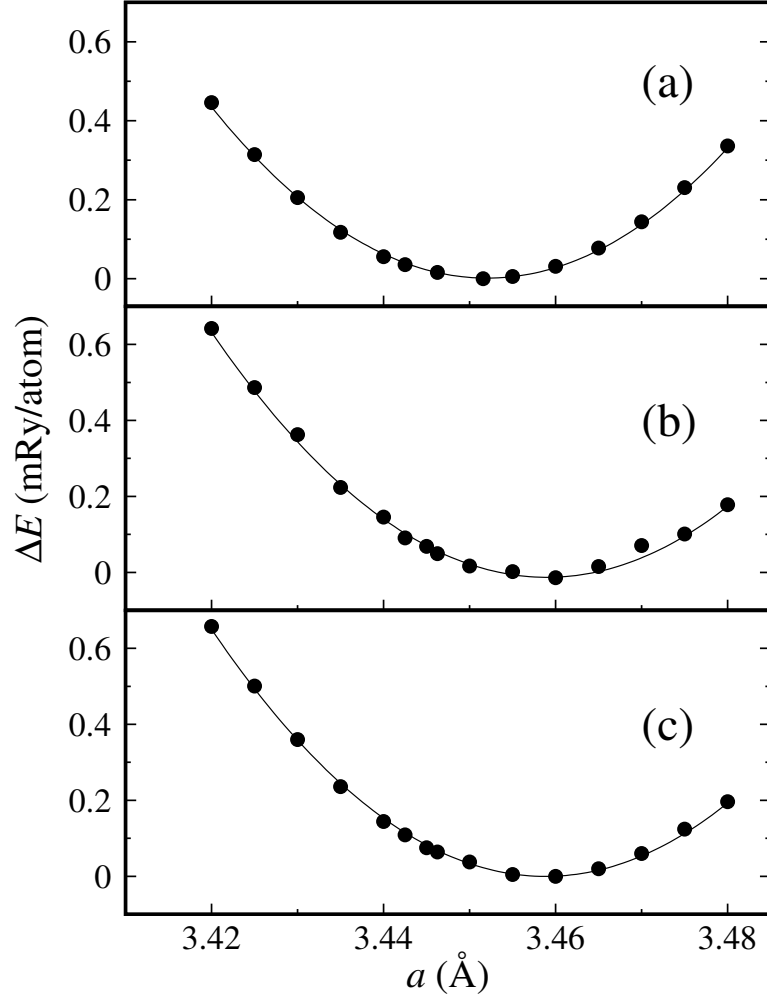
Figure G.1. Energy as a function of lattice parameters for γ-uranium. (a) Our work [1] with a *k*-point mesh of 30 × 30 × 30; (b) Pseudopotential from PS library [2, 3] with a *k*-point mesh of 30 × 30 × 30; (c) Pseudopotential from PS library [2, 3] with 42 × 42 × 42 *k*-point mesh.
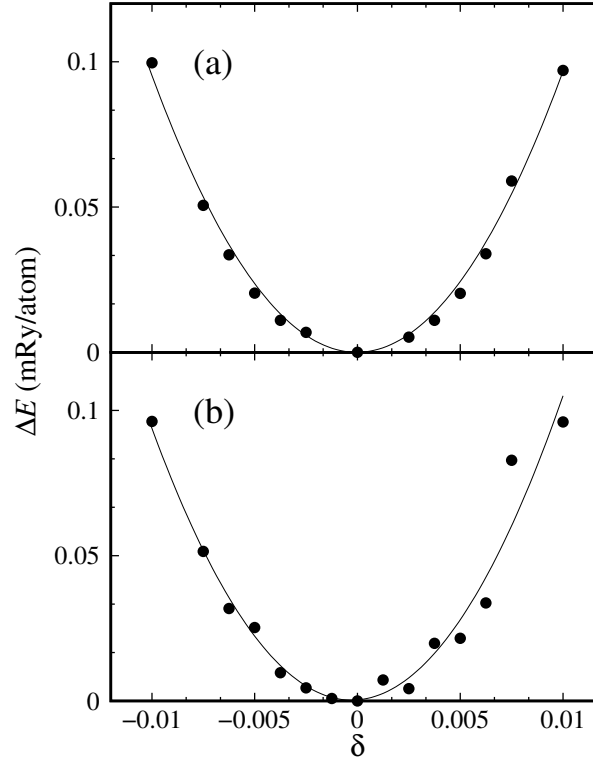
Figure G.2. Changes in the strain energy as a function of strain (δ) for monoclinic distortions of γ-uranium (Eq. (G.2) and Eq. (G.4)). (a) Our work [1]; (b) Pseudopotential from the PS library [2, 3]. Increasing the k-points does not improve the smoothness of plot (b).

```
1  import os, subprocess
2  from glob import glob
3  import re
4  import matplotlib.pyplot as plt
5  import numpy as np
6
7  def matprintf(x):
8      for i in range(len(x)):
9          print ('{:16.13f} {:16.13f} {:16.13f}'.format(x[i][0],x[i
   ][1],x[i][2]))
10
11 #d = np.array([3.42, 3.43, 3.44, 3.455, 3.45, 3.465, 3.46, 3.475,
    3.47, 3.48, 3.445, 3.4425])
12 d = np.array
      ([0,0.01,-0.01,0.005,-0.005,0.0075,-0.0075,0.00625,-0.00625,0.0025,-0.0025,0.003
13
14         # Run with different ecutwfc
15 for i in range(len(d)):
16     dd = d[i]
17     A12 = dd
18     A21 = dd
```

113
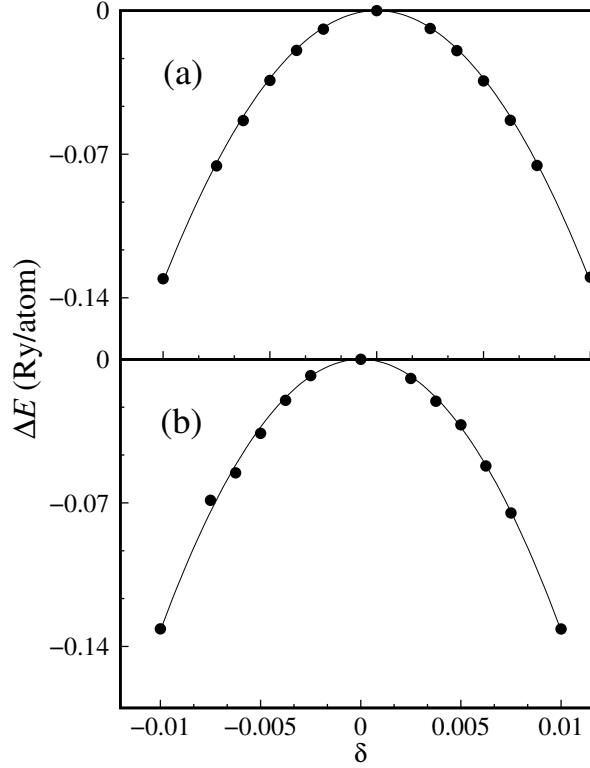
Figure G.3. Changes in the strain energy as a function of strain (δ) for orthorhombic distortions of γ-uranium (Eq. (G.1) and Eq. (G.3)). (a) Our work [1]; (b) Pseudopotential from the PS library [2, 3].

```
19    A33 = np.float128(1/((1-dd**2)))
20     #crystal axis for bcc
21    R = np.array([[-0.5,0.5,0.5],[0.5,-0.5,0.5],[0.5,0.5,-0.5]],dtype=
      np.float128)
22    #distortion matrix for monoclinic distortion
23    Dmono = np.array([[1,A12,0.0],[A21,1,0.0],[0.0,0.0,A33]],dtype=np.
      float128)
24    Rprime = np.matmul(R,Dmono)
25
26
27    filename = 'U_qepp_gamma.scf'
28    pseudo = '/home/scruffy/rafi/Desktop/rafi/quantum_espresso/
      supercell_study/pp_dir'
29    with open(filename + str(d[i]) + '.in','w') as f:
30        f.write("&control\n")
31        f.write("title = 'U_gamma'\n")
32        f.write("    calculation = 'relax'\n")
33        f.write("    restart_mode = 'from_scratch'\n")
34        f.write("    pseudo_dir = '{:s}' \n".format(pseudo))
35        f.write("    outdir = '{:s}'\n".format(pseudo))
36        f.write("    prefix = 'gammaU'\n")
37        f.write("    etot_conv_thr = 1.0e-8\n")
38        f.write("    forc_conv_thr = 1.0e-8 \n")
39        #f.write("    tstress = .true.\n")
```

```
40              #f.write("      tprnfor = .true.\n")
41      f.write("/\n")
42      f.write(" ")
43      f.write("&system\n")
44      f.write("     ibrav = 0\n")
45      f.write("         A = 3.459\n")
46      #f.write("          A = {:3.10f}\n" .format(d[i]))
47      f.write("     nat = 1\n")
48      f.write("     ntyp = 1\n")
49      f.write("     ecutwfc = 50 \n")
50      f.write("     ecutrho = 250 \n")
51      f.write("     smearing = 'methfessel-paxton'\n")
52              #f.write("     smearing = 'gauss'\n")
53              #f.write("     degauss = 0.01\n")
54      f.write("/\n")
55      f.write(" ")
56      f.write("&electrons\n")
57      f.write("     diagonalization = 'david'\n")
58              #f.write("     conv_thr = 1.0e-8\n")
59              #f.write("     mixing_beta = 0.7\n")
60      f.write("/\n")
61      f.write(" ")
62      f.write("&IONS\n")
63      f.write("/\n")
64      f.write(" ")
65      f.write("&CELL\n")
66      f.write("/\n")
67      f.write("CELL_PARAMETERS {alat} \n")
68      #f.write("  -0.5    0.5    0.5 \n")
69      #f.write("   0.5   -0.5    0.5 \n")
70      #f.write("   0.5    0.5   -0.5 \n")
71
72      for j in range (len(Rprime)) :
73              f.write ('{:16.13f} {:16.13f} {:16.13f} \n'.format(
    Rprime[j][0],Rprime[j][1],Rprime[j][2]))
74
75      f.write(" \n")
76      f.write("ATOMIC_SPECIES\n")
77      f.write("U 238.029  U.GGA-PBE-paw.UPF\n")
78      f.write(" \n")
79      f.write("ATOMIC_POSITIONS {crystal}\n")
80      f.write("U  0.000  0.000 0.000\n")
81      f.write(" \n")
82      f.write("K_POINTS automatic\n")
83      f.write("35 35 35 0 0 0\n")
84  command = ('mpiexec -n 8 pw.x -i ' + filename + str(d[i]) + '.in >
    ' + filename + str(d[i]) + '.out' )
85  print(command)
86  p = subprocess.Popen(command, shell=True)
87  p.wait()
```

APPENDIX H

FINITE ELEMENT METHOD IN MOOSE

Divergence theorem transforms and volume integral into a surface integral:

$$\int_{\Omega} \nabla \cdot \vec{\mathbf{g}} \, dx = \int_{\partial\Omega} \vec{\mathbf{g}} \cdot \hat{n} \, ds \tag{H.1}$$

The strong form of the diffusion equation without a source term is as follows:

$$\nabla \cdot (K(T)\nabla T) = 0$$

Multiplying by a test function ($\mathcal{T}_f$), and integrating over the domain Ω:

$$\int_{\Omega} \mathcal{T}_f (\nabla \cdot \underbrace{K(T)\nabla T}_{\mathcal{G}}) = 0$$

$$\int_{\Omega} \mathcal{T}_f \nabla \cdot \mathcal{G} = 0$$

$$\int_{\Omega} \nabla \cdot (\mathcal{T}_f \mathcal{G}) - \int_{\Omega} \nabla \mathcal{T}_f \cdot \mathcal{G} = 0$$

Using the divergence theorem (H.1) the above equation becomes:

$$\int_{\partial\Omega} \mathcal{T}_f \mathcal{G} \cdot \hat{n} \, ds - \int_{\Omega} \nabla \mathcal{T}_f \cdot \mathcal{G} dx = 0$$

$$\int_{\Omega} \nabla \mathcal{T}_f \cdot K(T)\nabla T dx - \int_{\partial\Omega} \mathcal{T}_f K(T)\nabla T \cdot \hat{n} \, ds = 0$$

Using the inner product notation the above equation can be written as follows:

$$(\nabla \mathcal{T}_f, K\nabla T) - \langle \mathcal{T}_f, K\nabla T \cdot \hat{n} \rangle = 0 \tag{H.2}$$

Each of these term inherits an existing MOOSE type to solve the problem.

$$\underbrace{(\nabla \mathcal{T}_f, K\nabla T)}_{Kernel} - \underbrace{\langle \mathcal{T}_f, K\nabla T \cdot \hat{n} \rangle}_{BoundaryCondition} = 0 \tag{H.3}$$

APPENDIX I

INPUT FILES

Input files for different software are included in this chapter. Because of the complexity and number, I have included samples of them.

I.1 MOOSE Framework

This is the `main.C` file for moose simulation. Depends on the problem, moose requires a number of header files and source file.

```
1   /* this is a main app file created for the purpose of simulating
     heat conduction
2    *       This is file is created by Rafi, Sepetember 27, 2016
3    *       **************************************************   */
4
5   #include "HeatCondRafiApp.h"
6   #include "MooseInit.h"
7   #include "Moose.h"
8   #include "MooseApp.h"
9   #include "AppFactory.h"
10
11  // Creat a performance log
12  PerfLog Moose::perf_log("HeatCondRafi");
13
14  //Begin the main problem.
15  int main(int argc, char *argv[])
16  {
17      // Initialize MPI, solvers and MOOSE
18      MooseInit init(argc, argv);
19
20      // Register this application's MooseApp and any it depends on
21      HeatCondRafiApp::registerApps();
22
23      // This creates dynamic memory that we're responsible for
    deleting
24      //MooseApp * app =  AppFactory::createAppShared("HeatCondRafiApp
    ", argc, argv);
25       std::shared_ptr<MooseApp> app = AppFactory::createAppShared("
    HeatCondRafiApp", argc, argv);
26
27      //Execute the application
```

```
28      app->run();
29
30      // Free up the memory we created earlier
31      //delete app;
32
33      return 0;
34  }
```

This is a sample of source file (kernel in MOOSE) of heat transfer in U–10Mo

```cpp
// this file is edited by rafi fro temperature dependent thermal
    conductivity
#include "Tempdepk.h"

template<>
InputParameters validParams<Tempdepk>()
{
  InputParameters params = validParams<Diffusion>();
  params.addClassDescription("This will solve heat diffusion with
    temperature dependent thermal conductivity");
  return params;
}

Tempdepk::Tempdepk(const InputParameters & parameters) :
    Diffusion(parameters),
  _thermal_conductivity(getMaterialProperty<Real>("
    thermal_conductivity"))  /*be sure u use the "thermal_conductivity,
     otherwise it will
not read the thermal_conductivity from the input*/
{
}

Real
Tempdepk::computeQpResidual()
{
  //return _grad_u[_qp] * _grad_test[_i][_qp];
  //Real _k=0.606+0.0351*_u[_qp]; // from D.E. Burkes et al./ Journal
    of Nuc Material 2010

  return _thermal_conductivity[_qp]*Diffusion::computeQpResidual();
}

Real
Tempdepk::computeQpJacobian()
{
  //Real _k=0.606+0.0351*_u[_qp];
  //return _grad_phi[_j][_qp] * _grad_test[_i][_qp];

  return _thermal_conductivity[_qp]*Diffusion::computeQpJacobian();
}
```

```
1  // this file is edited by rafi fro temperature dependent thermal
       conductivity
2  #include "TXenon.h"
3
4
5  template<>
6  InputParameters validParams<TXenon>()
7  {
8    InputParameters params = validParams<Diffusion>();
9    params.addClassDescription("This will solve heat diffusion with
       temperature dependent thermal conductivity");
10   return params;
11 }
12
13 TXenon::TXenon(const InputParameters & parameters) :
14     Diffusion(parameters),
15   _thermal_conductivity(getMaterialProperty<Real>("
      thermal_conductivity"))  /*be sure u use the "thermal_conductivity,
       otherwise it will
16 not read the thermal_conductivity from the input*/
17 {
18 }
19
20 Real
21 TXenon::computeQpResidual()
22 {
23   //return _grad_u[_qp] * _grad_test[_i][_qp];
24   //Real _k=0.606+0.0351*_u[_qp]; // from D.E. Burkes et al./ Journal
      of Nuc Material 2010
25
26 /* return _thermal_conductivity[_qp]*Diffusion::computeQpResidual() +
      380E3*_test[_i][_qp]; */
27
28 // the above one for a constant forcing function
29
30   return _thermal_conductivity[_qp]*Diffusion::computeQpResidual();
31 }
32
33 Real
34 TXenon::computeQpJacobian()
35 {
36   //Real _k=0.606+0.0351*_u[_qp];
37   //return _grad_phi[_j][_qp] * _grad_test[_i][_qp];
38
39   return _thermal_conductivity[_qp]*Diffusion::computeQpJacobian() +
40   (-2*4.72984E-09*_u[_qp]*2.+2.0891E-5)*_grad_u[_qp]*_grad_test[_i][
      _qp];
41 }
```

Material source code for U–10Mo property.

```
1  // this file is edited by Rafi January 24, 2017
2  //
3  #include "Tconductivity.h"
4
5  template<>
6  InputParameters validParams<Tconductivity>()
7  {
8    InputParameters params = validParams<Material>();
9  // we do not need to add any data from the input file
10   params.addClassDescription("This is to calculate the temperature
       dependent thermal conductivity of U-10Mo");
11 // the "temperature" variable has to be defined in the input files
12   params.addCoupledVar("dep_variable", "The thermal conductivity is
       calculated from temperature");
13   return params;
14 }
15
16 Tconductivity::Tconductivity(const InputParameters & parameters) :
17     Material(parameters),
18
19     // Declare  material properties.  This returns references that we
20     // hold onto as member variables
21     //_permeability(declareProperty<Real>("permeability")),
22   _thermal_conductivity(declareProperty<Real>("thermal_conductivity"))
     ,
23   //_dep_variable(isCoupled("dep_varible"))
24   _dep_variable(coupledValue("dep_variable"))
25 {
26 }
27
28 void
29 Tconductivity::computeQpProperties()
30 {
31
32   // Sample the LinearInterpolation object to get the permeability for
       the ball size
33   //_permeability[_qp] = _permeability_interpolation.sample(
       _ball_radius);
34   _thermal_conductivity[_qp]=0.606+0.0351*_dep_variable[_qp];
35 }
```

Source file for xenon material property.

```
1  // this file is edited by Rafi February 13, 2017
2  //
3  #include "XenonT.h"
4
5  template<>
6  InputParameters validParams<XenonT>()
7  {
8    InputParameters params = validParams<Material>();
9  // we do not need to add any data from the input file
10   params.addClassDescription("This is to calculate the temperature
       dependent  thermal conductivity of Xenon");
11 // the "temperature" variable has to be defined in the input files
12   params.addCoupledVar("dep_variable", "The thermal conductivity is
       calculated from temperature");
13   return params;
14 }
15
16
17 XenonT::XenonT(const InputParameters & parameters) :
18     Material(parameters),
19
20     // Declare  material properties.  This returns references that we
21     // hold onto as member variables
22     //_permeability(declareProperty<Real>("permeability")),
23   _thermal_conductivity(declareProperty<Real>("thermal_conductivity"))
       ,
24   //_dep_variable(isCoupled("dep_varible"))
25   _dep_variable(coupledValue("dep_variable"))
26 {
27 }
28
29 void
30 XenonT::computeQpProperties()
31 {
32
33   // Sample the LinearInterpolation object to get the permeability for
       the ball size
34   //_permeability[_qp] = _permeability_interpolation.sample(
       _ball_radius);
35   //_thermal_conductivity[_qp]=0.000000001+0.00000000001*_dep_variable
       [_qp];
36   /*abobe correlation is wrong, is calculated wrong, the next equation
       is calcuated from Robinovich et al. Thermophy
37   sical property of Neon, Argon, Krypton, and Xenon */
38
39   _thermal_conductivity[_qp]=-4.72984E-09*_dep_variable[_qp]*
       _dep_variable[_qp] + 2.0891E-5*_dep_variable[_qp]+ 2.83137E-05 ;
40
41
42 }
```

Source file for heat flux calculation.

```
1
2  #include "HeatFlux.h"
3
4  template<>
5  InputParameters validParams<HeatFlux>()
6  {
7    InputParameters params = validParams<AuxKernel>();
8
9    MooseEnum component("x y z");
10   // Declare the options for a MooseEnum.
11   // These options will be presented to the user in Peacock
12   // and if something other than these options is in the input file
13   // an error will be printed
14   params.addClassDescription("This is to calculate the heat flux for
       over all material");
15   // Add a "coupling paramater" to get a variable from the input file.
16   params.addRequiredCoupledVar("field_temperature", "The temperature
       field.");
17   params.addRequiredParam<MooseEnum>("component", component, "The
       desired component of temperature");
18
19   return params;
20 }
21
22 HeatFlux::HeatFlux(const InputParameters & parameters) :
23     AuxKernel(parameters),
24
25     // Get the gradient of the variable
26     _temperature_gradient(coupledGradient("field_temperature")),
27
28     // Snag thermal_coductivity from the Material system.
29     // Only AuxKernels operating on Elemental Auxiliary Variables can
       do this
30     _t_thermal_conductivity(getMaterialProperty<Real>("
       thermal_conductivity")),
31   _component(getParam<MooseEnum>("component"))
32
33 {
34 }
35
36 Real
37 HeatFlux::computeValue()
38 {
39   // Access the gradient of the pressure at this quadrature point
40   // Then pull out the "component" of it we are looking for (x, y or z
       )
41   // Note that getting a particular component of a gradient is done
       using the
42   // parenthesis operator
43   return _t_thermal_conductivity[_qp]*_temperature_gradient[_qp](
       _component);
44 }
```

This source file is to calculate the gradient of the temperature.

```
1
2  #include "TGradient.h"
3
```

```
4  template<>
5  InputParameters validParams<TGradient>()
6  {
7    InputParameters params = validParams<AuxKernel>();
8
9    // Declare the options for a MooseEnum.
10   // These options will be presented to the user in Peacock
11   // and if something other than these options is in the input file
12   // an error will be printed
13   params.addClassDescription("This is to calculate the temperature
       gradient for over all material");
14   // Add a "coupling paramater" to get a variable from the input file.
15   //params.addRequiredCoupledVar("field_temperature", "The temperature
        field.");
16   MooseEnum component("x y z");
17
18   // Use the MooseEnum to add a parameter called "component"
19   params.addRequiredCoupledVar("field_temperature", "The Temperature
       field");
20   params.addRequiredParam<MooseEnum>("component", component, "The
       desired component of velocity.");
21   return params;
22 }
23
24 TGradient::TGradient(const InputParameters & parameters) :
25     AuxKernel(parameters),
26
27     // Get the gradient of the variable
28     _temperature_gradient(coupledGradient("field_temperature")),
29
30   _component(getParam<MooseEnum>("component"))
31     // Snag thermal_coductivity from the Material system.
32     // Only AuxKernels operating on Elemental Auxiliary Variables can
     do this
33     //_t_thermal_conductivity(getMaterialProperty<Real>("
     thermal_conductivity"))
34
35 {
36 }
37
38 Real
39 TGradient::computeValue()
40 {
41   // Access the gradient of the pressure at this quadrature point
42   // Then pull out the "component" of it we are looking for (x, y or z
       )
43   // Note that getting a particular component of a gradient is done
     using the
44   // parenthesis operator
45   return _temperature_gradient[_qp](_component);
46 }
```

For every source file, we need header files. The required header files are below. `Tempdepk.h`

```cpp
// this file created by Rafi, January 24, 2017
#ifndef TEMPDEPK_H
#define TEMPDEPK_H
#include "Diffusion.h"
class Tempdepk;
template<>
InputParameters validParams<Tempdepk>();

/**
 * This kernel will solve a temperature dependent thermal conductivity
     with diffusion of temperature
 */
class Tempdepk : public Diffusion
{
public:
  Tempdepk(const InputParameters & parameters);
protected:
  virtual Real computeQpResidual() override;
  virtual Real computeQpJacobian() override;
// creating a moose array for material property
  const MaterialProperty<Real> & _thermal_conductivity;
};
#endif
```

TXenon.h

```cpp
1  / this file created by Rafi, January 24, 2017
2  #ifndef TXENON_H
3  #define TXENON_H
4
5  #include "Diffusion.h"
6
7  class TXenon;
8  template<>
9  InputParameters validParams<TXenon>();
10
11 /**
12  * This kernel will solve a temperature dependent thermal conductivity
       with diffusion of temperature
13  */
14 class TXenon : public Diffusion
15 {
16 public:
17   TXenon(const InputParameters & parameters);
18
19 protected:
20   virtual Real computeQpResidual() override;
21
22   virtual Real computeQpJacobian() override;
23 // creating a moose array for material property
24
25  const MaterialProperty<Real> & _thermal_conductivity;
26 };
27 #endif
```

```cpp
1  // this file is created by Rafi at February 13, 2017
2
3  #ifndef TCONDUCTIVITY_H
4  #define TCONDUCTIVITY_H
5
6  #include "Material.h"
7
8  class Tconductivity;
9
10 template<>
11 InputParameters validParams<Tconductivity>();
12
13 /**
14  * Material objects inherit from Material and override
15     computeQpProperties.
16  *
17  * Their job is to declare properties for use by other objects in the
18  * calculation such as Kernels and BoundaryConditions.
19  */
20 class Tconductivity : public Material
21 {
22 public:
23   Tconductivity(const InputParameters & parameters);
24
25 protected:
26   /**
27    * Necessary override.  This is where the values of the properties
28    * are computed.
29    */
30   virtual void computeQpProperties() override;
31
32 private:
33     // The thermal conductivity
34   MaterialProperty<Real> & _thermal_conductivity; // for u-10 Mo
35
36   // const VariableGradient & _dep_variable; // this will get the
37     temperature
38   //std::vector<const VariableValue> & _dep_variable;
39   //VariableValue<Real> & _dep_variable;
40     const VariableValue & _dep_variable;
41 };
42 #endif //Tconductivity
```

```cpp
// this file is created by Rafi at February 13, 2017

#ifndef TCONDUCTIVITY_H
#define TCONDUCTIVITY_H

#include "Material.h"

class Tconductivity;

template<>
InputParameters validParams<Tconductivity>();

/**
 * Material objects inherit from Material and override
    computeQpProperties.
 *
 * Their job is to declare properties for use by other objects in the
 * calculation such as Kernels and BoundaryConditions.
 */
class Tconductivity : public Material
{
public:
  Tconductivity(const InputParameters & parameters);

protected:
  /**
   * Necessary override.  This is where the values of the properties
   * are computed.
   */
  virtual void computeQpProperties() override;

private:
    // The thermal conductivity
  MaterialProperty<Real> & _thermal_conductivity; // for u-10 Mo

  // const VariableGradient & _dep_variable; // this will get the
    temperature
  //std::vector<const VariableValue> & _dep_variable;
  //VariableValue<Real> & _dep_variable;
    const VariableValue & _dep_variable;
};
#endif //Tconductivity
```

XenonT.h

```cpp
1  / this file is created by Rafi at February 13, 2017
2  // The reference is Rabinovich et al.
3  // Thermophysical Propeties of Neon, Argon, Krypton and Xenon// for
        the purpose of temperature dependent thermal condcutivity for U-10
        Mo
4  #ifndef XENONT_H
5  #define XENONT_H
6
7  #include "Material.h"
8  class XenonT;
9
10 template<>
11 InputParameters validParams<XenonT>();
12
13 /**
14  * Material objects inherit from Material and override
        computeQpProperties.
15  *
16  * Their job is to declare properties for use by other objects in the
17  * calculation such as Kernels and BoundaryConditions.
18  */
19 class XenonT : public Material
20 {
21 public:
22   XenonT(const InputParameters & parameters);
23
24 protected:
25   /**
26    * Necessary override.  This is where the values of the properties
27    * are computed.
28    */
29   virtual void computeQpProperties() override;
30 private:
31
32     // The thermal conductivity
33   MaterialProperty<Real> & _thermal_conductivity; // for u-10 Mo
34
35   // const VariableGradient & _dep_variable; // this will get the
        temperature
36   //std::vector<const VariableValue> & _dep_variable;
37   //VariableValue<Real> & _dep_variable;
38     const VariableValue & _dep_variable;
39 };
40
41 #endif //XENONT_H
```

129

HeatFlux.h

```
1  ifndef HEATFLUX_H
2  #define HEATFLUX_H
3
4  #include "AuxKernel.h"
5
6  //Forward Declarations
7  class HeatFlux;
8
9  template<>
10 InputParameters validParams<HeatFlux>();
11
12 /**
13  * Constant auxiliary value
14  */
15 class HeatFlux : public AuxKernel
16 {
17 public:
18   HeatFlux(const InputParameters & parameters);
19
20   virtual ~HeatFlux() {}
21
22 protected:
23   /**
24    * AuxKernels MUST override computeValue.  computeValue() is called
     on
25    * every quadrature point.  For Nodal Auxiliary variables those
     quadrature
26    * points coincide with the nodes.
27    */
28   virtual Real computeValue() override;
29
30
31   /// The gradient of a coupled variable
32   const VariableGradient & _temperature_gradient;
33
34   /// Holds the permeability and viscosity from the material system
35   const MaterialProperty<Real> & _t_thermal_conductivity;
36   // const MaterialProperty<Real> & _viscosity;
37
38     int _component;
39 };
40 #endif // end of HEATFLUX_H
```

TGradient.h

```
1  ifndef TGRADIENT_H
2  #define TGRADIENT_H
3
4  #include "AuxKernel.h"
5
6  //Forward Declarations
7  class TGradient;
8
9  template<>
10 InputParameters validParams<TGradient>();
11
12 /**
13  * Constant auxiliary value
14  */
15 class TGradient : public AuxKernel
16 {
17 public:
18   TGradient(const InputParameters & parameters);
19
20   virtual ~TGradient() {}
21
22 protected:
23   /**
24    * AuxKernels MUST override computeValue.  computeValue() is called
       on
25    * every quadrature point.  For Nodal Auxiliary variables those
       quadrature
26    * points coincide with the nodes.
27    */
28   virtual Real computeValue() override;
29
30
31   /// The gradient of a coupled variable
32   const VariableGradient & _temperature_gradient;
33
34   /// Holds the permeability and viscosity from the material system
35   //const MaterialProperty<Real> & _t_thermal_conductivity;
36   int _component;
37   // const MaterialProperty<Real> & _viscosity;
38 };
39
40 #endif // end of TGRADIENT_H
```

131

I.2 ATOMPAW

This is an input file for Atompaw to generate the paw database for electronic structure calculation.

```
1  U 92
2  GGA-PBE scalarrelativistic loggridv4 700
3  7 6 6 5 0
4  6 2 1
5  5 3 3
6  0 0 0
7  c    !1s2    1
8  c    !2s2    2
9  c    !3s2    3
10 c    !4s2    4
11 c    !5s2    5
12 v    !6s2    6        1
13 v    !7s2    7        2
14 c    !2p6    8
15 c    !3p6    9
16 c    !4p6    10
17 c    !5p6    11
18 v    !6p6    12       3
19 c    !3d10   13
20 c    !4d10   14
21 c    !5d10   15
22 v    !6d1    16       4
23 c    !4f14   17
24 v    !5f3    18       5
25 3
26 2.5 2.02 1.5 1.8    !rpaw, rshape, rvloc, rcore, in a.u
27 n
28 y                !one additional p partial wave
29 0.00
30 n                !no additional p partial wave
31 y                !one additional d partial wave
32 0.2              !
33 n                !no additional d partial wave
34 y                !one additional f partial wave
35 3.0
36 n                !no additional f partial wave
37 custom  rrkj besselshape    !UPF format needs bessels
38 4 0.0 !bessel              !l quantum number, reference energy (Ry),
      bessel for simplicity
39 1.3     !1 s             ! rc s partial wave
40 1.3     !2 s             ! rc for s
41 2.5     !3 p             ! rc for p
42 2.5     !4 p             ! rc for p
43 1.55    !5 d             ! rc for d, 1.3 gives very good result
44 1.55    !6 d        ! rc for  d,    1.3 gives very good result, 4.0
      energy
45 2.5     !7 f        ! rc for f
46 2.5     !8 f        ! rc for  f
47 PWSCFOUT
48 default
49 0
```

I.3 DFT Calculation

I.3.1 SCF of a primitive cell

This is sample input file to calculate the self consistent field study using Quantum Espresso. It contains the lattice parameter of α-uranium.

```
1  &CONTROL
2                          title = 'alphaU'
3                    calculation = 'scf'
4                   restart_mode = 'from_scratch'
5                         outdir = '/home/iasir/quantum_espresso/
       Uranium_PAW/rvloc_96/y_value_plot/lat01'
6                      pseudo_dir = '/home/iasir/quantum_espresso/
       Uranium_PAW/rvloc_96/y_value_plot/lat01'
7                         prefix = 'alphaU'
8                      verbosity = 'default'
9                        tstress = .true.
10                       tprnfor = .true.
11 /
12 &SYSTEM
13                         ibrav = 0
14                             A = 2.8383
15                            at = 2
16                          ntyp = 1
17                          ntyp = 1
18                        ecutwfc = 50
19                        ecutrho = 250
20                       smearing = 'methfessel-paxton'
21 /
22 &ELECTRONS
23             diagonalization = 'david'
24 /
25 &IONS
26
27  /
28 CELL_PARAMETERS {alat}
29   0.500000000000000   -1.031658697792153    0.000000000000000
30   0.500000000000000    1.031658697792153    0.000000000000000
31   0.000000000000000    0.000000000000000    1.73379271551118
32 ATOMIC_SPECIES
33     U   238.0290000000   U.GGA-PBE-paw.UPF
34
35 ATOMIC_POSITIONS {crystal}
36 U    0.0986000000000000   -0.0986000000000000   -0.250000000000000
37 U   -0.0986000000000000    0.0986000000000000    0.250000000000000
38
39 K_POINTS automatic
40 20   20   26    0 0 0
```

I.3.2 Supercell of uranium

The following input is for performing a relax calcuation using supercell of γ-uranium with molybdenum and xenon.

```
1  &CONTROL
2                                 title  = 'supercellgammaU'
3                           calculation = 'relax'
4                          restart_mode = 'from_scratch'
5                      outdir = '/group/hammond/sysyphus/3x3/2prim-2
       nd/im02',
6                        pseudo_dir = '/group/hammond/sysyphus/
       pp_dir',
7                           prefix = 'supercell_gammaU'
8                     etot_conv_thr = 1.0D-6
9                     forc_conv_thr = 1.0D-6
10                       verbosity = 'default'
11                        tstress = .true.
12                        tprnfor = .true.
13                         nstep  = 200
14 /
15 &SYSTEM
16                              ibrav = 0
17                                  A = 10.35
18                                nat = 53
19                                ntyp = 3
20                             ecutwfc = 50
21                             ecutrho = 260
22                          occupations = 'smearing'
23                             degauss = 0.02
24                            smearing = 'mp'
25 /
26 &ELECTRONS
27             diagonalization = 'david'
28          electron_maxstep  = 900
29                 mixing_beta = 0.1
30 /
31 &IONS
32
33 /
34 &CELL
35
36 /
37 CELL_PARAMETERS {alat}
38  1.00    0.00      0.00
39  0.00    1.00      0.00
40  0.00    0.00      1.00
41
42 ATOMIC_SPECIES
43    U  238.02800    U.GGA-PBE-paw.UPF
44    Xe 131.29       Xe.GGA-PBE-paw.UPF
45    Mo 95.94        Mo.GGA-PBE-paw.UPF
46
47 ATOMIC_POSITIONS (crystal)
48 U       0.000000000    0.000000000    0.000000000    0   0   0
49 U       0.210984461    0.204688901    0.229195736
50 U       0.000000000    0.000000000    0.333333333    0   0   0
51 U       0.000000000    0.000000000    0.666666667    0   0   0
52 U       0.333333333    0.000000000    0.000000000    0   0   0
```

53	U	0.666666667	0.000000000	0.000000000	0	0	0
54	U	0.000000000	0.333333333	0.000000000	0	0	0
55	U	0.000000000	0.666666667	0.000000000	0	0	0
56	U	0.137231091	0.153757182	0.530873483			
57	U	0.174376372	0.129124170	0.859923969			
58	U	0.526508957	0.134953713	0.159596399			
59	U	0.862089662	0.133706169	0.175813941			
60	U	0.158683128	0.524614679	0.202129442			
61	U	0.148170903	0.848856345	0.127554382			
62	U	0.000000000	0.333333333	0.333333333	0	0	0
63	U	0.000000000	0.666666667	0.666666667	0	0	0
64	U	0.000000000	0.666666667	0.333333333	0	0	0
65	U	0.000000000	0.333333333	0.666666667	0	0	0
66	U	0.333333333	0.000000000	0.333333333	0	0	0
67	U	0.666666667	0.000000000	0.666666667	0	0	0
68	U	0.333333333	0.000000000	0.666666667	0	0	0
69	U	0.666666667	0.000000000	0.333333333	0	0	0
70	U	0.333333333	0.333333333	0.000000000	0	0	0
71	U	0.666666667	0.666666667	0.000000000	0	0	0
72	U	0.666666667	0.333333333	0.000000000	0	0	0
73	U	0.333333333	0.666666667	0.000000000	0	0	0
74	U	0.137231091	0.153757182	0.530873483			
75	U	0.174376372	0.129124170	0.859923969			
76	U	0.526508957	0.134953713	0.159596399			
77	U	0.862089662	0.133706169	0.175813941			
78	U	0.158683128	0.524614679	0.202129442			
79	U	0.148170903	0.848856345	0.127554382			
80	U	0.000000000	0.333333333	0.333333333	0	0	0
81	U	0.000000000	0.666666667	0.666666667	0	0	0
82	U	0.000000000	0.666666667	0.333333333	0	0	0
83	U	0.000000000	0.333333333	0.666666667	0	0	0
84	U	0.333333333	0.000000000	0.333333333	0	0	0
85	U	0.666666667	0.000000000	0.666666667	0	0	0
86	U	0.333333333	0.000000000	0.666666667	0	0	0
87	U	0.666666667	0.000000000	0.333333333	0	0	0
88	U	0.333333333	0.333333333	0.000000000	0	0	0
89	U	0.666666667	0.666666667	0.000000000	0	0	0
90	U	0.666666667	0.333333333	0.000000000	0	0	0
91	U	0.333333333	0.666666667	0.000000000	0	0	0
92	U	0.179014193	0.490220525	0.515819257			
93	U	0.211529991	0.769018260	0.787411348			
94	U	0.174791835	0.807115343	0.456517964			
95	U	0.138750516	0.465098823	0.842421942			
96	U	0.460277126	0.148072446	0.492479910			
97	U	0.853185555	0.205057669	0.814927365			
98	U	0.517574914	0.155283842	0.808674767			
99	U	0.797006954	0.141631469	0.505322942			
100	U	0.472193561	0.445111610	0.164972643			
101	U	0.797427656	0.818792499	0.205498630			
102	U	0.849105689	0.447077449	0.157067159			
103	U	0.477316581	0.824076376	0.198019584			
104	U	0.357811109	0.358247142	0.377740929			
105	Mo	0.317120589	0.314631326	0.680448732			
106	Mo	0.607263578	0.351682511	0.642824966			
107	U	0.340594168	0.659454747	0.325699754			
108	U	0.361075015	0.621507036	0.637398808			
109	Mo	0.660724290	0.302342735	0.343336983			
110	U	0.864625684	0.823864687	0.866239386			
111	U	0.857300550	0.828682348	0.537389462			
112	U	0.459239378	0.501675726	0.851462699			

```
113 U          0.787353995    0.504077862    0.849782744
114 U          0.483651729    0.821500104    0.546062842
115 U          0.525967152    0.834454416    0.872311707
116 U          0.803327765    0.439115905    0.558594712
117 U          0.678734725    0.684452016    0.648081893
118 Xe         0.649495337    0.596675850    0.354354426
119
120
121
122 !Xe     0.500000000         0.500000000         0.500000000
123
124 K_POINTS automatic
125 4 4 4        0 0 0
```

I.3.3 Nudged Elastic Band Calculation

The following input file is to perform nudged elastic band calculation using Quantum Espresso.

```
1  BEGIN
2  BEGIN_PATH_INPUT
3  &PATH
4    restart_mode       = 'from_scratch',
5    string_method      = 'neb',
6    nstep_path         = 100,
7    ds                 = 1.00,
8    opt_scheme         = "broyden",
9    num_of_images      = 5,
10   k_max              = 0.6169D0,
11   k_min              = 0.6169D0,
12   CI_scheme          = "auto",
13   path_thr           = 0.1D0,
14 /
15 END_PATH_INPUT
16 BEGIN_ENGINE_INPUT
17 &CONTROL
18  outdir = '/group/hammond/sysyphus/3x3/2prim-2nd/neb',
19  pseudo_dir = '/group/hammond/sysyphus/pp_dir',
20  prefix = 'xe01neb' ,
21  verbosity = 'high' ,
22  etot_conv_thr = 1e-6 ,
23  forc_conv_thr = 1e-5 ,
24  nstep = 200 ,
25  tstress = .true.,
26  tprnfor = .true.,
27  max_seconds = 1.0D+18,
28 /
29 &SYSTEM
30                        ibrav = 0,
31                            A = 10.35,
32                          nat = 53,
33                         ntyp = 3,
34                       ecutwfc = 50,
35                       ecutrho = 260,
36                   occupations = 'smearing',
37                       degauss = 0.02,
38                      smearing = 'mp',
39 /
40 &ELECTRONS
41           electron_maxstep = 900,
42                   conv_thr = 1e-7 ,
43               mixing_beta = 0.1 ,
44           diagonalization = 'david' ,
45 /
46 &IONS
47 /
48 ATOMIC_SPECIES
49    U  238.02800   U.GGA-PBE-paw.UPF
50    Xe 131.29      Xe.GGA-PBE-paw.UPF
51    Mo 95.94       Mo.GGA-PBE-paw.UPF
52 BEGIN_POSITIONS
53 FIRST_IMAGE
54 ATOMIC_POSITIONS (crystal)
```

```
 55 U         0.000000000    0.000000000    0.000000000    0   0   0
 56 U         0.175109924    0.144562064    0.206801126
 57 U         0.000000000    0.000000000    0.333333333    0   0   0
 58 U         0.000000000    0.000000000    0.666666667    0   0   0
 59 U         0.333333333    0.000000000    0.000000000    0   0   0
 60 U         0.666666667    0.000000000    0.000000000    0   0   0
 61 U         0.000000000    0.333333333    0.000000000    0   0   0
 62 U         0.000000000    0.666666667    0.000000000    0   0   0
 63 U         0.172966137    0.162988305    0.549703444
 64 U         0.170611892    0.151612185    0.878052143
 65 U         0.495257014    0.208922221    0.160293502
 66 U         0.831518767    0.131820848    0.145403232
 67 U         0.187663248    0.516383543    0.207043480
 68 U         0.141733995    0.833501726    0.124057856
 69 U         0.000000000    0.333333333    0.333333333    0   0   0
 70 U         0.000000000    0.666666667    0.666666667    0   0   0
 71 U         0.000000000    0.666666667    0.333333333    0   0   0
 72 U         0.000000000    0.333333333    0.666666667    0   0   0
 73 U         0.333333333    0.000000000    0.333333333    0   0   0
 74 U         0.666666667    0.000000000    0.666666667    0   0   0
 75 U         0.333333333    0.000000000    0.666666667    0   0   0
 76 U         0.666666667    0.000000000    0.333333333    0   0   0
 77 U         0.333333333    0.333333333    0.000000000    0   0   0
 78 U         0.666666667    0.666666667    0.000000000    0   0   0
 79 U         0.666666667    0.333333333    0.000000000    0   0   0
 80 U         0.333333333    0.666666667    0.000000000    0   0   0
 81 U         0.151218039    0.506822556    0.548576738
 82 U         0.146390108    0.829542179    0.788362872
 83 U         0.185174494    0.843342696    0.464715498
 84 U         0.143670888    0.494112883    0.870258462
 85 U         0.521448430    0.133334423    0.501328591
 86 U         0.833500163    0.136787016    0.798434778
 87 U         0.495145627    0.121151838    0.844025002
 88 U         0.863545497    0.168786689    0.469156772
 89 U         0.509274324    0.548329765    0.145881356
 90 U         0.825440636    0.779984312    0.192980330
 91 U         0.842423236    0.466015059    0.136756583
 92 U         0.534458472    0.865141497    0.169291879
 93 U         0.310602920    0.323532531    0.315012292
 94 Mo        0.328606490    0.314883686    0.687255302
 95 Mo        0.674009341    0.305267841    0.662448637
 96 U         0.326631011    0.679870122    0.331479707
 97 U         0.371644890    0.679274954    0.665208460
 98 Mo        0.672193000    0.303810812    0.317212538
 99 U         0.820847752    0.816237464    0.833790833
100 U         0.780071628    0.836705518    0.490628528
101 U         0.493041587    0.450284430    0.842990907
102 U         0.818302670    0.476570581    0.798002061
103 U         0.497363584    0.801441831    0.487806684
104 U         0.478662001    0.802952159    0.852807185
105 U         0.852755368    0.505332549    0.451217549
106 U         0.687902994    0.670557165    0.683653268
107 Xe        0.536400212    0.492947199    0.459667944
108 LAST_IMAGE
109 ATOMIC_POSITIONS (crystal)
110 U         0.000000000    0.000000000    0.000000000    0   0   0
111 U         0.211003121    0.204403180    0.229059646
112 U         0.000000000    0.000000000    0.333333333    0   0   0
113 U         0.000000000    0.000000000    0.666666667    0   0   0
114 U         0.333333333    0.000000000    0.000000000    0   0   0
```

```
115 U          0.666666667    0.000000000    0.000000000    0    0    0
116 U          0.000000000    0.333333333    0.000000000    0    0    0
117 U          0.000000000    0.666666667    0.000000000    0    0    0
118 U          0.137157542    0.154100490    0.530986252
119 U          0.174212597    0.129079723    0.860099413
120 U          0.526361077    0.134914785    0.159501081
121 U          0.862023067    0.133697598    0.175888456
122 U          0.158401680    0.524202200    0.202384340
123 U          0.148244066    0.848143594    0.127034040
124 U          0.000000000    0.333333333    0.333333333    0    0    0
125 U          0.000000000    0.666666667    0.666666667    0    0    0
126 U          0.000000000    0.666666667    0.333333333    0    0    0
127 U          0.000000000    0.333333333    0.666666667    0    0    0
128 U          0.333333333    0.000000000    0.333333333    0    0    0
129 U          0.666666667    0.000000000    0.666666667    0    0    0
130 U          0.333333333    0.000000000    0.666666667    0    0    0
131 U          0.666666667    0.000000000    0.333333333    0    0    0
132 U          0.333333333    0.333333333    0.000000000    0    0    0
133 U          0.666666667    0.666666667    0.000000000    0    0    0
134 U          0.666666667    0.333333333    0.000000000    0    0    0
135 U          0.333333333    0.666666667    0.000000000    0    0    0
136 U          0.178710377    0.490990744    0.516187076
137 U          0.211424168    0.769055779    0.787371675
138 U          0.175042054    0.807911917    0.455992431
139 U          0.138797282    0.465117394    0.842521779
140 U          0.460172734    0.148226288    0.492431541
141 U          0.853214362    0.204001135    0.813615314
142 U          0.517320360    0.155236389    0.808583066
143 U          0.796831649    0.141536092    0.504982369
144 U          0.472082596    0.445170387    0.165199942
145 U          0.797246556    0.819083198    0.205717103
146 U          0.848947010    0.446752941    0.157261389
147 U          0.477337922    0.823974130    0.198045419
148 U          0.357415253    0.358227015    0.377748970
149 Mo         0.316993580    0.314763082    0.680421155
150 Mo         0.607201462    0.351778562    0.642719282
151 U          0.340550068    0.659420403    0.325593019
152 U          0.361166032    0.621614060    0.637522343
153 Mo         0.660553429    0.302407475    0.343460369
154 U          0.864645732    0.824012823    0.866480839
155 U          0.857095779    0.828386743    0.537288219
156 U          0.459295873    0.501704484    0.851504670
157 U          0.787396737    0.503369090    0.850267568
158 U          0.483789070    0.821735869    0.546285283
159 U          0.525937071    0.834449910    0.872642503
160 U          0.803265518    0.439297450    0.559004083
161 U          0.678713059    0.684639768    0.648649342
162 Xe         0.649346200    0.596837093    0.354823657
163 END_POSITIONS
164 K_POINTS automatic
165 4 4 4   0 0 0
166 CELL_PARAMETERS {alat}
167  1.00    0.00     0.00
168  0.00    1.00     0.00
169  0.00    0.00     1.00
170 END_ENGINE_INPUT
171 END
```

VITA

Abu Rafi Mohammad Iasir was born in Chattagram (Chittagong), Bangladesh. He received his BSc. in Chemical Engineering from Bangladesh University of Engineering and Technology in 2012. In 2013, he moved to Mizzou and received an M.S. in Nuclear Engineering under the supervision of Dr. Gary Solbrekken.